THE UNIVERSITY OF CHICAGO

TRANSVERSE GRADIENT UNDULATOR IN A STORAGE RING FREE ELECTRON LASER OSCILLATOR

A DISSERTATION SUBMITTED TO
THE FACULTY OF THE DIVISION OF THE PHYSICAL SCIENCES
IN CANDIDACY FOR THE DEGREE OF
DOCTOR OF PHILOSOPHY

DEPARTMENT OF PHYSICS

BY
YUAN SHEN LI

CHICAGO, ILLINOIS
JUNE 2023

TABLE OF CONTENTS

LIST OF FIGURES

LIST OF TABLES

ACKNOWLEDGMENTS

I would like to thank my advisor, Prof. Kwang-Je Kim and frequent collaborator, Ryan Lindberg, for their invaluable guidance and support throughout my graduate school journey. Without their words of wisdom and encouragement, this thesis project will not have been possible. I would also like to thank my co-advisor, Prof. Young-Kee Kim, as well as members of the thesis committee, Profs. Sergei Nagaitsev, Henry Frisch and Phillipe Guyot-Sionnest for their honest feedback and advice throughout this process.

Rounding out the Argonne FEL group are the postdocs, Ganesh Tiwari and Jeong-Wan Park. I would like to thank them for many hours of fruitful discussion, advice, and general banter. I would also like to credit members of the CBXFEL collaboration (Argonne: Yuri Shvyd'ko, Marion White, Xianbo Shi; SLAC: Gabe Marcus, Zhirong Huang, Diling Zhu, James MacArthur, Rachel Margraf) for all their support throughout my involvement in the project. Also I would like to extend a shout-out to the adminstrators, Cindy Schmitt (Argonne), Amy Schulz (UChicago), Putri Kusumo (UChicago), and Ramona Echols (UChicago) for their help in navigating the various bureaucratic mazes.

Finally, I wish to express my gratitude to my friends and family for keeping me sane and motivated through graduate school. To the friends I've met at UChicago—thank you for so much joy and laughter through thick and thin. To Sami—thank you for being an unwavering pillar of support even when I had my doubts. To my parents—I am eternally grateful for your unconditional love and encouragement, without which I would not be half the person I am today.

ABSTRACT

Accelerator-driven light sources, such as electron storage rings (SRs) and free-electron lasers (FELs), are valuable instruments of scientific discovery thanks to their unparalleled ability to produce extremely bright beams of X-ray light. In this thesis, we will discuss the implementation of the storage ring X-ray FEL oscillator (SRXFELO). The SRXFELO has the potential to combine the strengths of the SR and FEL, thereby surpassing the performance of both in terms of average photon brightness and coherence. Our analysis will be based on a mix of theory and simulation. We begin by discussing the foundational physics of SRs and FELs. We then zoom in on the theoretical basis of the transverse gradient undulator (TGU) as a method to mitigate the SR energy spread deficiency. Next, we construct a custom simulation framework in order to model the SRXFELO from start to end. We use this framework to simulate a hypothetical SRXFELO design based on realistic machine parameters, and report on projected performance and implementation strategies. Finally, we examine challenges associated with the X-ray cavity, such as beam alignment and optical phase purity, in the context of the Cavity-based X-ray FEL (CBXFEL) experiment located at SLAC.

CHAPTER 1

INTRODUCTION

The free-electron laser (FEL) was first invented and experimentally demonstrated by John Madey and collaborators at Stanford University in the 1970s [1, 2]. In the FEL, a relativistic electron bunch radiates coherently while following an approximately sinusoidal trajectory under the influence of an alternating periodic array of magnetic dipoles, also known as the undulator. The emitted radiation wavelength λ_1 is given by

$$\frac{\lambda_1}{\lambda_u} = \frac{1 + K^2/2}{2\gamma_r^2} \tag{1.1}$$

where λ_u is the undulator period, $K \equiv eB_0/mck_u$ is the undulator parameter, and γ_r is the Lorentz factor of the electron bunch[1]. Eq. (1.1) demonstrates that the FEL can in principle radiate at any wavelength, as long as an electron bunch of sufficient brightness[2] can be produced at the requisite γ_r. Indeed, the very first FELs were operational in the infrared (IR) through visible wavelengths. Their continuous tunability, either by altering γ_r or K, made them a useful complement to conventional lasers since the latter tends to be limited by the discrete transition energies of their atomic gain media.

Even in the early years, there exists at least two different configurations of the FEL (Fig. 1.1). The linear, high gain configuration relies on self-amplified spontaneous emission (SASE) in which resonant energy exchange takes place between the high-current electron bunch and the co-propagating spontaneous emission radiation field over a long undulator system. The oscillator configuration, on the other hand, eschews high current and long magnets in favor of enclosing a shorter undulator within a low-loss optical cavity. The high reflectivity mirrors of the cavity entraps a recirculating photon pulse that gets progressively

---

[1] We will discuss these parameters in deeper detail in Chapter 2.

[2] The concept of brightness will be made precise later.

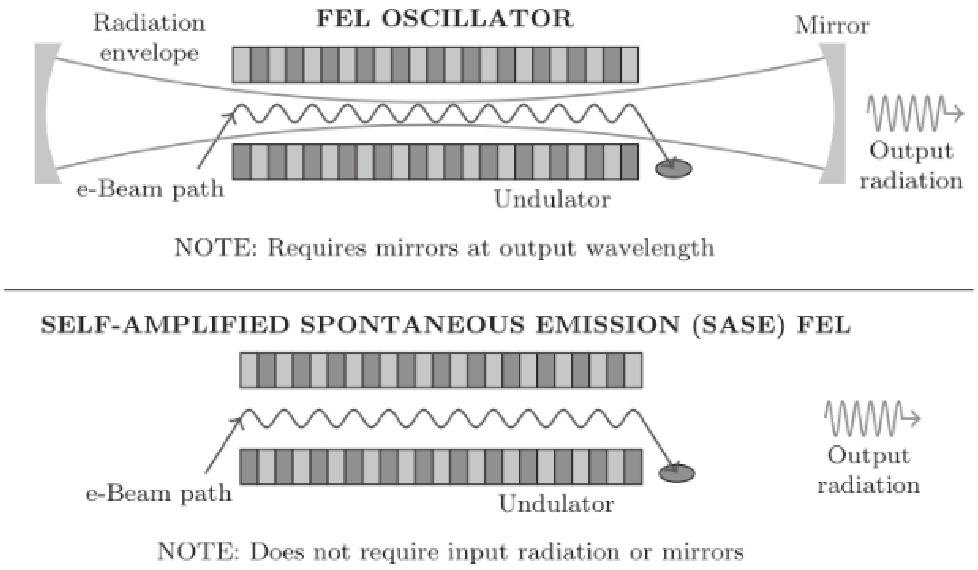

Figure 1.1: Schematic of a FEL oscillator (top) and SASE FEL (bottom). Figure reproduced from [3].

amplified turn by turn by consecutive electron bunches.

The periodic nature of the FEL oscillator makes a natural pairing with the electron storage ring (SR) as its electron provider. When combined, the storage ring FEL oscillator (SRFELO) behaves like a coupled oscillator system. Successfully implementations of the SRFELO have reached wavelengths as small as the middle UV regime ($\sim 200\,\text{nm}$) [4]. Progress into higher photon energies was hampered by the lack of high reflectivity mirrors at those wavelengths.

The SASE FEL suffers from no such restriction. As early as the 1990s and 2000s, SASE FELs have broken into the extreme UV and soft X-ray regime, for instance at the FLASH facility in Hamburg [5]. The domain of hard X-rays was subsequently conquered by the Linear Coherent Light Source (LCLS) at SLAC in 2009 [6]. This ushered in a new era of productive science—the angstrom-scale X-ray regime is home to a vast array of atomic and molecular physics, ready to be probed by the ultrabright, ultrashort photon pulses generated by these X-ray SASE FELs. These devices continue to be hugely successful today, with new facilities coming online all around the world [7–9].

In recent years, interest has been reignited in the SRFELO for X-ray energies, the so-called storage ring X-ray FEL oscillator (SRXFELO) due to significant technological advancements available to the optical cavity [10–13]. Most crucially, highly reflective Bragg crystals, such as diamond or silicon, in conjunction with compound refractive lens (CRL) technology has rendered the X-ray optical cavity a physical possibility.

The SRXFELO, if realised, offers two immediate advantages over the SASE FEL—improvements to user capacity and longitudinal coherence. The first benefit is apparent. The SRXFELO could potentially be run parallel alongside many other user stations in a storage ring, in contrast to the singular output of a linear SASE FEL. The improvement to longitudinal coherence comes from the use of narrow bandwidth Bragg crystals as cavity reflectors. A diamond mirror in the C337 configuration, for instance, has a reflectivity bandwidth of $\sim 20\,\mathrm{meV}$ at the resonant photon energy of $14.4\,\mathrm{keV}$, corresponding to a relative bandwidth of order 10^{-6} to 10^{-7}. In comparison, the bandwidth of an X-ray SASE FEL at a comparable energy is around a thousand times larger, with substantial shot-to-shot variation due to the stochastic nature of SASE [3].

The SRXFELO represents a paradigm shift in X-ray generation, rather than a mere incremental improvement. In the long term, the SRXFELO could serve as a testbed for advanced laser technologies, such as frequency stabilized mode locking [14], or high-gain harmonic generation (HGHG) in conjunction with a SASE FEL. These techniques could unlock the potential to reach even higher photon energies (tens to hundreds of keV) and brightness [3].

Key challenges

With all of that being said, the SRXFELO still faces substantial implementation challenges. The goal of this thesis is to address some of these challenges, and hopefully pave the way toward the physical realization of the SRXFELO. We will summarize the key points below, while delving deeper into each topic in the subsequent chapters.

1. *Electron brightness.* Traditionally, the electron brightness of SRs are insufficient to drive a FEL in the X-ray regime. With the advent of the fourth generation of SRs (4GSRs), however, significant progress has been made. The equilibrium transverse emittance[3] in 4GSRs can be as small as tens of picometer-radians, matching the required mode size for a diffraction-limited X-ray beam. However, energy spread in the longitudinal domain remains one order of magnitude too large. The energy spread deficiency can be bridged by the transverse gradient undulator (TGU) [15, 16]. We will examine this concept in detail in Chapter 3.

2. *Ring-FEL coupling.* The SRXFELO behaves as a coupled oscillator system, which exhibits complex and chaotic behavior [17, 18]. Furthermore, the FEL amplification process can lead to substantial degradation of electron beam brightness, potentially spoiling the beam for other users [19, 20]. We will examine the beam degradation process and discuss mitigation measures in Chapter 5.

3. *Cavity stability and optical quality.* The Cavity-based X-ray FEL (CBXFEL) experiment, based at SLAC, aims to construct the world's first proof-of-concept X-ray cavity [21]. This project will test the limits of current technology, particularly in the areas of mirror/beam stabilization and optical phase purity. In order to establish crucial tolerances and requirements for the CBXFEL project, we will examine X-ray cavity performance under a variety of non-ideal circumstances using numerical analysis. Natually, these simulation results are also relevant to SRXFELO. All of this will be covered in Chapter 6.

In the process of addressing these challenges, we will introduce a hypothetical design (Fig. 1.2) for the SRXFELO based on machine parameters realistic for current technology.

---

[3] To be defined in Chapter 2

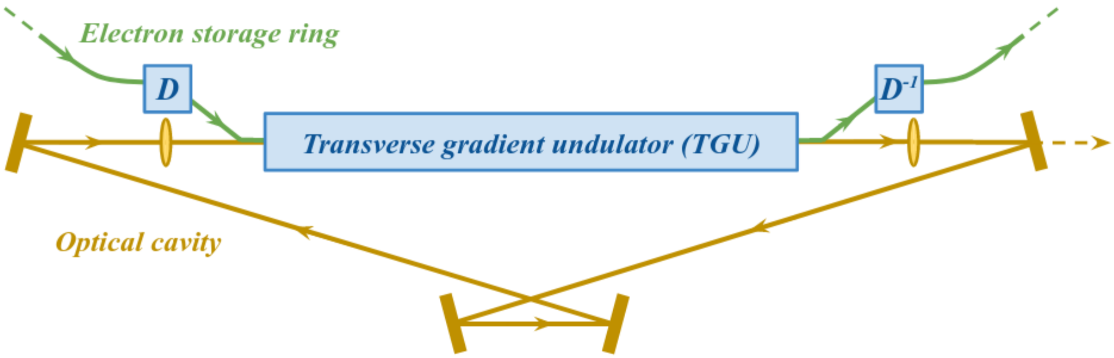

Figure 1.2: Schematic of a storage ring XFELO driven by a TGU. In the following chapters, we will delve into the details of each principal component—TGU, storage ring, and optical cavity.

The storage ring design is based on the PETRA-IV upgrade project [22], whereas the cavity design is inspired by previous works [11, 12]. In order to model this design, we will also detail the construction of a start-to-end simulation framework, which forms the numerical backbone of this thesis project.

Thesis organization

This thesis consists of five main chapters, excluding the Introduction and Conclusion. Chapter 2 begins with an introduction to the physics of relativistic electron and X-ray beams. We will discuss the core working principles of a low gain FEL, with a focus on deriving the gain equation. This is followed by a cursory overview of electron storage ring physics, with an emphasis on radiation damping and equilibrium.

Chapter 3 builds upon the previous chapter and delves into the physics of the TGU in the low gain approximation. Chapter 4 then turns our attention to the simulation aspects of the study, with the goal of elucidating key numerical modeling principles behind each component of the start-to-end simulation framework.

Chapter 5 discusses the design and modeling of a hypothetical SRXFELO, building upon the theoretical and numerical foundation laid in the previous chapters. We will also examine some challenges related to ring-FEL coupling. Chapter 6 then turns our focus to the CBXFEL experiment, with a particular emphasis on XFELO performance under non-ideal optical cavity conditions. The results of this chapter ties our hypothetical SRXFELO design to actual experiment, and represents the first step toward the physical realization of the SRXFELO concept.

CHAPTER 2

THEORY FUNDAMENTALS

This chapter lays the theoretical foundation for the rest of the thesis. We will begin with introductory beam physics concepts, followed individual sections focusing on low gain FEL physics and storage ring dynamics.

2.1 Introductory concepts

To set the stage, we introduce here the basic terminology used to describe X-ray and relativistic electron beams.

2.1.1 Electron beam

The total energy U of an electron is given by

$$U = \gamma m_e c^2, \tag{2.1}$$

where m_e is the electron mass, c is the speed of light, and γ is the relativistic Lorentz factor. Since $m_e c^2$ is constant, we will frequently use γ as a proxy variable for electron energy in this text. In a high energy accelerator, it is not uncommon for U to reach the single GeVs scale, with γ ranging from 10^3 to 10^4. An additional relationship between γ and the electron velocity is

$$\gamma = (1 - \vec{\boldsymbol{\beta}}^2)^{-1/2} \tag{2.2}$$

where $\vec{\boldsymbol{\beta}} \equiv \vec{\boldsymbol{v}}/c$ is the normalized electron velocity. For a $5\,\mathrm{GeV}$ electron with $\gamma \approx 10^4$, the absolute magnitude of $\vec{\boldsymbol{\beta}}$ differs from unity by $\sim 10^{-9}$. Thus in most of this text, we will approximate[1] $\left|\vec{\boldsymbol{\beta}}\right| \approx 1$ or equivalently $|\vec{\boldsymbol{v}}| \approx c$.

---

[1] Care must be taken in using this approximation. Usually, this only applies to the absolute magnitude of $\vec{\boldsymbol{\beta}}$ appearing in prefactors. We *will not* perform a similar approximation for the individual components

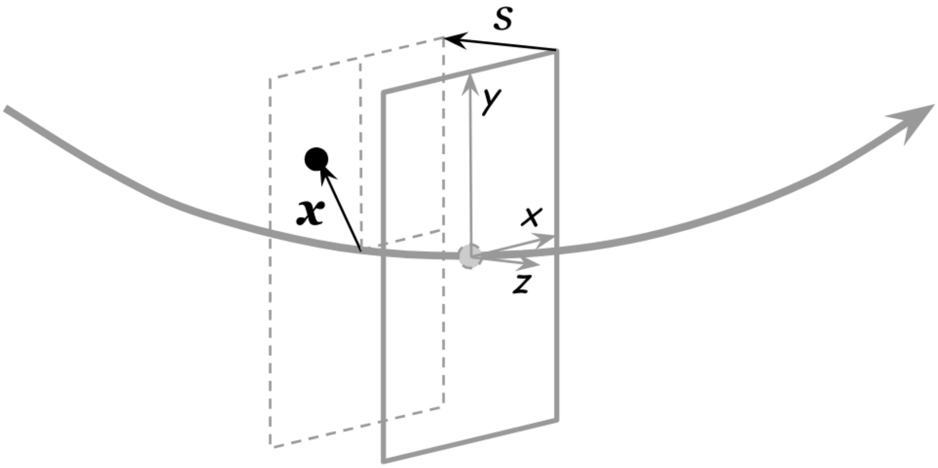

Figure 2.1: Sketch depicting the particle coordinate system in a circular accelerator. The coordinates are defined in reference to the nominal trajectory (gray curved arrow) and the reference particle (gray circle with dashed outline). An actual particle (black circle) has transverse position $\vec{\boldsymbol{x}}$ and longitudinal position s relative to the transverse plane (gray parallelogram) located at the reference particle. The coordinate axes x, y, z are labelled in sans serif typeface. Longitudinal position may also be measured relative to a fixed position in the accelerator (not pictured).

The electron has six total degrees of freedom—three in position and three in momentum. To set up a coordinate system, we define its origin to be a reference particle following exactly the design trajectory of the accelerator (Fig. 2.1). Relative to this particle, we use (x, y) to denote the horizontal and vertical position coordinates transverse to the direction of motion. The longitudinal coordinate can be defined either in absolute terms: distance z measured from a fixed location along the accelerator, or in relative terms: distance s measured from the reference particle. Later on, we will also introduce pondermotive phase θ, defined relative to the radiation wavefront, as an alternate longitudinal coordinate in FEL physics.

Following accelerator physics convention, we use (x', y') to denote the transverse momentum coordinates, given by

$$x' \equiv \frac{\mathrm{d}x}{\mathrm{d}z} = \frac{1}{v_z}\frac{\mathrm{d}x}{\mathrm{d}t} \tag{2.3}$$

$\beta_x, \beta_y, \beta_z$ when discussing FEL physics. The slight difference of β_z from unity plays a crucial role in FEL amplification. We will discuss this in detail later.

and similarly for y'. Here v_z is the longitudinal speed of the electron. The coordinates (x', y') describe the slope of the electron momentum vector relative to the design trajectory. In lieu of a longitudinal momentum coordinate, we will use γ to represent electron energy. Hence, the complete 6D representation of an electron is given by $(x, x', y, y', s, \gamma)$.

When dealing with a group of electrons (a.k.a. *bunch* or *distribution*), it is common to describe the bunch using its first- and second-order statistical moments. The first-order moment, or mean, is calculated in the usual sense. For instance, in a bunch with N_e total electrons, the mean horizontal position

$$\langle x \rangle \equiv \frac{1}{N_e} \sum_j x_j, \tag{2.4}$$

where x_j is the position of the jth electron. One can find the centroid of the electron distribution by calculating all six first-order moments. It is common practice to subtract the centroid when calculating the second-order moments. Then, we can simply define

$$\left\langle x^2 \right\rangle = \frac{1}{N_e} \sum_j x_j^2 \tag{2.5}$$

and similarly for the other five coordinates. This is also known as the root-mean-square (RMS) size, and commonly denoted by σ with the appropriate subscript. It is also useful calculate cross-correlation, for example

$$\left\langle x x' \right\rangle = \frac{1}{N_e} \sum_j x_j x'_j. \tag{2.6}$$

In particular, dispersion is related to the correlation between transverse position and energy. This will be relevant when we discuss TGU physics in Chapter 3.

We use *geometric emittance* to measure the notion of phase space area described by a position coordinate and its corresponding momentum. For instance, the horizontal emittance

ε_x of an electron distribution is given by

$$\varepsilon_x \equiv \sqrt{\sigma_x^2 \sigma_{x'}^2 - \sigma_{xx'}^2}. \tag{2.7}$$

This quantifies the phase space area occupied by the electron distribution within the x-x' domain. It is important to distinguish this ensemble definition of geometric emittance from an alternate definition based on single particle trajectory. The latter definiton, which we shall denote with ϵ, is given by

$$\epsilon_x = \gamma x^2 + 2\alpha x x' + \beta x'^2, \tag{2.8}$$

where β, α, γ are the Courant-Snyder (or Twiss) parameters, also known as envelope functions[2]. In contrast to ε_x, the latter emittance ϵ_x measures the phase space area encircled by the elliptical phase space trajectory traced out by a single particle. For the rest of this thesis, we will primarily use the former distributional sense of emittance, i.e. ε_x. The Twiss parameters are frequently used to parameterize an electron bunch, and are related to the second-order beam moments as follows:

$$\begin{aligned} \beta_x &= \frac{\sigma_x^2}{\varepsilon_x}, & (2.9) \\ \alpha_x &= -\frac{\sigma_{xx'}}{\varepsilon_x}, & (2.10) \\ \gamma_x &= \frac{\sigma_{x'}^2}{\varepsilon_x}. & (2.11) \end{aligned}$$

A similar set of Twiss variables can be defined for the vertical and longitudinal directions.

---

[2] The unfortunate conventional choice to use β, γ conflicts with symbols for normalized velocity and Lorentz factor respectively. While the distinction is usually clear from context, we will add clarifications where necessary.

To round out the discussion of emittance, we shall also introduce *normalized emittance*

$$\varepsilon_{x,n} = \beta_z \gamma \varepsilon_x \approx \gamma \varepsilon_x. \tag{2.12}$$

Normalized emittance is a conserved quantity in a linear system (i.e. deflection and focusing), whereas geometric emittance changes as the bunch is accelerated. It is therefore an important metric during the initial stages of an accelerating system. However, it will not be as relevant in a storage ring, where electron energy is largely kept constant.

2.1.2 X-ray beam

Since the output of an X-ray FEL is extremely collimated, it is useful to describe the radiation beam in the paraxial approximation. We start with the EM wave equation in a vacuum:

$$\left(\frac{1}{c^2} \frac{\partial^2}{\partial t^2} - \frac{\partial^2}{\partial z^2} - \frac{\partial^2}{\partial \boldsymbol{x}^2} \right) \vec{\boldsymbol{E}}(\vec{\boldsymbol{x}}, z, t) = 0. \tag{2.13}$$

We adopt a similar coordinate system as that of the electron bunch, meaning that the radiation beam is propagating in the z direction with $\vec{\boldsymbol{x}} \equiv (x, y)$ representing the horizontal and vertical axes respectively in the transverse plane. We can isolate the time-dependent component of field by substituting $\vec{\boldsymbol{E}}(\boldsymbol{x}, z, t) = \vec{\boldsymbol{E}}_\omega(\vec{\boldsymbol{x}}, z) e^{-i\omega t}$, where ω is the radiation angular frequency. Then the wave equation becomes

$$\left(k^2 + \frac{\partial^2}{\partial z^2} + \frac{\partial^2}{\partial \vec{\boldsymbol{x}}^2} \right) \vec{\boldsymbol{E}}_\omega(\vec{\boldsymbol{x}}, z) = 0, \tag{2.14}$$

where $k \equiv \omega/c$ is the radiation wavenumber. Let us also introduce the angular Fourier transform (FT), namely

$$\begin{aligned}\vec{\boldsymbol{\mathcal{E}}}_\omega(\vec{\boldsymbol{\phi}}) &= \frac{1}{\lambda^2}\int d\vec{\boldsymbol{x}}\, e^{-ik\vec{\boldsymbol{\phi}}\cdot\vec{\boldsymbol{x}}}\vec{\boldsymbol{E}}_\omega(\vec{\boldsymbol{x}}), & (2.15)\\ \vec{\boldsymbol{E}}_\omega(\vec{\boldsymbol{x}}) &= \int d\vec{\boldsymbol{\phi}}\, e^{ik\vec{\boldsymbol{\phi}}\cdot\vec{\boldsymbol{x}}}\vec{\boldsymbol{\mathcal{E}}}_\omega(\vec{\boldsymbol{\phi}}), & (2.16)\end{aligned}$$

Note that we omitted the longitudinal coordinate z for brevity. Turning our attention back to Eq. (2.14), we can take the angular FT to obtain

$$\left[k^2(1-\vec{\boldsymbol{\phi}}^2) + \frac{\partial^2}{\partial z^2}\right]\vec{\boldsymbol{\mathcal{E}}}_\omega(\vec{\boldsymbol{\phi}}, z) = 0. \tag{2.17}$$

This second-order linear differential equation has the solution $\vec{\boldsymbol{\mathcal{E}}}_\omega(\vec{\boldsymbol{\phi}}, z) = e^{ikz\sqrt{1-\vec{\boldsymbol{\phi}}^2}}\vec{\boldsymbol{\mathcal{E}}}(\vec{\boldsymbol{\phi}}, 0)$ for waves propagating in the $+z$ direction. Here $\vec{\boldsymbol{\mathcal{E}}}_\omega(\vec{\boldsymbol{\phi}}, 0)$ is the initial field at $z = 0$. We apply the paraxial approximation, i.e. $\vec{\boldsymbol{\phi}}^2 \ll 1$, so that $\sqrt{1-\vec{\boldsymbol{\phi}}^2} \approx 1 - \vec{\boldsymbol{\phi}}^2/2$ and

$$\vec{\boldsymbol{\mathcal{E}}}_\omega(\vec{\boldsymbol{\phi}}, z) = e^{ikz(1-\vec{\boldsymbol{\phi}}^2)/2}\vec{\boldsymbol{\mathcal{E}}}_\omega(\vec{\boldsymbol{\phi}}, 0), \tag{2.18}$$

In other words, vacuum propagation of a paraxial wave over distance s is given by the simple multiplication of phase factor $e^{-iks\vec{\boldsymbol{\phi}}^2/2}$ in the angular representation. This is a very useful result that we will revisit when we discuss the Fourier optics cavity code.

In a similar vein, it can be shown that the action of a lens on the paraxial wave is the multiplication of a phase factor in the spatial representation. More precisely, for a lens with focal length f, refractive index n, thickness ℓ and pupil function $p(\vec{\boldsymbol{x}})$, the phase factor is given by

$$\vec{\boldsymbol{E}}_\omega(\vec{\boldsymbol{x}}, z+\ell) = p(\vec{\boldsymbol{x}})e^{ikn\ell}e^{-ik\vec{\boldsymbol{x}}^2/(2f)}\vec{\boldsymbol{E}}_\omega(\vec{\boldsymbol{x}}, z). \tag{2.19}$$

For our purposes, we typically apply the thin lens approximation $\ell \ll 1$ and a constant pupil function $p = 1$, whence the first and second factors reduce to unity.

To round out the discussion of basic optical beam concepts, we shall introduce the Gaussian beam. In its most general form,

$$\vec{\boldsymbol{E}}_\omega(r,z) = \frac{\vec{\boldsymbol{E}}_0 e^{ikz}}{\sqrt{1+iz(\sigma_{r'}/\sigma_r)}} \exp\left(-\frac{r^2}{4\sigma_r^2(1+iz(\sigma_{r'}/\sigma_r))}\right), \tag{2.20}$$

where r is the radial position coordinate, $\vec{\boldsymbol{E}}_0$ is a constant magnitude, and $\sigma_r, \sigma_{r'}$ are the RMS beam size and divergence at the waist respectively. Note that z is defined with respect to the location of the beam waist. The Gaussian beam carries special significance because it is the fundamental transverse EM mode in an optical cavity (also referred to as the TEM_{00} mode).

At the beam waist $z = 0$, the field reduces to

$$\vec{\boldsymbol{E}}_\omega(r,0) = \vec{\boldsymbol{E}}_0 \exp\left(-\frac{r^2}{4\sigma_r^2}\right), \tag{2.21}$$

with the corresponding angular representation

$$\vec{\boldsymbol{\mathcal{E}}}_\omega(\phi,0) = \vec{\boldsymbol{\mathcal{E}}}_0 \left(-\frac{\phi^2}{4\sigma_{r'}^2}\right), \tag{2.22}$$

where ϕ is the radial angular coordinate. Notice the factor of 4 in the exponent denominator—this is because $\sigma_r, \sigma_{r'}$ are measured with respect to beam intensity, which is proportional to $\left|\vec{\boldsymbol{E}}^2\right|$. It is also useful to define the *Rayleigh length*

$$Z_R = \sigma_r/\sigma_{r'}. \tag{2.23}$$

The Rayleigh length represents the distance over which the beam diverges to $\sqrt{2}$ times its previous size, with a corresponding $1/e^2$ drop in axial intensity. We can then express the

RMS beam size as a function of longitudinal distance:

$$\sigma_r(z) = \sigma_r \sqrt{1 + \left(\frac{z}{Z_R}\right)^2}. \tag{2.24}$$

The Gaussian beam grows larger in spatial dimensions as it converges and then diverges around its waist.

2.1.3 Brightness function

Brightness is an important figure of merit for the light source community. In the most abstract sense, it measures the density of particles (photons or electrons) per six-dimensional phase space area.

In the context of electrons, we measure brightness as particle number density per unit momentum and position. Up to this point, we have been treating the electron bunch as a collection of point particles. However, we may also take the Eulerian approach by defining a phase space distribution function $F(x, x', y, y', z, \gamma)$, with the property that

$$N_e = \int dx dx' dy dy' dz d\gamma \, F(x, x', y, y', z, \gamma), \tag{2.25}$$

where N_e is the total number of electrons. When integrated over a finite extent in phase space, F gives the electron number density within that region. Therefore F is also the electron brightness function.

For the photon beam, brightness is defined as photon flux per unit area, solid angle, and frequency bandwidth at the light source:

$$\mathcal{B} = \frac{dN_{\text{ph}}}{d\vec{\boldsymbol{x}} d\vec{\boldsymbol{\phi}} d\omega dt}, \tag{2.26}$$

where N_{ph} is the total number of photons. There is a further distinction between peak brightness, which is calculated over the time duration of a single radiation pulse, and average brightness, which includes the repetition rate of said pulse.

For a given EM field E, we can more formally define a brightness function associated with the Wigner transform[3] of the radiation field E [3, 23]:

$$\begin{aligned} B(\vec{\boldsymbol{x}}, \vec{\boldsymbol{\phi}}) &= \int d\vec{\boldsymbol{y}}\, E^*(\vec{\boldsymbol{x}} + \vec{\boldsymbol{y}}/2) E(\vec{\boldsymbol{x}} - \vec{\boldsymbol{y}}/2) e^{ik\vec{\mathbf{y}}\cdot\vec{\boldsymbol{\phi}}}, & (2.27) \\ &= \int d\vec{\boldsymbol{\xi}}\, \mathcal{E}^*(\vec{\boldsymbol{\phi}} + \vec{\boldsymbol{\xi}}/2) \mathcal{E}(\vec{\boldsymbol{\phi}} - \vec{\boldsymbol{\xi}}/2) e^{-ik\vec{\boldsymbol{\xi}}\cdot\vec{\boldsymbol{x}}}. & (2.28) \end{aligned}$$

The brightness function B defined[4] in this form acts as the conceptual counterpart to the electron distribution function F, in that for phase space areas larger than $\lambda/2$, fully integrating over B yields the photon number[5].

The brightness function of a Gaussian beam is given by

$$B(\vec{\boldsymbol{x}}, \vec{\boldsymbol{\phi}}, z) = B_0 \exp\left(-\frac{(x - z\phi)^2}{2\sigma_r^2} - \frac{\phi^2}{2\sigma_{r'}^2} \right) \tag{2.29}$$

where B_0 is the on-axis brightness at the source origin.

2.2 Free-electron laser (FEL) physics

In this section, we will examine fundamental concepts in free-electron laser operation. In particular, we will focus on deriving FEL gain in the low gain approximation (to be defined later) with the goal of understanding the operating principle behind the XFELO, as well as laying the theoretical foundation for the subsequent chapter on TGU physics.

Comprehensive treatments of FEL physics can be found in many textbooks and review

---

[3] This is a close relative to the Wigner quasiprobability distribution function in quantum mechanics.

[4] For broadband/incoherent fields, we use the time-averaged integrand $\langle E(\vec{\boldsymbol{x}} - \vec{\boldsymbol{y}}/2) E^*(\vec{\boldsymbol{x}} + \vec{\boldsymbol{y}}/2) \rangle$ instead.

[5] For areas smaller than $\lambda/2$, B is not guaranteed to be positive. This is due to the quantum mechanical nature of light. For more details of this brightness function definition, we refer readers to [3, 23].

articles. See, for instance [3, 24, 25], for topics not covered in this thesis. The author would especially like to credit [3] for the following discussion.

2.2.1 Undulator radiation

The goal of this subsection is to arrive at an expression for the spontaneous emission radiation field due to an electron traversing the undulator. Along the way, we will derive some key parameters of undulator radiation, including its fundamental wavelength and spectral characteristics. We shall begin by deriving the radiation field due to a moving point charge under the paraxial approximation.

Paraxial radiation field due to moving point charge

In the presence of charge density $\rho(\vec{\boldsymbol{x}}, z, t)$ and current density $\vec{\boldsymbol{J}}(\vec{\boldsymbol{x}}, z, t)$, the EM wave equation Eq. (2.13) acquires a driving term:

$$\left(\frac{1}{c^2}\frac{\partial^2}{\partial t^2} - \frac{\partial^2}{\partial z^2} - \frac{\partial^2}{\partial \vec{\boldsymbol{x}}^2}\right)\vec{\boldsymbol{E}}(\vec{\boldsymbol{x}}, z, t) = -\frac{1}{\epsilon_0 c^2}\left(c^2\boldsymbol{\nabla}\rho + \frac{\partial \vec{\boldsymbol{J}}}{\partial t}\right), \tag{2.30}$$

where ϵ_0 is the vacuum permittivity and c is the speed of light. Like before, we can isolate the time-dependent component by defining $\vec{\boldsymbol{E}}(\vec{\boldsymbol{x}}, z, t) = \vec{\boldsymbol{E}}_\omega(\vec{\boldsymbol{x}}, z)e^{-i\omega t}$ and taking the temporal FT on both sides to obtain

$$\left(k^2 - \frac{\partial^2}{\partial z^2} - \frac{\partial^2}{\partial \vec{\boldsymbol{x}}^2}\right)\vec{\boldsymbol{E}}_\omega(\vec{\boldsymbol{x}}, z) = -\frac{1}{2\pi\epsilon_0 c^2}\int dt\, e^{i\omega t}\left(c^2\boldsymbol{\nabla}\rho + \frac{\partial \vec{\boldsymbol{J}}}{\partial t}\right). \tag{2.31}$$

Let us define the envelope function $\tilde{\vec{\boldsymbol{E}}}_\omega(\vec{\boldsymbol{x}}, z) \equiv \vec{\boldsymbol{E}}_\omega(\vec{\boldsymbol{x}}, z)e^{ikz}$. As its name implies, the envelope function encompasses the maximum extent of the wave oscillations and changes slowly over the length scale of wavelength λ. The factor of e^{ikz} represents the rapid wave oscillations within this slow-varying envelope. This allows us to drop second and higher order derivatives in z of the envelope function $\tilde{\boldsymbol{E}}_\omega$, i.e.

$$\frac{\partial^2}{\partial z^2}\left(\tilde{\boldsymbol{E}}_\omega e^{ikz}\right) \approx \left(2ik\frac{\partial}{\partial z} - k^2\right)\tilde{\boldsymbol{E}}_\omega e^{ikz}. \tag{2.32}$$

Substituting this result into Eq. (2.31) yields

$$\left(\frac{\partial}{\partial z} - \frac{i}{2k}\frac{\partial^2}{\partial \vec{\boldsymbol{x}}^2}\right)\tilde{\boldsymbol{E}}_\omega(\vec{\boldsymbol{x}}, z) = -\frac{i}{4\pi\epsilon_0 c^2 k}\int dt\, e^{ik(ct-z)}\left(c^2\boldsymbol{\nabla}\rho + \frac{\partial \vec{\boldsymbol{J}}}{\partial t}\right). \tag{2.33}$$

We perform the angular FT on both sides and switch the derivatives on the right hand side using integration by parts:

$$\left(\frac{\partial}{\partial z} - \frac{ik}{2}\vec{\boldsymbol{\phi}}^2\right)\tilde{\boldsymbol{\mathcal{E}}}_\omega(\vec{\boldsymbol{\phi}}, z) = -\frac{1}{4\pi\epsilon_0 c\lambda^2}\int dt d\vec{\boldsymbol{x}}\, e^{ik(ct-z-\vec{\boldsymbol{\phi}}\cdot\vec{\boldsymbol{x}})}\left(\vec{\boldsymbol{J}} - c\rho\vec{\boldsymbol{\phi}}\right). \tag{2.34}$$

For a moving electron, the charge density $\rho = -e\delta(z - z_j)\delta(\vec{\boldsymbol{x}} - \vec{\boldsymbol{x}}_j)$, where δ is the delta function and the subscript j denotes the coordinates of the jth electron. The current density $\vec{\boldsymbol{J}} = c\rho\vec{\boldsymbol{\beta}}_j$, where $\vec{\boldsymbol{\beta}}_j$ is the normalized particle velocity. It is convenient for the dt integration in Eq. (2.34) to switch the dependence of z and t coordinates. Let $t_j(z)$ denote the particle time coordinate at position z, such that $\delta(z - z_j) = \delta(t - t_j)/\left|\mathrm{d}z/\mathrm{d}t_j\right| \approx \delta(t - t_j)/c$. Substituting the expressions into Eq. (2.34) yields

$$\left(\frac{\partial}{\partial z} - \frac{ik}{2}\vec{\boldsymbol{\phi}}^2\right)\tilde{\boldsymbol{\mathcal{E}}}_\omega(\vec{\boldsymbol{\phi}}, z) = \frac{e(\vec{\boldsymbol{\beta}}_j - \vec{\boldsymbol{\phi}})}{4\pi\epsilon_0 c\lambda^2}\exp\left(ik[ct_j(z) - z - \vec{\boldsymbol{\phi}}\cdot\vec{\boldsymbol{x}}_j(z)]\right) \tag{2.35}$$

This first-order differential equation has the integral solution

$$\tilde{\boldsymbol{\mathcal{E}}}_\omega(\vec{\boldsymbol{\phi}}, z) = \int_{-\infty}^{z} ds\, \frac{e(\vec{\boldsymbol{\beta}}_j(s) - \vec{\boldsymbol{\phi}})}{4\pi\epsilon_0 c\lambda^2}\exp\left(ik\left[ct_j(s) - s - \vec{\boldsymbol{\phi}}\cdot\vec{\boldsymbol{x}}_j(s) + \vec{\boldsymbol{\phi}}^2\frac{(s-z)}{2}\right]\right). \tag{2.36}$$

This is the radiation field due to a relativistic electron moving along the longitudinal axis ($\beta_z \approx c$) with transverse velocity $\vec{\boldsymbol{\beta}}_j(z)$ and trajectory described by $\vec{\boldsymbol{x}}_j(z), t_j(z)$. In the next part, we shall derive the trajectory of this particle in the presence of the undulator.

Electron trajectory in an undulator

The magnetic field of an ideal planar undulator can be approximated by

$$\vec{\boldsymbol{B}}(x,y,z) = -(B_0 \cosh(k_u y)\sin(k_u z))\hat{\mathbf{y}} - (B_0 \sinh(k_u y)\cos k_u z)\hat{\mathbf{x}} \tag{2.37}$$

where B_0 is the peak magnetic field strength, and k_u is the undulator wavenumber. We also define $\lambda_u \equiv 2\pi/k_u$ as the undulator wavelength/period, and N_u, L_u as the number of undulator periods and overall length of the undulator respectively. Using the Lorentz force law, the velocity of an electron travelling along the nominal central axis is

$$\beta_x = \frac{K}{\gamma}\cos(k_u z), \tag{2.38}$$

where the *undulator parameter*

$$K \equiv \frac{eB_0}{mck_u} \approx 0.934\,\lambda_u\,[\mathrm{cm}]\,B_0\,[\mathrm{T}]. \tag{2.39}$$

Thus K can be regarded as a measure of the undulator strength, and also the magnitude of deflection in the electron trajectory. Undulators typically operate under $K \lesssim 1$, where the electron path lies within the $1/\gamma$ opening cone of the emitted radiation, in contrast with wigglers ($K \gtrsim 1$).

Returning to the electron velocity, the longitudinal velocity β_z is reduced from the maximum value $\left|\vec{\boldsymbol{\beta}}\right|$ due to the horizontal deflection β_x:

$$\beta_z = \sqrt{1 - \frac{1}{\gamma^2} - \beta_x^2} \approx 1 - \frac{1 + K^2/2}{2\gamma^2} - \frac{K^2}{4\gamma^2}\cos(2k_u z), \tag{2.40}$$

where we assumed $\beta_x \ll 1$. The first two terms describe the average longitudinal velocity $\bar{\beta}_z$ of the electron reference frame, about which the electron oscillates in a figure-eight pattern associated with the last term.

Recall that Eq. (2.36) expresses the longitudinal coordinate using the particle time coordinate $t_j(z)$. This can be obtained from integration of Eq. (2.40) via

$$\begin{aligned} t_j(z) &= \int_0^z dz' \, \frac{\mathrm{d}t}{\mathrm{d}z'} = \int_0^z dz' \, \frac{1}{c\beta_z(z')} \\ &= \frac{z}{c}\left(1 + \frac{1 + K^2/2}{2\gamma^2}\right) + \frac{K^2}{8ck_u\gamma^2}\sin(2k_u z) + t_j(0). \end{aligned} \tag{2.41}$$

Having derived the electron trajectory and velocity, we will use Eq. (2.36) to derive the undulator field.

Paraxial undulator radiation field (on-axis approximation)

From Eq. (2.36), the $\hat{\mathbf{x}}$ component of the radiation field is,

$$\tilde{\mathcal{E}}_{\omega,x}(\vec{\boldsymbol{\phi}}, z) = \int_{-\infty}^{z} ds \, \frac{e(\beta_x(s) - \phi_x)}{4\pi\epsilon_0 c\lambda^2} \exp\left(ik\left[ct_j(s) - s - \vec{\boldsymbol{\phi}} \cdot \vec{\boldsymbol{x}}_j(s) + \vec{\boldsymbol{\phi}}^2 \frac{(s-z)}{2}\right]\right), \tag{2.42}$$

where in the numerator of the prefactor,

$$\beta_x(s) - \phi_x = \frac{K}{\gamma}\cos(k_u s) - \phi_x. \tag{2.43}$$

We shall make the argument to drop the ϕ_x term which arises from the charge density ρ. The undulator radiation cone has an opening angle of $\phi \lesssim \frac{1}{\gamma\sqrt{N_u}}$ about the central axis. (We will justify this later.) Assuming $K \sim 1$ and $N_u \gg 1$, the first term $\beta_x(s)$ dominates in our region of interest. Thus we obtain

$$\begin{aligned}\tilde{\mathcal{E}}_{\omega,x}(\vec{\boldsymbol{\phi}}) &= \int_0^{L_u} ds\, \frac{eK\cos(k_u s)}{4\pi\epsilon_0\gamma c\lambda^2}\exp\left(ik(ct_j(s)-s)\right) \\ &\qquad\times\exp\left(-ik\vec{\boldsymbol{\phi}}\cdot\vec{\boldsymbol{x}}_j(s)+ik\vec{\boldsymbol{\phi}}^2\frac{(s-L_u)}{2}\right). \qquad (2.44)\end{aligned}$$

Notice that we updated the bounds of the integral to encompass the full length of the undulator L_u. We turn our attention to

$$\exp\bigl(ik(ct_j(s)-s)\bigr) = \exp\left(ik\left[s\,\frac{1+K^2/2}{2\gamma^2}+\frac{K^2}{8k_u\gamma^2}\sin(2k_u s)+ct_j(0)\right]\right). \qquad (2.45)$$

The middle term in the exponent can be expanded using the Jacobi-Anger identity

$$e^{ix\sin\theta} = \sum_{n=-\infty}^{\infty} J_n(x)e^{in\theta}, \qquad (2.46)$$

where J_n is the nth Bessel function of the first kind. Whence

$$\begin{aligned}\cos(k_u s)\exp\bigl(ik(ct_j(s)-s)\bigr) &= \frac{e^{ikct_j(0)}}{2}\sum_{n=-\infty}^{\infty} J_n\left(\frac{kK^2}{8k_u\gamma^2}\right)\left(e^{ik_u s}+e^{-ik_u s}\right) \\ &\qquad\times\exp\left(iks\,\frac{1+K^2/2}{2\gamma^2}+2ink_u s\right), \qquad (2.47)\end{aligned}$$

where we wrote $\cos(k_u s)$ in exponential form. The exponentials within the summation take the form

$$\sum_n \exp\left(ik_u s\left[\frac{k}{k_u}\frac{1+K^2/2}{2\gamma^2}+2n\pm 1\right]\right) \qquad (2.48)$$

Over the domain of the ds integral in Eq. (2.44), the periodic exponential term above will average to zero *unless* the exponent is zero (or very small). Peak power will occur when the exponent is zero, at frequencies associated with

$$\lambda_h = \frac{\lambda_u}{h}\frac{1+K^2/2}{2\gamma^2} \quad \text{for} \quad h = 2n \pm 1. \tag{2.49}$$

where we define $\lambda_h \equiv \lambda_1/h$ to be the hth harmonic of the fundamental wavelength λ_1. Eq. (2.49) is an important result that not only yields the fundamental frequency of the radiation field in terms of the electron and undulator parameters, but also implies that on-axis undulator radiation consists only of odd harmonics of λ_1. (In the off-axis case, it can be shown that the undulator field consists of all odd and even harmonics.)

By considering slight deviations from λ_h, we can also deduce the bandwidth of the frequency peaks. We will discuss this shortly. For a given frequency k close to harmonic hk_1, let us define the scaled frequency difference (detuning) $\Delta\nu \equiv (k - hk_1)/k_1$ and scaled frequency $\nu \equiv k/k_1 = h + \Delta\nu$. We now rewrite Eq. (2.44) in terms of $\nu, \Delta\nu$ and including everything we have derived so far.

$$\tilde{\mathcal{E}}_{\nu,x}(\vec{\boldsymbol{\phi}}) = \sum_{h \text{ odd}} \frac{eK[JJ]_h}{8\pi\epsilon_0\gamma c\lambda^2} e^{ic\nu k_1 t_j(0)} \int_0^{L_u} ds\, e^{ik_u s\Delta\nu} e^{-ik(\vec{\boldsymbol{\phi}}\cdot\vec{\boldsymbol{x}}_j(s) - \vec{\boldsymbol{\phi}}^2(s-L_u)/2)}, \tag{2.50}$$

where the Bessel functions are abbreviated as

$$[JJ]_h = (-1)^{(h-1)/2}\left(J_{(h-1)/2}\left(\frac{hK^2}{4+2K^2}\right) - J_{(h+1)/2}\left(\frac{hK^2}{4+2K^2}\right)\right). \tag{2.51}$$

The argument of the Bessel functions have been simplified using Eq. (2.49). We also employed the identity $J_{-n}(x) = (-1)^n J_n(x)$ so that the summation of h is only over the positive odd integers.

We can determine the angular and spectral bandwidth by considering the radiation resulting from a perfectly on-axis electron with trajectory $\vec{\boldsymbol{x}}_j(z) = 0$. Then the ds integral

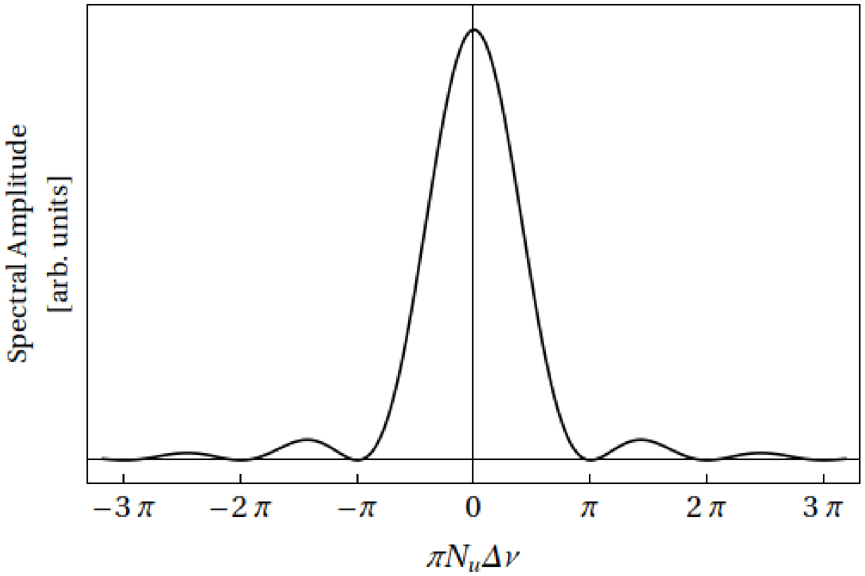

Figure 2.2: Plot of undulator radiation spectral amplitude as function of detuning $\pi N_u \Delta\nu$. The radiation amplitude is proportional to the sinc^2 function, which has a characteristic width of π. This implies that undulator radiation has a characteristic frequency bandwidth of $\sigma_{\Delta\nu} \sim 1/N_u$.

Eq. (2.50) takes the form

$$\int_0^{L_u} ds\, e^{iAs} = \frac{e^{iAL_u} - 1}{iA} = L_u e^{iAL_u/2}\,\mathrm{sinc}(AL_u/2), \tag{2.52}$$

where $\mathrm{sinc}(x) \equiv \sin(x)/x$ and the coefficient

$$\frac{AL_u}{2} = \frac{L_u}{2}(k_u \Delta\nu + k\phi^2/2) \tag{2.53}$$

$$= \pi N_u \left(\Delta\nu + \frac{h\gamma^2\phi^2}{1 + K^2/2} \right). \tag{2.54}$$

In other words, the spectral and angular profile of the radiation field is described by the sinc function:

$$\mathcal{E} \propto \mathrm{sinc}\left[\pi N_u \left(\Delta\nu + \frac{h\gamma^2\phi^2}{1 + K^2/2} \right) \right]. \tag{2.55}$$

Figure 2.2 shows the undulator radiation spectral amplitude. The characteristic width of the central peak of sinc(x) is π, meaning in the frequency space the radiation field has the RMS width

$$\sigma_{\Delta\nu} \sim \frac{1}{N_u} \quad \Rightarrow \quad \frac{\Delta\omega}{\omega_h} = \frac{1}{hN_u}, \tag{2.56}$$

and in the angular space,

$$\sigma_\phi \sim \frac{1}{\gamma}\sqrt{\frac{1+K^2/2}{hN_u}}. \tag{2.57}$$

This angular width is consistent with our assumption of the narrow cone opening angle earlier.

Undulator radiation from arbitrary non-ideal electron

Let us define the "perfect" electron as having zero deviation from nominal energy, timing, and transverse trajectory. Relative energy deviation is $\eta \equiv (\gamma - \gamma_r)/\gamma_r$ where γ_r is the nominal energy. Then the perfect electron has $\eta_j = 0$, $t_j = 0$, $\vec{\boldsymbol{x}}_j = 0$ and $\vec{\boldsymbol{x}}'_j = 0$. Using Eq. (2.44), the fundamental harmonic of the undulator radiation field from this perfect electron is

$$\mathcal{E}_0(\nu, \vec{\boldsymbol{\phi}}) = \frac{eK[JJ]}{8\pi\epsilon_0\gamma_r c\lambda^2}\int_0^{L_u} e^{ik_u s\Delta\nu - ik\vec{\boldsymbol{\phi}}^2(s-L_u)/2}. \tag{2.58}$$

The subscript 0 denotes the perfect electron. We moved the relative frequency ν into the argument to highlight the frequency-angular dependence of $\mathcal{E}$. What about some arbitrary electron j with non-zero η_j, t_j and trajectory $\vec{\boldsymbol{x}}_j, \vec{\boldsymbol{x}}'_j$? We shall derive the resultant radiation field using heuristic arguments.

Position. Imagine a test electron with zero η_j, t_j and $\vec{\boldsymbol{x}}'_j$, but non-zero $\vec{\boldsymbol{x}}$. Consequently, this test electron is equivalent to the perfect electron with transverse trajectory displaced by a constant vector $\vec{\boldsymbol{x}}$. Clearly, the radiation field is also displaced by $\vec{\boldsymbol{x}}$. As discussed in the previous section, position displacement is equivalent to multiplication by the phase factor $e^{-ik\vec{\boldsymbol{\phi}}\cdot\vec{\boldsymbol{x}}}$ in angular space.

Time. Now take a test electron with non-zero t_j relative to the perfect electron. Temporal displacement is equivalent to multiplication by $e^{i\omega t_j} = e^{ickt_j}$ in the frequency domain.

Energy. Consider a test electron with non-zero energy deviation $\eta_j = \Delta\gamma/\gamma_r$. The resulting change in fundamental frequency $\Delta\omega_1$ can be derived from partial differentiation of Eq. (2.49):

$$\frac{\Delta\omega_1}{\omega_1} = 2\frac{\Delta\gamma}{\gamma_r} = 2\eta_j. \tag{2.59}$$

In other words, an energy deviation of η_j is equivalent to a relative frequency shift of $2\eta_j$.

Angle. Similar to the energy argument, an angular displacement $\vec{\boldsymbol{x}}'_j$ in the electron trajectory is equivalent to an angular shift in $\vec{\boldsymbol{\phi}}$ by the same amount.

Putting everything together, for an electron with arbitrary $\eta_j, t_j, \vec{\boldsymbol{x}}_j, \vec{\boldsymbol{x}}'_j$, the undulator field is

$$\mathcal{E}_j(\nu, \vec{\boldsymbol{\phi}}) = \exp\Big(ik(ct_j - \vec{\boldsymbol{\phi}} \cdot \vec{\boldsymbol{x}}_j)\Big)\, \mathcal{E}_0(\nu - 2\eta_j, \vec{\boldsymbol{\phi}} - \vec{\boldsymbol{x}}'_j) \tag{2.60}$$

with $\mathcal{E}_0$ provided in Eq. (2.58). In an electron bunch with N_e electrons, we can either adopt the Lagrangian treatment (electrons as point particles) or the Eulerian treatment (electron bunch as a distribution). In the former, the resulting field is a summation

$$\mathcal{E}(\nu, \vec{\boldsymbol{\phi}}) = \sum_j^{N_e} \exp\Big(ik(ct_j - \vec{\boldsymbol{\phi}} \cdot \vec{\boldsymbol{x}}_j)\Big)\, \mathcal{E}_0(\nu - 2\eta_j, \vec{\boldsymbol{\phi}} - \vec{\boldsymbol{x}}'_j). \tag{2.61}$$

Whereas in the Eulerian/phase space distribution representation, we have

$$\mathcal{E}(\nu, \vec{\boldsymbol{\phi}}) = \int d\eta dt d\vec{\boldsymbol{y}} d\vec{\boldsymbol{y}}'\, f(\eta, t, \vec{\boldsymbol{y}}, \vec{\boldsymbol{y}}') \exp\Big(ik(ct - \vec{\boldsymbol{\phi}} \cdot \vec{\boldsymbol{y}})\Big)\, \mathcal{E}_0(\nu - 2\eta, \vec{\boldsymbol{\phi}} - \vec{\boldsymbol{y}}'). \tag{2.62}$$

where f is the particle phase space distribution function with

$$N_e = \int d\eta dt d\vec{\boldsymbol{y}} d\vec{\boldsymbol{y}}'\, f(\eta, t, \vec{\boldsymbol{y}}, \vec{\boldsymbol{y}}'). \tag{2.63}$$

(To avoid confusion: $\vec{\boldsymbol{y}}, \vec{\boldsymbol{y}}'$ are spatial and angular integration variables, and not referring explicitly to the vertical dimension.)

2.2.2 FEL particle and field equations

The goal of this subsection is to arrive at the system of differential equations that govern the FEL interaction between the radiation field and the electron bunch. These equations form the theoretical foundation of most FEL simulation codes, such as `GENESIS` or `ginger`.

But before we begin, it is useful to distinguish between the two longitudinal length scales in this problem: the length of the electron/radiation pulse, and the length of the undulator. The former describes the size of the problem domain, whereas the latter describes the time evolution of the system. To measure time evolution, we shall use distance along undulator z as the most natural choice, with initial value $z = 0$ and final value $z = L_u$. Thus we will frequently make the substitution $dt \to (1/c)\, dz$ when deriving the equations of motion.

As for the problem domain, we have already discussed the particle time coordinate $t_j(z)$ in Eq. (2.41). However due to the periodic nature of the radiation field, it will be useful to define a phase coordinate θ_j relative to the radiation wavefronts. This is also known as the *FEL ponderomotive phase*. We will elaborate on the relationship between θ_j and t_j below.

FEL pendulum equations

The system of equations that govern the longitudinal evolution of the electrons is also known as the *FEL pendulum equations*, for their mathematical resemblence to the equations that describe the physical pendulum.

The rate of particle energy change can be derived from the Lorentz force law and the definition of work:

$$\frac{\mathrm{d}U}{\mathrm{d}t} = \vec{\boldsymbol{F}} \cdot \vec{\boldsymbol{v}} = -ec\vec{\boldsymbol{E}} \cdot \vec{\boldsymbol{\beta}} \tag{2.64}$$

where $U = \gamma mc^2$ is the electron energy, $\vec{\boldsymbol{E}}$ is the co-propagating radiation field, and $\vec{\boldsymbol{\beta}}$ describes the electron velocity. Let us treat the radiation field as horizontally polarized, whence

$$\frac{\mathrm{d}\gamma}{\mathrm{d}z} = -\frac{eKE_x}{\gamma m^2 c}\cos(k_u z), \tag{2.65}$$

where we substituted Eq. (2.38) for the electron velocity and switched from $t \to z$. Next, we give E_x the same treatment as before, writing it in terms of the slow-varying envelope function $E_\nu \equiv E_x e^{-ikz}$ and time harmonic components:

$$E_x = \int d\nu\, E_\nu e^{i\nu(k_1 z - \omega_1 t) - i\Delta\nu k_u z} + c.c. \tag{2.66}$$

We represent frequency in relative terms with $\nu, \Delta\nu$ as before, with k_1, ω_1 corresponding to the fundamental harmonic. The abbreviation *c.c.* refers to the complex conjugate. Inserting this definition into Eq. (2.65) and following the same steps leading up to Eq. (2.50) yields one of the longitudinal equations of motion:

$$\frac{\mathrm{d}\eta}{\mathrm{d}z} = \sum_{h \text{ odd}} \frac{eK[JJ]_h}{2\gamma_r^2 mc^2} \int d\nu\, E_\nu e^{i\nu\theta} + c.c. \tag{2.67}$$

in terms of relative energy $\eta \equiv (\gamma - \gamma_r)/\gamma_r$. In the exponent of $e^{i\nu\theta}$, we switched to the ponderomotive phase θ, which we shall discuss next.

From Eqs. (2.65) and (2.66), we find the term

$$\cos(k_u z) e^{i\nu(k_1 z - \omega_1 t)} \sim \exp((\pm k_u + k_1)z - \omega_1 t) \tag{2.68}$$

which results from multiplying the cosine particle velocity term against with the plane wave representation of the radiation field. We extract resulting phase term

$$\theta = (k_u + k_1)z - \omega_1 t, \tag{2.69}$$

where t is the particle time coordinate discussed in Eq. (2.41) with two modifications[6]. The first change is to average out the fast-moving particle oscillation proportional to $\sin(2k_u z)$, and the second is to include v_z deviations due to transverse particle velocity $\vec{\boldsymbol{v}}_\perp$. With these changes, we find

$$\begin{aligned} \theta &= (k_u + k_1)z - k_1 z\left(1 + \frac{1+K^2/2}{2\gamma^2} + \frac{1}{2}\left(\vec{\boldsymbol{x}}'^2 + k_\beta^2\vec{\boldsymbol{x}}^2\right)\right) && (2.70)\\ &= k_u z - k_1 z\left(\frac{1+K^2/2}{2\gamma_r^2}(1-2\eta) + \frac{1}{2}\left(\vec{\boldsymbol{x}}'^2 + k_\beta^2\vec{\boldsymbol{x}}^2\right)\right) && (2.71)\end{aligned}$$

where k_β describes the transverse betatron motion of the electrons (more on that later). In the second step we expanded $1/2\gamma^2 \approx (1-2\eta)/2\gamma_r^2$ for small η. Then,

$$\frac{\mathrm{d}\theta}{\mathrm{d}z} = 2k_u\eta - \frac{k_1}{2}\left(\vec{\boldsymbol{x}}'^2 + k_\beta^2\vec{\boldsymbol{x}}^2\right). \tag{2.72}$$

Notice the relationship

$$\frac{\mathrm{d}\eta}{\mathrm{d}z} \sim \sin\theta \quad \text{and} \quad \frac{\mathrm{d}\theta}{\mathrm{d}z} \sim \eta. \tag{2.73}$$

These are mathematically analogous to the equations of a physical pendulum. Figure 2.3 depicts particle evolution in longitudinal phase space. The dashed lines represent the phase space separatrix imposed by the radiation field. Since the vertical axis measures energy, the up-down movement of the electrons represent energy exchange with the radiation field—up implies radiation energy loss, down implies radiation energy gain. Over time, the electrons are observed to follow phase space trajectories described by level sets of the system Hamiltonian.

Let us assume an initial electron bunch with a Gaussian distribution in energy and uniform in phase. If the mean relative bunch energy $\eta_0 = 0$ (measured against resonant γ_r of the radiation field), we observe that there can be no net exchange with the field—by

---

[6] The reason for choosing $+k_u$ is elaborated on in [3].

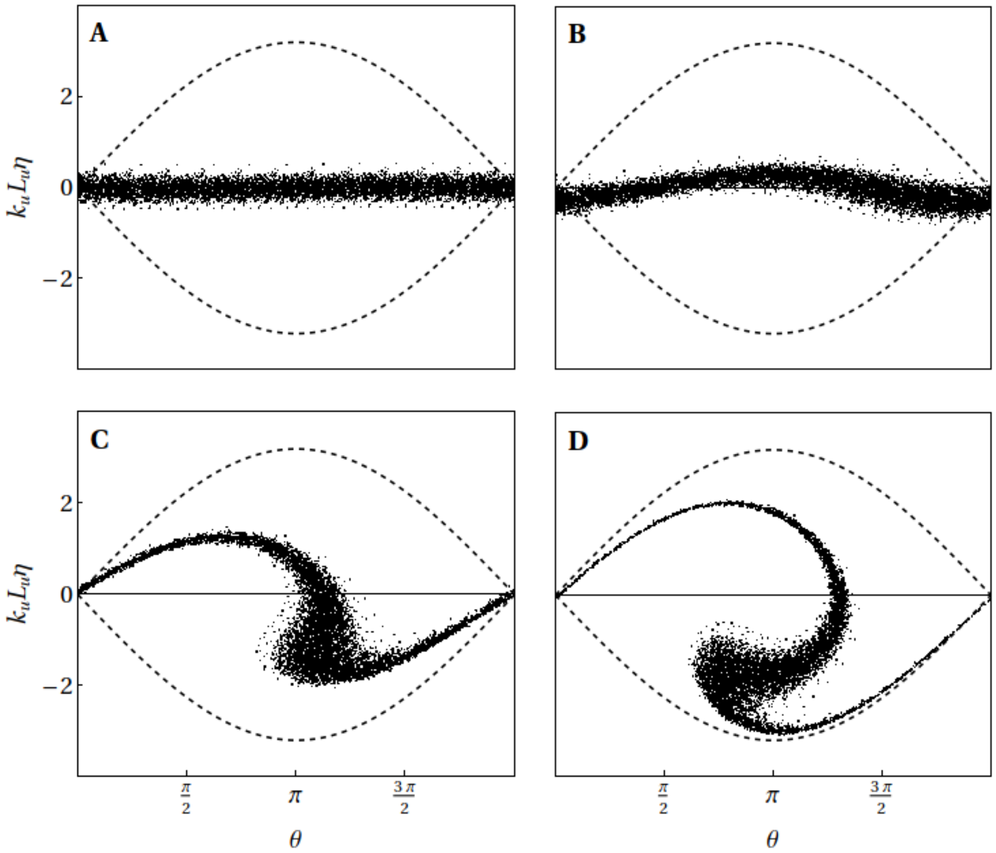

Figure 2.3: Longitudinal phase space evoluition according to the FEL pendulum equations. The radiation field defines the separatrix $\propto \pm\sqrt{E_0}\cos(\theta/2)$, depicted in black dashed lines, about which the particle distribution orbits. From top left to bottom right, the plots show different stages of FEL interaction, namely (A) the beginning, (B) slight energy modulation, (C) maximum microbunching and peak gain, (D) onset of saturation.

symmetry, just as many electrons will gain energy from the field as those which lose energy to it. In order to achieve net gain, η_0 has to be slightly positive. In this case, the phase space trajectories carry more electrons downward than upward (during the initial stage).

This observation implies that gain is maximized when there is a slight detuning between the resonant γ_r and the mean bunch energy γ_0 such that $\gamma_0 - \gamma_r > 0$. We will determine the ideal detuning amount when we derive the 1D gain formula later.

In the transverse domain, the electrons behave as a separate Hamiltonian system, with the transverse equations of motion given by

$$\frac{\mathrm{d}\vec{\boldsymbol{x}}}{\mathrm{d}z} = \vec{\boldsymbol{x}'} \quad \text{and} \quad \frac{\mathrm{d}\vec{\boldsymbol{x}}'}{\mathrm{d}z} = F(\vec{\boldsymbol{x}}, \vec{\boldsymbol{x}'}), \tag{2.74}$$

where F is the external forcing term. Driving forces in the transverse domain arises predominantly due to magnetostatic fields, such as the undulator and external magnets. The focusing due to the undulator is known as *natural focusing*, with an associated length scale (focal length) of

$$\beta_{\text{nat}} \sim \frac{\sqrt{2}\gamma}{K k_u}. \tag{2.75}$$

This typically exceeds the undulator length L_u in the X-ray regime, thus allowing natural focusing to be ignored in analytical approximations. Forcing from external magnets may be written similar to a multipole expansion

$$F(\vec{\boldsymbol{x}}) = a + b\vec{\boldsymbol{x}} + c\vec{\boldsymbol{x}}^2 + d\vec{\boldsymbol{x}}^3 + \ldots, \tag{2.76}$$

associated with (from lowest order) dipoles, quadrupoles, sextupoles, and octupoles. There may also be additional cross terms due to skew quadrupoles and solenoids. Unless otherwise stated, in the following discussion we will assume that only the quadrupole focusing term is present, with an associated strength k_β such that $F(\vec{\boldsymbol{x}}) = -k_\beta^2 \vec{\boldsymbol{x}}$.

Field evolution equation

The field evolution equation follows from the driven Maxwell equation described in Eq. (2.33). Substituting the right hand side for the electron source term yields

$$\left(\frac{\partial}{\partial x} - \frac{i}{2k} \frac{\partial^2}{\partial \vec{\boldsymbol{x}}^2} \right) \tilde{E}_\nu = -\frac{eK[JJ]_h}{4\epsilon_0 \gamma_r \lambda_1} \sum_j e^{-i\nu\theta_j} \delta(\vec{\boldsymbol{x}} - \vec{\boldsymbol{x}}_j). \tag{2.77}$$

Field evolution is thus governed principally by particle phase θ_j and transverse position overlap dictated by $\delta(\vec{\boldsymbol{x}} - \vec{\mathbf{x}}_j)$.

Equations (2.67), (2.72), (2.74), and (2.77) form the complete particle and field equations for the FEL. They are apt to be solved numerically and thus form the basis of most modern FEL codes. In general, it is non-trivial to solve these equations by hand, but there are various approximation methods[7] to determine key quantities of interest. In the next section, we shall explore one such technique with the goal of estimating FEL gain.

2.2.3 Perturbative analysis for low gain

We define FEL gain as

$$G = \frac{U(L_u) - U(0)}{U(0)} \tag{2.78}$$

where $U(z) \equiv |E(z)|^2$ denotes total radiation energy at position z along the undulator. The radiation field E is governed by Eq. (2.77), which in turn depends on the evolution of the particle beam. In the following discussion, we will restrict the problem to the 1D longitudinal domain, before generalizing to 3D afterwards. We can make the problem tractable by taking the following assumptions:

1. Instead of treating the electrons as discrete particles, we approximate the electron bunch as a distribution function $F(\theta, \eta, z)$. Furthermore, we separate this function into a smooth background $\bar{F}(\eta, z)$ with no θ dependence, and the perturbation $\delta F(\theta, \eta, z)$ which arises due to microbunching. In other words, we have $F = \bar{F} + \delta F$. This forms the basis of the perturbative approach.

2. Next, we narrow our focus to the small signal, low gain regime where $G \ll 1$. The small signal regime applies after the initial start-up phase (where the radiation consists mostly of spontaneous emission) but before saturation sets in. This restriction permits

---

[7] See, for instance, Chapters 4 and 5 in [3].

us to drop higher-order terms in E when calculating gain, as well as narrow in on the frequency range near resonance. Note that in high gain ($G \ll 1$) and "mid gain" ($G \sim 1$) cases, the omitted higher-order terms will contribute significantly to the gain calculation, which falls outside the range of validity of this method. It is also important to note that this calculation does not conserve total energy, since energy is a second-order quantity in E. Thus, the result will not be applicable to the saturation phase, where energy-conserving methods are important.

3. (3D case) In the transverse domain, we adopt the simplifying assumption that the electron trajectory is linear with no transverse focusing (including natural focusing and external magnets). In other words,

$$\vec{\boldsymbol{x}}(z) = \vec{\boldsymbol{x}}_0 + \vec{\boldsymbol{p}}(L_u/2 - z), \quad \vec{\boldsymbol{p}}(0) = \vec{\boldsymbol{p}}_0, \tag{2.79}$$

   where $(\vec{\boldsymbol{x}}_0, \vec{\boldsymbol{p}}_0)$ are the electron positions and momenta at the midpoint of the undulator $z = L_u/2$. As discussed previously, natural focusing (Eq. (2.75)) is typically negligible in the X-ray regime. The exclusion of external focusing magnets is also justified in the low gain regime, where the shorter undulator length precludes the need for focusing in the middle of the undulator. Finally, we will also ignore TGU-induced transverse focusing when we examine TGU gain. The justification for that will be provided in the TGU section.

Solving for 1D gain equation

With the stage set, let us examine the evolution equation for F. According to conservative Hamiltonian dynamics, the evolution of F should satisfy the conservation of phase space area along particle trajectories (Liouville's theorem), meaning

$$0 = \frac{\partial F}{\partial z} + \frac{\mathrm{d}\theta}{\mathrm{d}z}\frac{\partial F}{\partial \theta} + \frac{\mathrm{d}\eta}{\mathrm{d}z}\frac{\partial F}{\partial \eta}. \tag{2.80}$$

This is also known as the *continuity equation*. Let us also introduce the longitudinal Fourier transform

$$F_\nu = \frac{1}{2\pi}\int d\theta\, F(\theta) e^{-i\nu\theta}. \tag{2.81}$$

Inserting 1D versions of Eqs. (2.67), (2.72) into Eq. (2.80) and writing $F = \bar{F} + \delta F$ yields

$$0 = \frac{\partial \bar{F}}{\partial z} + \left(\frac{\partial}{\partial z} + 2k_u\eta\frac{\partial}{\partial \theta}\right)\delta F + \chi\left(\int d\nu E_\nu e^{i\nu\theta} + c.c.\right)\frac{\partial}{\partial \eta}\big(\bar{F} + \delta F\big). \tag{2.82}$$

where χ represents the prefactor in Eq. (2.67). We also restrict ourselves to the fundamental harmonic $h = 1$. There are two distinct length scales to this equation: one that varies slowly over many radiation wavelengths, and one that changes rapidly at the scale of λ. We expect the associated terms to vanish separately. Thus, for $\bar{F}$, we find

$$\frac{\partial \bar{F}}{\partial z} = -\chi\int d\nu\left(E_\nu e^{i\nu\theta}\frac{\partial F_\nu}{\partial \eta} + c.c.\right). \tag{2.83}$$

On the scale of the radiation wavelength, we find

$$\left(\frac{\partial}{\partial z} + 2i\nu k_u\eta\right)F_\nu = -\chi E_\nu\frac{\partial \bar{F}}{\partial \eta} \tag{2.84}$$

where we applied the longitudinal FT as defined in Eq. (2.81) to the δF terms. Finally, from Eq. (2.77) we can derive the radiation evolution equation

$$\left(\frac{\partial}{\partial z} + i\Delta\nu k_u\right)E_\nu = -\kappa\int d\eta\, F_\nu \tag{2.85}$$

where κ_h is the prefactor in Eq. (2.77). To proceed, let us write Eqs. (2.84) and (2.85) in the integral form. For a generic equation

$$\left(\frac{\partial}{\partial z} + iA\right) f = B(z), \tag{2.86}$$

we have

$$f(z) = e^{-iAz}\left(f(0) + \int_0^z ds\, e^{-iAs} B(s)\right) \tag{2.87}$$

which follows from applying the chain rule to $\frac{\partial}{\partial z}\left(e^{iAz} f\right)$. Here, $f(0)$ stands for the initial value of f. Applying this to Eqs. (2.84) and (2.85) yields

$$\begin{aligned} E_\nu(z) &= e^{-i\Delta\nu k_u z}\left(E_\nu(0) - \kappa \int_0^z ds \int d\eta\, e^{i(\Delta\nu - 2\nu\eta)k_u s} F_\nu(0)\right. \\ &\left. + \chi\kappa \int_0^z ds\, e^{i(\Delta\nu-2\nu\eta)k_u s} \int_0^s ds'\, e^{2i\nu k_u \eta s'} E_\nu(s') \frac{\partial \bar{F}}{\partial \eta}\right). \end{aligned} \tag{2.88}$$

We can attribute physical significance to the three terms in the above equation. The first term, associated with the initial value of E_ν, represents the seed radiation pulse. The second term, driven entirely by F_ν, represents the spontaneous undulator radiation emitted by the electron bunch. Finally, the third term captures the interaction between the radiation field and the electron bunch, and thus represents the coherent output of the FEL amplification process. In other words, $E_\nu(z) = E_{\mathrm{Seed}} + E_{\mathrm{SR}} + E_{\mathrm{Coh}}$.

To solve for gain, we disregard the spontaneous term E_{SR} and consider only the amplification of the seed $E_{\mathrm{Seed}} + E_{\mathrm{Coh}}$. Next, under the low gain assumption we approximate $E_\nu(s') \sim E_\nu(0)$ in the ds' integral in E_{Coh}. We also define the initial electron energy distribution

$$\bar{F}(\eta) = \frac{1}{\sqrt{2\pi}\sigma_\eta} \exp\left(-\frac{(\eta-\eta_0)^2}{2\sigma_\eta^2}\right) \tag{2.89}$$

with mean energy η_0 and standard deviation σ_η. This allows us to evaluate Eq. (2.88) and

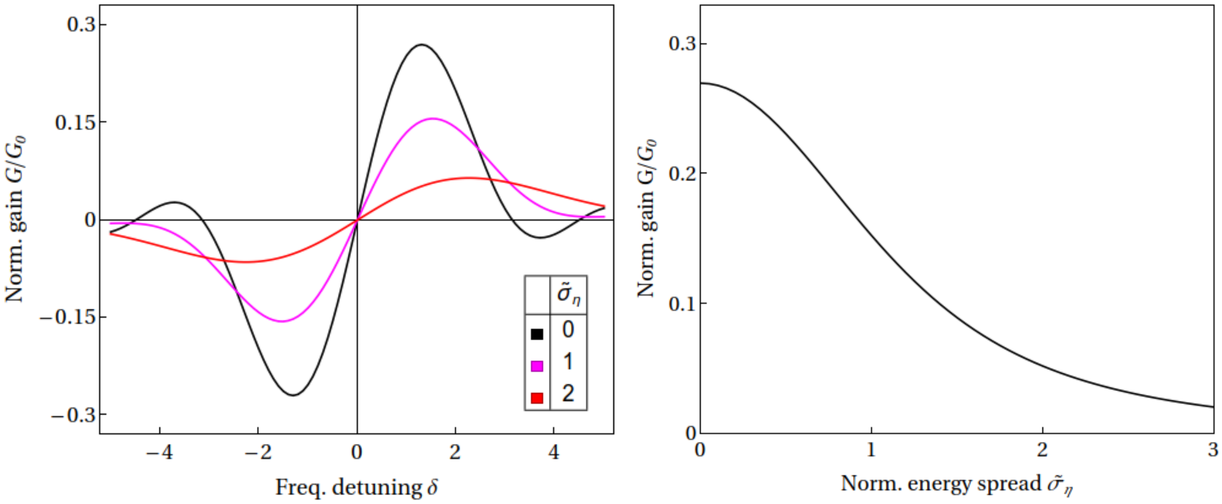

Figure 2.4: *Left:* Plot of 1D normalized gain G/G_0 vs. frequency detuning $\delta \equiv \pi N_u \Delta\nu$, for different normalized energy spreads $\tilde{\sigma}_\eta \equiv 2\pi N_u \sigma_\eta$. With $\tilde{\sigma}_\eta = 0$, peak gain is attained at a slightly positive value of detuning, $\delta \approx 1.3$, with an associated gain bandwidth of $\sim \pi$. By Eq. (2.49), this corresponds to $\sigma_\eta \sim 1/2N_u$. With increasing $\tilde{\sigma}_\eta$, maximum gain is increasingly suppressed. *Right:* Plot of the 1D normalized gain versus $\tilde{\sigma}_\eta$ for $\delta = 1.3$. Notice the rapid falloff of gain with increasing energy spread.

insert into Eq. (2.78) to obtain

$$G = 2\chi\kappa N_e k_u L_u^3 \int_{-L_u/2}^{L_u/2} dz\, ds\, (z-s)\sin(\delta(z-s))\exp\left(-2(\tilde{\sigma}_\eta(z-s))^2\right), \tag{2.90}$$

where we defined the normalized frequency detuning δ and energy spread $\tilde{\sigma}_\eta$ as

$$\delta = 2\pi N_u(\eta_0 - \Delta\nu/2), \tag{2.91}$$

$$\tilde{\sigma}_\eta = 2\pi N_u \sigma_\eta. \tag{2.92}$$

Figure 2.4 shows normalized G plotted against δ and $\tilde{\sigma}_\eta$. We can make several key observations. First, peak gain does not occur at zero detuning, but rather at a slightly positive value of $\delta \approx 1.3$. This is consistent with our understanding of the FEL pendulum equations. If the average electron energy starts at $\eta = 0$, by symmetry the same number of electrons will gain energy from the field as those that lose energy to the field. It is only with a slightly positive mean η that the net energy exchange favors the radiation field.

Second, we note that the width of the main peak scales as $\Delta\delta \sim \pi$. Using Eq. (2.91), this translates to a frequency bandwidth of

$$\sigma_\nu \equiv \frac{\sigma_\omega}{\omega} \sim \frac{1}{N_u} \tag{2.93}$$

for the fundamental harmonic. It is no coincidence that this is precisely the undulator radiation bandwidth, since in the linear low gain approximation the spontaneous undulator emission term $\sim e^{ik_u \Delta\nu z}$ plays a significant role in the amplification term E_{Coh}.

Finally, from the exponent in Eq. (2.90), we observe that G is exponentially suppressed by energy spread due to the $-\tilde{\sigma}_\eta^2$ term (right panel of Fig. 2.4). By visual inspection of the plot, we note that the effective gain bandwidth is $\tilde{\sigma}_\eta \ll 1$ or $\sigma_\eta \ll 1/N_u$. This explains the strict energy spread requirement for the XFELO, where typical values of $1/N_u \sim 10^{-3}$. Compare this to the typical $\sigma_\eta \sim 10^{-3}$ in a storage ring, and we begin to see the need for the TGU in the X-ray regime.

Extension to 3D

Since the longitudinal and transverse dynamics are decoupled, the derivation of 3D gain largely follows the same steps as the 1D analysis. The continuity equation for F now reads

$$0 = \frac{\partial F}{\partial z} + \frac{\mathrm{d}\theta}{\mathrm{d}z}\frac{\partial F}{\partial \theta} + \frac{\mathrm{d}\eta}{\mathrm{d}z}\frac{\partial F}{\partial \eta} + \frac{\mathrm{d}\vec{\boldsymbol{x}}}{\mathrm{d}z}\frac{\partial F}{\partial \vec{\boldsymbol{x}}} + \frac{\mathrm{d}\vec{\boldsymbol{p}}}{\mathrm{d}z}\frac{\partial F}{\partial \vec{\boldsymbol{p}}}. \tag{2.94}$$

As before, the evolution of transverse position and momentum coordinates $(\vec{\boldsymbol{x}}, \vec{\boldsymbol{p}})$ can be obtained directly from the equations of motion Eq. (2.74). Next, we determine the evolution equations for F and E_ν in full 3D, followed by calculating G using the seed E_{Seed} and coherent amplification E_{Coh} terms of the radiation field[8]. The final result for the fundamental

---

[8] The full details of the calculation are presented in Chapter 5.4 of [3].

harmonic is

$$\begin{aligned} G &= \frac{N_e \kappa \chi}{2\pi\lambda^2 P_{\text{in}}} \int d\vec{\boldsymbol{\phi}} d\vec{\boldsymbol{\phi}}' \mathcal{E}_{\nu,\vec{\boldsymbol{\phi}}}(0) \mathcal{E}^*_{\nu,\vec{\boldsymbol{\phi}}'}(0) \int d\vec{\boldsymbol{x}}\, e^{ik\vec{\boldsymbol{x}}\cdot(\vec{\boldsymbol{\phi}}-\vec{\boldsymbol{\phi}}')} \\ &\quad \times \int d\eta\, d\vec{\boldsymbol{p}} \mathcal{U}_\nu(\eta, \vec{\boldsymbol{\phi}} - \vec{\boldsymbol{p}}) \mathcal{U}^*_\nu(\eta, \vec{\boldsymbol{\phi}}' - \vec{\boldsymbol{p}}) \frac{\partial \bar{F}(0)}{\partial \eta}. \end{aligned} \tag{2.95}$$

Here, P_{in} represents the initial beam power. The radiation field is given in the angular-frequency representation $\mathcal{E}_{\nu,\vec{\boldsymbol{\phi}}}(z)$ with the subscripts corresponding to the respective coordinate. We also introduced the undulator radiation field

$$\mathcal{U}_\nu(\eta, \vec{\boldsymbol{x}}(z), \vec{\boldsymbol{\phi}} - \vec{\boldsymbol{p}}) = \int_{-L_u/2}^{L_u/2} dz\, \exp\left[-ik\vec{\boldsymbol{\phi}} \cdot \vec{\boldsymbol{x}}(z) - ikz(\vec{\boldsymbol{\phi}} - \vec{\boldsymbol{p}})^2/2 + ik_u z(2\nu\eta - \Delta\nu)\right], \tag{2.96}$$

where $\vec{\boldsymbol{x}}(z)$ represents the electron trajectory. Notice the direct connection of Eq. (2.96) to the result Eq. (2.50) in our discussion of undulator radiation. Substituting the electron trajectories under the no-focusing assumption (Eq. (2.79)) into Eq. (2.96) results in the $\mathcal{U}_\nu(\eta, \vec{\boldsymbol{\phi}} - \vec{\boldsymbol{p}})$ factors in the gain integral.

We can also rewrite the gain equation Eq. (2.95) in terms of the radiation brightness functions, as defined in Eq. (2.28). In this form, the gain equation is also known as the *gain convolution theorem* [3, 26]:

$$G = \frac{N_e \kappa \chi}{\lambda^2} \frac{\int d\eta d\vec{\boldsymbol{x}} d\vec{\boldsymbol{\phi}} d\vec{\boldsymbol{x}} d\vec{\boldsymbol{y}} B_E(\vec{\boldsymbol{y}}, \vec{\boldsymbol{\phi}}) B_U(\eta, \vec{\boldsymbol{x}} - \vec{\boldsymbol{y}}, \vec{\boldsymbol{\phi}} - \vec{\boldsymbol{p}}) \frac{\partial}{\partial \eta} \bar{F}(\eta, \vec{\boldsymbol{x}}, \vec{\boldsymbol{p}})}{\int d\vec{\boldsymbol{\phi}} d\vec{\boldsymbol{y}} B_E(\vec{\boldsymbol{y}}, \vec{\boldsymbol{\phi}})} \tag{2.97}$$

Here, B_E is the brightness of the seed radiation field $\mathcal{E}_{\nu,\vec{\boldsymbol{\phi}}}(0)$, B_U is the brightness of the undulator radiation field $\mathcal{U}_\nu$, and $\bar{F}$ describes the electron beam distribution. Thus, under the small signal no-focusing assumption, gain is essentially the convolution of the radiation and electron brightness distributions. This result will be essential to our analysis of TGU gain later on.

Let us consider the scenario where the initial seed radiation and electron beams are both

Gaussian, i.e.

$$\bar{F} = \frac{1}{(2\pi)^{5/2}\sigma_\eta\sigma_x\sigma_y\sigma_{px}\sigma_{py}} \exp\left(-\frac{\eta^2}{2\sigma_\eta} - \frac{x^2}{2\sigma_x^2} - \frac{y^2}{2\sigma_y^2} - \frac{p_x^2}{2\sigma_{px}^2} - \frac{p_y^2}{2\sigma_{py}^2}\right) \tag{2.98}$$

$$B_E = \frac{1}{(2\pi)^2\sigma_{rx}\sigma_{ry}\sigma_{\phi x}\sigma_{\phi y}} \exp\left(-\frac{r_x^2}{2\sigma_{rx}^2} - \frac{r_y^2}{2\sigma_{ry}^2} - \frac{\phi_x^2}{2\sigma_{\phi x}^2} - \frac{\phi_y^2}{2\sigma_{\phi y}^2}\right), \tag{2.99}$$

where $\sigma_x, \sigma_y, \sigma_{px}, \sigma_{py}$ represent the RMS electron transverse sizes in positions and momenta respectively. Similarly $\sigma_{rx}\sigma_{ry}, \sigma_{\phi x}, \sigma_{\phi y}$ give the RMS spot sizes in position and angle for the seed radiation beam. Substituting these definitions into Eq. (2.97) yields

$$G = 2\chi\kappa N_e k_u L_u^3 \int_{-1/2}^{1/2} dz\, ds\, \frac{i(z-s)}{\sqrt{\mathfrak{D}_x\mathfrak{D}_y}} \exp\left[-2i\delta(z-s) - 2\tilde{\sigma}_\eta^2(z-s)^2\right], \tag{2.100}$$

with the diffraction factors $\mathfrak{D}_{x,y}$ defined as

$$\mathfrak{D}_{x,y} = \Sigma_{x,y}^2 + sz\, L_u^2\Sigma_{\phi x,y}^2 - iL_u(z-s)\left[\frac{1}{4k_1} + k_1\Sigma_{\phi x,y}^2\Sigma_{x,y}^2\right], \tag{2.101}$$

$$\Sigma_{x,y}^2 = \sigma_{x,y}^2 + \sigma_{rx,ry}^2, \tag{2.102}$$

$$\Sigma_{\phi x,y}^2 = \sigma_{px,y}^2 + \sigma_{\phi x,y}^2. \tag{2.103}$$

The presence of $\mathfrak{D}_{x,y}$ in the denominator in Eq. (2.100) acts to dilute gain when diffraction effects are large. Maximum gain is achieved when there is tight overlap between the radiation and electron beams ($\beta_{x,y} = Z_{Rx,Ry}$). Notice that Eq. (2.100) reduces correctly to Eq. (2.90) when we take the 1D limit $\Sigma_{\phi x,y} \to 0$ and $L_u/k\Sigma_{x,y}^2 \ll 1$. The impact of frequency detuning δ and energy spread $\tilde{\sigma}_\eta$ remains the same as the 1D case.

Thus with Eq. (2.100), we have arrived at a practical low gain formula that can be optimized based on beam parameters. The derivation of the TGU low gain formula in Chapter 3 will build upon this analysis, with appropriate modifications made to reflect the impact of the TGU on longitudinal FEL dynamics.

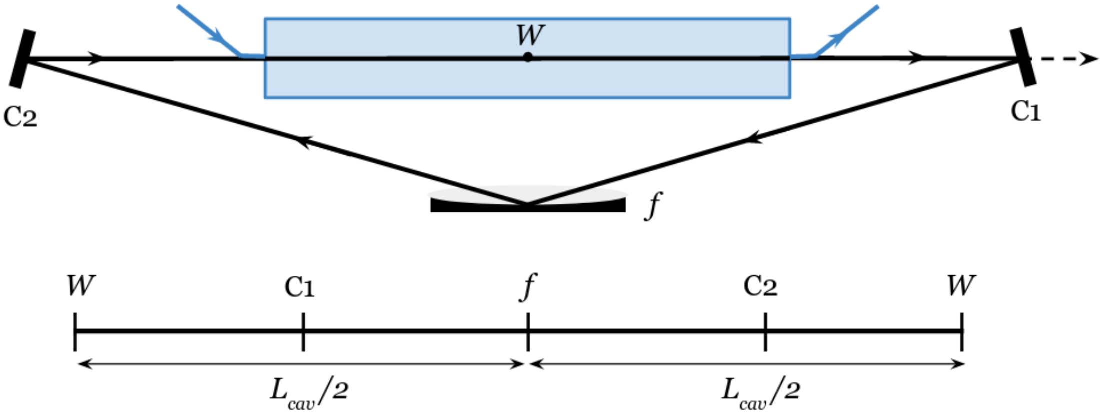

Figure 2.5: Schematic of a two-mirror optical cavity for the XFELO. The cavity consists of two Bragg crystals C1, C2 and a glancing incident angle lens f. The waist W of the cavity is located in the middle of the undulator (blue). The total round trip length is L_{cav}.

2.2.4 X-ray FEL oscillator (XFELO)

The concept of a FEL oscillator (an undulator enclosed within an optical cavity) was conceived and demonstrated not long after the invention of the FEL itself. The term *oscillator* is adopted from conventional laser terminology, referring to the recirculating radiation pulse trapped within the cavity. Typical characteristics of the oscillator include low gain and high cavity quality factor Q, which in turn implies narrow frequency bandwidth and low outcoupling power. This is in contrast to the *amplifier* which is a high gain, high loss device.

In the modern day, FEL oscillators are common and well understood in the IR, optical and UV regimes [18, 24, 27]. It remains a significant challenge to build a robust optical cavity in the X-ray regime. However, with recent advances in technology, the practical implementation of an X-ray FEL oscillator (XFELO) is within reach [12].

Power evolution and frequency narrowing

The simplest cavity configuration for the XFELO consists of two mirrors and a single lens (Fig. 2.5) which trap a recirculating X-ray pulse such that it encounters a fresh electron bunch in the undulator with each round trip (bunch separation T_{bunch} = cavity round trip time T_{cavity}). Let P_n represent radiation pulse power on the nth pass, and P_s represent spontaneous radiation power. Then, we obtain the recursion relation

$$P_n = (1-L)(1+G)P_{n-1} + P_s \tag{2.104}$$

where $L > 0$ is the net cavity round trip loss (in terms of power) and G is the small signal FEL gain. In other words, the radiation during each pass consists of the radiation pulse from the previous pass amplified $(1+G)$ times by seeding the FEL interaction within the undulator and losing $(1-L)$ times traversing the cavity, as well as the spontaneous undulator radiation emitted during the most recent pass. In order for lasing to occur, it is necessary that

$$(1-L)(1+G) > 1. \tag{2.105}$$

Losses in the cavity result from intentional design factors, such as Bragg filtering and outcoupling, as well as imperfections such as crystal absorption. For $L, G \ll 1$, the lasing condition can be approximated as $G - L > 0$. Solving the recursion relation Eq. (2.104) yields

$$P_n = \frac{[(1-L)(1+G)]^n - 1}{(1-L)(1+G) - 1} P_0 \tag{2.106}$$

where P_0 represents the starting radiation power (typically provided by spontaneous radiation P_s). Thus we observe an exponential increase in power with increasing turn number n. It is important to note that this analysis is only valid during the small signal exponential gain phase of the laser. During the initial startup and final saturation phases, gain G is not constant and has a complicated dependance on the electron and X-ray beams.

This exponential gain in power is matched by bandwidth narrowing in frequency space, another hallmark of the lasing process. The narrowing occurs due to two mechanisms:

1. *Bragg filtering.* Mirrors in an X-ray cavity rely on Bragg diffraction to achieve high

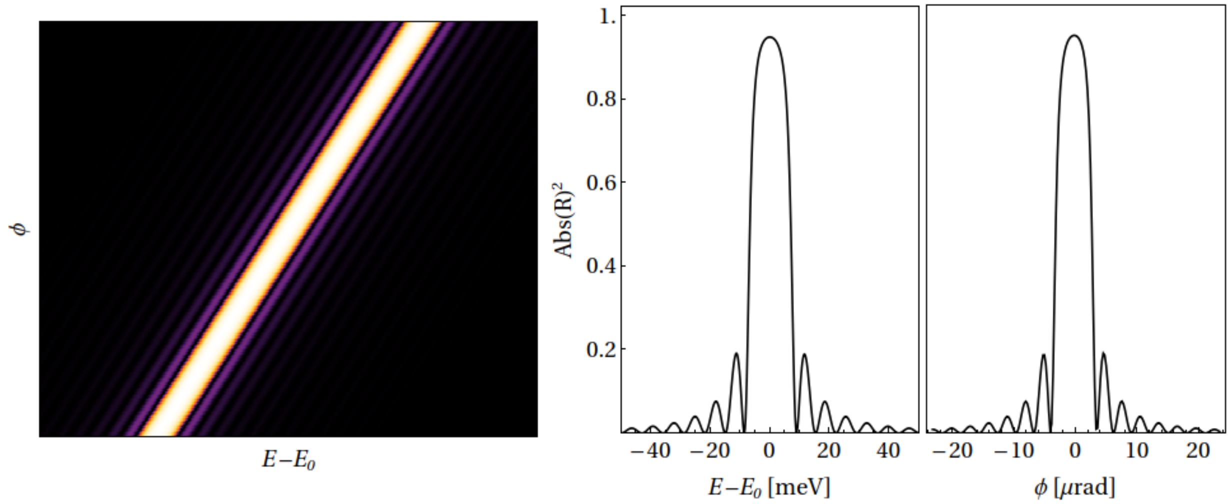

Figure 2.6: *Left:* Plot of crystal reflectivity amplitude $|R|^2$ vs. photon energy $E - E_0$ and angle ϕ. Here, $E_0 = \hbar\omega_0 \approx 14.4\,\mathrm{keV}$ is the Bragg resonant energy. *Right:* Lineouts of $|R|^2$ taken at $\phi = 0$ and $E - E_0 = 0$ respectively. Notice the narrow bandwidths of $\sigma_E \sim 10\,\mathrm{meV}$ (relative bandwidth $\sigma_{\mathrm{refl}} \sim 10^{-6}$) and $\sigma_\phi \sim 5\,\mu\mathrm{rad}$.

reflectivity. The corresponding reflectivity curves $R(\omega, \phi)$ are sharply peaked in frequency and angular space (Fig. 2.6), acting effectively as a narrow bandpass filter on the incident radiation. Over multiple mirror reflections and many cavity turns, the repeated multiplication by R causes the beam to narrow in frequency and angular space.

2. *Gain narrowing.* We expect to observe frequency narrowing in the XFELO even in the absence of Bragg filtering. This is because of the finite FEL gain bandwidth as described by Eq. (2.93). Frequencies at the center of the gain curve will be preferentially amplified over those in the wings. Over many turns, we expect the relative radiation bandwidth to decrease as

$$\left(\frac{\Delta\omega}{\omega}\right)_n \sim \frac{1}{N_u\sqrt{n}}. \tag{2.107}$$

This narrowing stops when the pulse becomes Fourier-limited longitudinally. In the temporal domain, one can think of the frequency narrowing as the increase in coherence length by $\sim N_u\lambda$ per turn until it encompasses the entire pulse.

In the X-ray regime, we expect Bragg filtering to dominate since the effective cavity bandwidth $\sigma_{\text{refl}} \sim 10^{-6}$ is many orders of magnitude less than the gain bandwidth $1/N_u \sim 10^{-3}$. The reader might wonder if the more stringent crystal bandwidth has an impact on the electron energy spread requirement. This will not be the case as the FEL amplification process in the undulator occurs independently of the crystal filtering in the optical cavity. In a metaphorical sense, FEL amplification acts as a "rising tide that lifts" all frequencies in the range $\sim 1/N_u$. It is only in the optical cavity that frequencies outside of the much narrower σ_{refl} are filtered.

One last note before moving on: although both the effective cavity bandwidth and gain bandwidth also have angular dependance, they are not significant sources of angular narrowing in the XFELO. Rather, the primary determining factors of the transverse mode size are the cavity geometry and focal lengths. We will discuss this later when we examine the transverse design of the cavity.

Start-up and saturation

The exponential power growth discussed in the previous section does not apply during the very earliest and latest stages of the XFELO. During the initial start-up phase, radiation power is dominated by spontaneous emission within the $1/N_u \sim 10^{-3}$ bandwidth. Let us split this emission bandwidth into two regions: (a) those existing within the crystal bandwidth σ_{refl}, and (b) those existing outside σ_{refl}.

The vast majority of the spontaneous emission belongs to the region B and is therefore filtered by the crystal. Round trip loss for this region is very large, $L \sim 1$, and gain is almost nil. On the other hand, for the small range of frequencies in region A, loss is minimal $L = 1 - |R|^2 \sim 0$ and gain is close to the theoretical value (as set by the gain function). Over many turns, the initially small signal in region A is exponentially amplified and dominates over region B. At this stage, the exponential gain regime discussed in the previous section sets in.

The exponential gain phase eventually gives way to saturation, when the radiation pulse energy peaks and gain falls back towards zero. This is because the FEL amplification process comes at a cost to electron energy spread. The amount of energy spread growth is given by[9]

$$\Delta\sigma_\eta \propto -2\int_{\eta_0}^{\eta_1} d\eta \, \frac{\partial S(\omega,\eta)}{\partial\omega} \tag{2.108}$$

where (η_0, η_1) represent the initial and final average bunch energies, and $S(\omega,\eta) \propto |\mathcal{E}|^2$ is the on-axis power spectrum of the undulator emission from Eq. (2.55). In other words, energy spread growth $\Delta\sigma_\eta$ is proportional to total field energy $|\mathcal{E}|^2$. As the radiation field grows in power, each interaction with the electron bunch results in increasing disruption to its energy spread. This reduces the FEL gain for the next turn. Eventually, the falling gain is overtaken by cavity loss such that the lasing condition Eq. (2.105) is no longer fulfilled. At this point, the XFELO has reached saturation.

In the short term post-saturation phase, radiation power falls exponentially as a result of unmitigated cavity loss. In the long term, the fate of the radiation field is determined by the electron source. We will re-examine this topic when we discuss ring-FEL dynamics.

Transverse design

The transverse design of the XFELO cavity is analogous to that of conventional optical cavities. For now, let us restrict our discussion to a single transverse dimension. Under the ABCD ray transfer matrix convention, the transverse position x and angle ϕ of a ray can be expressed as a vector $\vec{\boldsymbol{r}} = \begin{pmatrix} x \\ \phi \end{pmatrix}$. Diffraction and focusing can then be written as matrix

---

[9] This is also known as Madey's first theorem [1].

operations

$$D(\ell) = \begin{pmatrix} 1 & \ell \\ 0 & 1 \end{pmatrix}, \qquad F(f) = \begin{pmatrix} 1 & 0 \\ -1/f & 0 \end{pmatrix}, \tag{2.109}$$

where ℓ is the drift length and f is the focal length under the thin lens approximation. The round-trip matrix for the 2-mirror cavity (Fig. 2.5) would be

$$M_{\text{2mirr}} = D(L_{\text{cav}}/2)F(f)D(L_{\text{cav}}/2) \tag{2.110}$$

where L_{cav} is the total round-trip length. In general, an optical cavity is stable if $|\mathrm{Tr}\, M| < 2$, where M is the periodic round-trip matrix. For the 2-mirror cavity, this reduces to $f > L_{\text{cav}}/4$ for $f > 0$ and $L_{\text{cav}} > 0$.

We can also determine the size of the stable Gaussian mode supported in the cavity. Let us define the second-order beam moment matrix

$$\Sigma = \begin{pmatrix} \sigma_r^2 & \sigma_{r\phi}^2 \\ \sigma_{\phi r}^2 & \sigma_\phi^2 \end{pmatrix} \tag{2.111}$$

where σ_r, σ_ϕ are the RMS beam size and angular divergence respectively, and $\sigma_{r\phi}^2, \sigma_{\phi r}^2$ are the covariance terms. Then the stable mode has to satisfy

$$\Sigma_{\text{final}} = M\Sigma_{\text{initial}}M^T \tag{2.112}$$

where $\Sigma_{\text{final}}, \Sigma_{\text{initial}}$ denote the initial and final beam states after one cavity round trip, and superscript T denotes matrix transpose. For the 2-mirror cavity, this reduces to the relationship

$$Z_R = \sqrt{L_{\text{cav}} f - \frac{L_{\text{cav}}^2}{4}} \tag{2.113}$$

where $Z_R \equiv \sigma_r/\sigma_\phi$ is the Rayleigh range of the stable mode. Thus for a given target Z_R

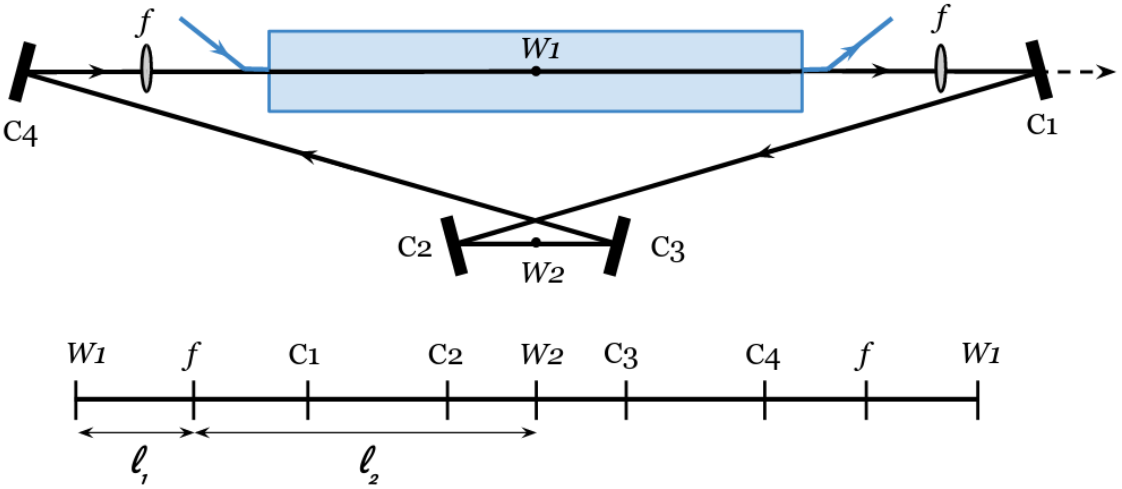

Figure 2.7: Schematic of a four-mirror optical cavity in the bowtie configuration, consisting of four Bragg mirrors C1 through C4 and two lenses with identical focal lengths f. The first waist W1 is located on the long straight section with the undulator (blue), whereas the second waist W2 is located on the short straight section between C2 and C3. Total round trip length is $L_{\text{cav}} = 2\ell_1 + 2\ell_2$.

(for instance, to maximize overlap with electron betatron function), Eq. (2.112) allows us to choose appropriate f and L_{cav} to support that mode.

A significant drawback of the 2-mirror cavity is that it does not allow for on-the-fly frequency tunability without significantly altering the round-trip length. The 4-mirror bowtie cavity (Fig. 2.7) offers a solution. The resonant frequency can be tuned by adjusting the angle of incidence on all four mirrors, while simultaneously keeping the path length constant by translating the two mirrors on the shorter straight section. There are two waist locations, at the midpoint of the long (waist W1) and short (waist W2) straight sections respectively. The undulator midpoint matches W1 and the lenses are positioned symmetrically about W1.

Let us calculate the stability condition and stable modes of this cavity. The round-trip matrix is given by

$$M_{4\text{mirr}} = D(\ell_1)F(f)D(2\ell_2)F(f)D(\ell_1) \tag{2.114}$$

where ℓ_1, ℓ_2 indicate the distances from W1 to the first lens, and the first lens to W2 respectively. Both lenses are assumed to have the same focal length f. Enforcing the stability condition $|\mathrm{Tr}\, M_{4\mathrm{mirr}}| < 2$ results in

$$0 < \left(\frac{\ell_1}{f} - 1\right)\left(\frac{\ell_2}{f} - 1\right) < 1 \tag{2.115}$$

for $f > 0$. The stable mode can be calculated from Eq. (2.112) to obtain

$$Z_{R1} = \sqrt{\frac{\ell_1 - f}{\ell_2 - f}(f(\ell_1 + \ell_2) - \ell_1\ell_2)}, \qquad Z_{R2} = \frac{\ell_2 - f}{\ell_1 - f} Z_{R1}. \tag{2.116}$$

where Z_{R1}, Z_{R2} are the stable Rayleigh ranges at waists 1 and 2 respectively. Note that solutions to Eq. (2.116) are not unique. In Section 5.1, we will return to these formulas when we design the oscillator cavity.

2.3 Storage ring physics

In this section, we will introduce basic accelerator physics concepts relevant to the operation of the storage ring driven XFELO. In particular, we will place emphasis on transverse storage ring damping dynamics and equilibrium emittance.

A more comprehensive treatment of storage ring and accelerator physics is available in many textbooks, including [28–30]. The author would like to credit [29, 30] for the following discussion.

2.3.1 Linear betatron motion

Transfer matrix and tune

The linear ABCD ray transfer matrix analysis used in our discussion of the XFELO is also useful in accelerator physics. A direct analog can be made between particle trajectories $(\vec{\boldsymbol{x}}, \vec{\boldsymbol{p}})$ and optical ray vectors $(\vec{\boldsymbol{r}}, \vec{\boldsymbol{\phi}})$. In general, for any linear element or sequence of elements in an accelerator, we can define the *transfer matrix* as

$$M = \begin{pmatrix} \cos\phi + \alpha\sin\phi & \beta\sin\phi \\ -\gamma\sin\phi & \cos\phi - \alpha\sin\phi \end{pmatrix} \tag{2.117}$$

where β, α, γ are the Courant-Snyder parameters introduced in the beginning of this chapter. The phase advance ϕ is defined as

$$\phi \equiv \int_0^L \frac{ds}{\beta(s)}. \tag{2.118}$$

The integral is performed over the entire length L of the section of interest. Consequently, the phase advance for one complete turn in a storage ring is given by

$$\nu \equiv \frac{1}{2\pi} \oint \frac{ds}{\beta(s)} \tag{2.119}$$

over the entire ring. This is also known as the *tune*. Qualitatively, ν describes how many oscillations of β occurs over the ring, and is not necessarily a whole number. In fact, it is advantageous for ring stability that the decimal part of the tune, also known as the *fractional tune*, be close to an irrational fraction.

Eq. (2.117) allows us to track the motion of electron trajectories provided starting parameters β, α, γ and the pre-calculated phase advance ϕ (or equivalently tune ν for the entire ring). To illustrate, let us use the classic example of the FODO cell, consisting of a focusing dipole and a defocusing dipole with identical focal lengths f and a fixed separation distance L. If we start our analysis in the middle of the focusing dipole, we can write the transfer matrix as

$$
\begin{aligned}
M_{\text{FODO}} &= \begin{pmatrix} 1 & 0 \\ -\frac{1}{2f} & 1 \end{pmatrix} \begin{pmatrix} 1 & L \\ 0 & 1 \end{pmatrix} \begin{pmatrix} 1 & 0 \\ \frac{1}{f} & 1 \end{pmatrix} \begin{pmatrix} 1 & L \\ 0 & 1 \end{pmatrix} \begin{pmatrix} 1 & 0 \\ -\frac{1}{2f} & 1 \end{pmatrix} && (2.120) \\
&= \begin{pmatrix} 1 - \frac{L^2}{2f^2} & 2L\left(1 + \frac{L}{2f}\right) \\ -\frac{L}{2f}\left(1 - \frac{L}{2f}\right) & 1 - \frac{L^2}{2f^2} \end{pmatrix}. && (2.121)
\end{aligned}
$$

The stability condition $|\mathrm{Tr}\, M_{\text{FODO}}| < 2$ then requires that $0 < L < 2f$, for $f > 0$. Using Eq. (2.117), we can identify the phase advance

$$\phi = \cos^{-1}\left(1 - \frac{L^2}{2f^2}\right), \tag{2.122}$$

and

$$\beta = \frac{2L(1 + \sin(\phi/2))}{\sin\phi}, \qquad \alpha = 0. \tag{2.123}$$

It follows that the phase advance over n identical FODO cells is $n\phi$, and a ring consisting of N copies of this FODO cell would have $\nu = N\phi/2\pi$.

Dispersion and momentum compaction

The preceding discussion assumed that all electrons have the nominal design momentum p_0. In reality, the electron bunch consists of particles distributed around p_0 with relative momentum deviations $\eta \equiv (p - p_0)/p_0$. (In an electron storage ring where $v_z \approx c$, η is equivalently defined as the relative energy deviation $(\gamma - \gamma_0)/\gamma_0$ where γ_0 is the nominal Lorentz factor.) The response of a transverse magnetic element can be dependant on η. For instance, in the bending dipole, higher momentum particles are deflected less than their lower momentum counterparts.

This behavior is characterized by the *dispersion function* D. We decompose the transverse particle trajectory $x(s)$ into two parts:

$$x(s) = x_\beta(s) + D(s)\eta \tag{2.124}$$

where x_β is the design betatron trajectory in the absence of off-momentum particles. Dispersion $D(s)$ effectively acts as an additional linear component of the particle trajectory.

We can derive a transfer matrix for D, similar to Eq. (2.117). Let us define the dispersion vector $(D, D', 1)$. Then the dispersion transfer matrix is given by

$$M = \begin{pmatrix} M_{11} & M_{12} & M_{13} \\ M_{21} & M_{22} & M_{23} \\ 0 & 0 & 1 \end{pmatrix} \tag{2.125}$$

where the upper 2x2 square matrix consisting of $M_{11}, M_{12}, M_{21}, M_{22}$ is identical to Eq. (2.117) and

$$\begin{aligned} M_{13} &= D(1 - \cos\phi - \alpha\sin\phi) - D'\beta\sin\phi, \qquad (2.126) \\ M_{23} &= D\gamma\sin\phi + D'(1 - \cos\phi + \alpha\sin\phi). \qquad (2.127) \end{aligned}$$

The entries M_{13} and M_{23} characterize orbit deviations due to momentum deviation η. For instance, for a bending dipole under the small angle approximation,

$$M_{\text{dip}} = \begin{pmatrix} 1 & L & \frac{L\theta}{2} \\ 0 & 1 & \theta \\ 0 & 0 & 1 \end{pmatrix} \tag{2.128}$$

where L, θ are the dipole length and bending angle respectively.

From Eq. (2.124), we observe that non-zero dispersion has a detrimental impact on beam size and hence beam brightness:

$$\sigma_x^2 = \sigma_{x,\beta}^2 + D^2\sigma_\eta^2 \tag{2.129}$$

where $\sigma_{x,\beta} = \sqrt{\beta\varepsilon_x}$ is the RMS spot size due to betatron motion alone. Much effort is devoted to eradicating dispersion in the straight sections of a ring, where undulators, RF cavities, injection/extraction segments and other important devices are located.

The elimination of dispersion is equivalent to $M_{13} = M_{23} = 0$. A lattice with this property is known as an *achromat.* The simplest example of an achromatic system is the double bend achromat (DBA), consisting of two bending dipoles sandwiching a dispersion-matching section. This allows the two ends of the DBA to have zero dispersion straight sections. Since then, more sophisticated systems with up to 7 bends, also known as multi-bend achromats (MBAs), have been demonstrated [31]. It can be said that the proliferation of MBAs is one of the key contributors to the rise of the 4th generation storage ring.

We round out the discussion of momentum deviation by introducing the *momentum compaction factor* α_c. This is defined as

$$\alpha_c \equiv \frac{1}{C}\frac{\mathrm{d}C}{\mathrm{d}\eta} = \frac{1}{C}\oint \frac{D(s)}{\rho}\,ds \tag{2.130}$$

where C, ρ are the ring circumference and radius of curvature respectively. Effectively, α_c relates the relative longitudinal path difference $\Delta C/C$ to momentum deviation η:

$$\frac{\Delta C}{C} = \alpha_c\eta. \tag{2.131}$$

It is the counterpart to dispersion D in the longitudinal domain.

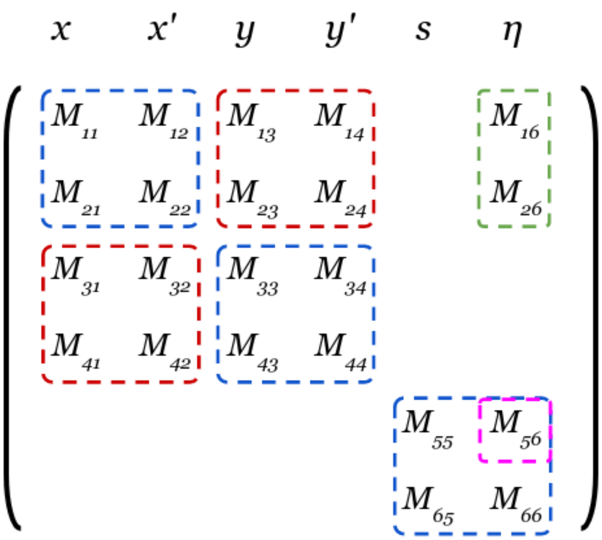

Figure 2.8: Sketch of the 6D beam transport matrix M with non-zero entries labelled. The diagonal 2x2 entries (blue dashed) represent horizontal, vertical, and longitudinal dynamics respectively. Transverse skew terms are given in the off-diagonal 2x2 squares (red). The dispersion terms correspond to entries M_{16}, M_{26} (green). Finally, the entry M_{56} (magenta) holds special significance as the momentum compaction factor α_c.

6D transport matrix

As discussed in the introduction to this chapter, the complete description of particle state in the 6D phase space is given by $\vec{\boldsymbol{A}} \equiv (x, x', y, y', s, \eta)$, where s denotes longitudinal distance relative to the reference particle. The linear transport of state vector $\vec{\boldsymbol{A}}$ is given by

$$A_i = \sum_j M_{ij} A_j, \tag{2.132}$$

where M_{ij} are the entries of the 6D linear transport matrix (Fig. 2.8). The 2x2 blocks formed by index pairs (1, 2) and (3, 4) are the horizontal and vertical transport matrices respectively, as defined in Eq. (2.117). The 2x2 matrix for the (5, 6) pair describes synchrotron motion. In particular, notice that $M_{56} = \alpha_c$.

The entries M_{16}, M_{26} correspond to the dispersion terms Eqs. (2.126) and (2.127). Dispersion is not present in the vertical direction in a flat ring, i.e. $M_{36} = M_{46} = 0$. However, the effect of dispersion can make its way into vertical emittance via the linear coupling terms $M_{13}, M_{23}, M_{14}, M_{24}$. Intentional linear coupling can be introduced with elements such as skew quadrupoles and solenoids.

Particle tracking in a storage ring can be greatly simplified provided we can specify M from design parameters such as the Courant-Snyder parameters, tunes, dispersion and momentum compaction. This is the basis of the `ILMATRIX` propagation element in the particle tracking code `elegant`, which we will revisit in the Simulations chapter.

2.3.2 Radiation damping and equilibrium

As electrons traverse the bending sections of the storage ring, they emit spontaneous radiation. The rate of power loss is given by

$$P_\gamma = \frac{cC_\gamma}{2\pi}\frac{U^4}{\rho^2}, \tag{2.133}$$

where U is the electron energy and ρ is the local radius of curvature. The constant C_γ is defined as

$$C_\gamma = \frac{4\pi}{3}\frac{r_e}{(mc^2)^3} = 8.85 \times 10^{-5}\,\mathrm{m}/(\mathrm{GeV})^3. \tag{2.134}$$

To find total energy loss per turn, we integrate around the ring to obtain

$$U_0 = \frac{C_\gamma U^4}{2\pi}\oint \frac{ds}{\rho(s)^2}. \tag{2.135}$$

Longitudinal damping

Eq. (2.135) gives the total energy loss of a reference particle with energy $\gamma = \gamma_0$. Since off-energy particles follow a slightly different trajectory due to dispersion, their rate of energy loss will be slightly different. Let us evaluate the energy loss

$$U_{\rm rad} = \oint P_\gamma \, dt = \frac{1}{c} \oint P_\gamma \left(1 + \frac{D\eta}{\rho} \right) ds. \tag{2.136}$$

The sensitivity of $U_{\rm rad}$ to particle energy E is then given by

$$\frac{\mathrm{d}U_{\rm rad}}{\mathrm{d}E} = \frac{U_0}{E_0} \left(2 + \frac{1}{cU_0} \oint \left[D P_\gamma \left(\frac{1}{\rho} + \frac{2}{B} \frac{\mathrm{d}B}{\mathrm{d}x} \right) ds \right]_{E_0} \right) \tag{2.137}$$

where B is the magnetic field strength and the subscript E_0 denotes the evaluating the derivative at $E = E_0$. The second term with the integral is also known as the *damping partition* $\mathcal{D}$. Let us define the radiation integrals

$$\begin{aligned} I_2 &= \oint \frac{ds}{\rho^2}, & (2.138) \\ I_4 &= \oint \frac{D}{\rho} \left(\frac{1}{\rho^2} + \frac{2}{B\rho} \frac{\mathrm{d}B}{\mathrm{d}x} \right) ds. & (2.139) \end{aligned}$$

These are standard integrals commonly used by the storage ring community, and can be readily calculated for a given machine lattice. Then Eq. (2.137) can be rewritten as

$$\frac{\mathrm{d}U_{\rm rad}}{\mathrm{d}E} = \frac{U_0}{E_0} \left(2 + \mathcal{D} \right), \qquad \mathcal{D} = I_4/I_2. \tag{2.140}$$

Typical values of $\mathcal{D}$ are positive but substantially less than unity. Thus, Eq. (2.140) implies that higher energy particles radiate more than the reference particle, while lower energy particles radiate less. Over many turns, the result is a gradual reduction in energy spread. The damping rate α_s can be calculated from the rate of energy loss. The result is

$$\alpha_s = \frac{1}{2T_0} \frac{\mathrm{d}U_{\rm rad}}{\mathrm{d}E} = \frac{U_0}{2T_0 E_0} (2 + \mathcal{D}), \tag{2.141}$$

where T is the ring period and the subscript 0 denotes values for the reference particle. This corresponds to a damping time constant

$$\tau_s = \frac{1}{\alpha_s} = \frac{2T_0 E_0}{U_0(2+\mathcal{D})}. \tag{2.142}$$

Typical values of τ_s for a large storage ring are on the order of tens to hundreds of milliseconds.

Vertical damping

For the following discussion, let us assume that the electron is following a betatron orbit parametrized by

$$y = A_y \cos\phi, \qquad y' = -\frac{A_y}{\beta}\sin\phi, \qquad A_y^2 = y^2 + (\beta y')^2, \tag{2.143}$$

where A_y, ϕ are the amplitude and phase of the betatron oscillation respectively.

Recall that spontaneous emission from a relativistic electron is focused in a narrow cone with opening angle $\sim 1/\gamma$ in the forward direction. Therefore let us approximate that the resulting momentum change $\delta\vec{\boldsymbol{p}}$ from one spontaneous emission event is parallel to the instantaneous electron momentum $\vec{\boldsymbol{p}}$. To first order, the betatron orbit of the electron remains unaffected.

The electron recuperates the lost momentum in the RF cavities, where the accelerating force is parallel to the design orbit. In general, the recovered momentum is not parallel to $\delta\vec{\boldsymbol{p}}$, and results in a change in the slope of the orbit trajectory. The change in slope y' is given by

$$\delta y' = -y'\frac{\delta p}{p} = -y'(\delta\eta). \tag{2.144}$$

Then the average change in betatron amplitude A_y is

$$\langle \delta A_y \rangle = -\frac{\langle (\beta y')^2 \rangle}{A_y} \frac{U_0}{E_0}. \tag{2.145}$$

Since betatron motion is sinusoidal, we find $\langle (\beta y')^2 \rangle = A_y^2/2$. Then

$$\frac{\delta A_y}{A_y} = -\frac{U_0}{2E_0} \tag{2.146}$$

This is associated with the damping rate and time constants

$$\alpha_y = -\frac{U_0}{2T_0 E_0}, \qquad \tau_y = -\frac{2T_0 E_0}{U_0}. \tag{2.147}$$

Notice that vertical damping occurs at half the rate of longitudinal damping for a reference electron ($\mathcal{D} = 0$).

Horizontal damping

Horizontal damping follows the same principle as vertical damping but with two complicating factors. The first complication is dispersion. When an electron loses energy $\delta\eta$, its instantaneous position does not change. From Eq. (2.124),

$$0 = \delta x = \delta x_\beta + D(\delta\eta). \tag{2.148}$$

Thus the betatron orbit x_β changes by amount $\delta x_\beta = -D(\delta\eta)$ to compensate. Similarly, the orbit slope x'_β changes by $\delta x'_\beta = -D'(\delta\eta)$.

The second complication arises due to the fact that the electron traverses a longer path length during the outward swing of its betatron orbit than during its inward swing. Therefore a different amount of energy is lost during the two halves of the oscillation. This effect is small but non-negligible. To account for this, we let $P_\gamma(x_\beta)$ be a function of the betatron orbit.

The subsequent calculation of the horizontal damping rate and time constants follows largely the same steps as vertical damping, with the aforementioned modifications. For a detailed account, we refer readers to [30]. The end result is

$$\alpha_x = -\frac{U_0}{2T_0E_0}(1-\mathcal{D}), \qquad \tau_x = -\frac{2T_0E_0}{U_0(1-\mathcal{D})}. \tag{2.149}$$

Damping partition numbers

Let us define the *damping partition numbers*

$$\mathcal{J}_x = 1-\mathcal{D}, \qquad \mathcal{J}_y = 1, \qquad \mathcal{J}_s = 2+\mathcal{D}. \tag{2.150}$$

which allows us to write $\alpha_i = \mathcal{J}_i\alpha_0$ for $i \in \{x, y, s\}$ and $\alpha_0 = -U_0/(2T_0E_0)$. Notice that the damping partition numbers sum to a constant

$$\sum_i \mathcal{J}_i = 4. \tag{2.151}$$

This is also known as *Robinson's theorem* and holds for any configuration of the magnetic lattice, as long as it is independent of electron motion [32]. In the restricted case where the design orbit lies on a perfectly flat horizontal plane with fields symmetric with respect to that plane, we also obtain $\mathcal{J}_x + \mathcal{J}_s = 3$. This would not be true if there is any sort of vertical dependance in the magnetic lattice.

Quantum excitation and equilibrium

Our discussion of radiation damping so far has not dealt with the fact that spontaneous emission is a discrete random process due to the particle nature of light. Each time an electron emits a photon, it experiences a momentary disturbance to its orbit. The occurarnce of emission events is governed by the Poisson distribution, and the sum effect of all the disturbances obey the random walk.

Let u be the induced change in energy due to one photon emission event. The evolution of synchrotron motion amplitude A_s is then given by

$$\frac{\mathrm{d}\left\langle A_s^2\right\rangle}{\mathrm{d}t} = -2\frac{\left\langle A_s^2\right\rangle}{\tau_s} + Nu^2, \tag{2.152}$$

where N is the rate of photon emission. The first term follows from our previous discussion of longitudinal damping. Setting the LHS to zero yields the steady state solution $\left\langle A_s^2\right\rangle = \frac{1}{2}Nu^2\tau_s$, or

$$\sigma_E^2 \equiv \frac{\left\langle A_s^2\right\rangle}{2} = \frac{1}{4}Nu^2\tau_s. \tag{2.153}$$

In reality, photon emission does not take place at a single energy u, nor at a fixed rate N. The number of emitted photons $n(u)$ is a function of energy:

$$n(u) = \frac{P_\gamma}{u_c^2}F\left(\frac{u}{u_c}\right) \tag{2.154}$$

where $u_c = 3\hbar c\gamma^3/2\rho$ is the characteristic photon energy. The function F is an algebraic function

$$F(\xi) = \frac{9\sqrt{3}}{8\pi}\int_\xi^\infty K_{5/3}(\xi')\,d\xi', \tag{2.155}$$

where $K_{5/3}$ is the modified Bessel function. Knowing this, we can calculate the total rate of photon emission

$$\mathcal{N} = \int_0^\infty n(u)\,du = \frac{15\sqrt{3}}{8}\frac{P_\gamma}{u_c}. \tag{2.156}$$

In addition,

$$\left\langle u^2\right\rangle_u = \frac{1}{\mathcal{N}}\int_0^\infty u^2 n(u)\,du = \frac{11}{27}u_c^2. \tag{2.157}$$

Note that $\langle\cdot\rangle_u$ indicates averaging over energy, rather than the ring circumference. It is still necessary to average $\mathcal{N}\left\langle u\right\rangle_u^2$ over the ring, yielding

$$G_E \equiv \left\langle \mathcal{N}\left\langle u^2\right\rangle_u \right\rangle = \frac{55}{24\sqrt{3}}\left\langle u_c P_\gamma\right\rangle. \tag{2.158}$$

Substituting the above into Eq. (2.153) and performing some algebraic manipulation yields

$$\sigma_\eta^2 = \frac{55}{32\sqrt{3}}\frac{\hbar}{mc}\frac{\gamma^2}{\mathcal{J}_s}\frac{\left\langle 1/\rho^3\right\rangle}{\left\langle 1/\rho^2\right\rangle}. \tag{2.159}$$

For an isomagnetic ring (ρ constant), we can further simplify to

$$\sigma_\eta = (0.62\times 10^{-6})\frac{\gamma}{\sqrt{\mathcal{J}_s\rho[m]}}. \tag{2.160}$$

Plugging in numbers for PETRA-IV [22] yields $\sigma_\eta \sim 0.4\times 10^{-3}$. Note that this is smaller than the actual anticipated value (0.7 to 0.9×10^{-3}) but in the correct ballpark.

We can follow the same line of argument to derive the equilibrium horizontal emittance

$$\varepsilon_{x,0} = \frac{1}{4}\tau_x G_x, \tag{2.161}$$

where $G_x \equiv \mathrm{d}\left\langle A_x^2\right\rangle/\mathrm{d}t$ is the average change in betatron amplitude. The calculation of G_x is more complicated than G_E and depends on the dispersion functions D and D'. This is because any spontaneous emission u results in an aforementioned change in betatron orbit $(\delta x_\beta, \delta x'_\beta)$. For more details, refer to [30]. We will quote the final result

$$\varepsilon_{x,0} = \frac{55}{32\sqrt{3}}\frac{\hbar}{mc}\frac{\gamma^2}{\mathcal{J}_x}\frac{\left\langle \mathcal{H}/|\rho|^3\right\rangle}{\left\langle 1/\rho^2\right\rangle}. \tag{2.162}$$

The $\mathcal{H}$-function is given by

$$\mathcal{H} = \frac{1}{\beta_x}\left(D^2 + (\beta_x D' - \frac{1}{2}\beta'_x D)^2\right). \tag{2.163}$$

The equilibrium horizontal emittance $\varepsilon_{x,0}$ is also known as the *natural emittance*. By minimizing dispersion and thus the average $\mathcal{H}$-function, modern storage rings are able to achieve extremely small values of natural emittance.

Finally, in the vertical direction, quantum excitation has a very small and negligible effect. Recall that the spontaneous emission has an opening angle $\sim 1/\gamma$. Thus the emission of a photon would deflect the electron transversely on the order of $\delta y' \sim 1/\gamma$. The resulting growth in betatron amplitude $\left\langle A_y^2 \right\rangle$ is proportional to $1/\gamma^2$, a very small number indeed. It can be shown that the equilibrium vertical emittance $\varepsilon_{y,0}$ is $1/\gamma^2$ times smaller than $\varepsilon_{x,0}$.

For most purposes, we will assume $\varepsilon_{y,0} \sim 0$. In actual operation, the beam is not permitted to damp vertically to $\varepsilon_{y,0}$. Any amount of intentional or unintentional transverse coupling will share the betatron orbit disruptions between the horizontal and vertical directions, causing the substantially larger $\varepsilon_{x,0}$ to dominate. Therefore in an actual machine, equilibrium vertical emittance effectively depends on $\varepsilon_{x,0}$ only. Let us define the coupling factor $k_c \equiv \varepsilon_y/\varepsilon_x$. Then at equilibrium,

$$\varepsilon_x = \frac{\varepsilon_{x,0}}{1+k_c}, \qquad \varepsilon_y = \frac{k_c \varepsilon_{x,0}}{1+k_c}. \tag{2.164}$$

Usually, we have $k_c \ll 1$. However in ultralow emittance rings, such as PETRA-IV, it can be advantageous to let $k_c \sim 0.1$ or higher to reduce intrabeam scattering and increase beam lifetime.

CHAPTER 3

TRANSVERSE GRADIENT UNDULATOR (TGU)

The concept of the transverse gradient undulator (TGU) was first introduced in the 1970s, not long after the advent of the free-electron laser [15]. Its original purpose was to combat the impact of electron energy spread on FEL gain in a storage ring, albeit at much lower electron energies. Since then, the field of accelerator-driven light sources has grown dramatically, most notably expanding into the X-ray regime. The TGU is once again being studied for its potential application to large energy spread electron sources, e.g. storage rings and plasma wakefield accelerators [33, 34].

In this chapter, we will study the physics of the TGU in the low-gain regime. We begin with the basic principles of the TGU and demonstrate how it modifies the FEL resonance condition, as well as define several important parameters and assumptions. Then, we dive into the derivation of the full 3D gain formula, starting from the gain convolution theorem Eq. (2.97). Finally, we end with discussion about the implications of the gain formula. At every stage, we will compare the results with that of the regular planar FEL, in order to highlight their differences and similarities.

3.1 Basic principles

Recall from Eq. (2.49) the FEL resonance condition, which we shall reproduce here for the fundamental harmonic $h = 1$:

$$\lambda_1 = \lambda_u \frac{1 + K^2/2}{2\gamma^2}. \tag{3.1}$$

To achieve FEL amplification, the frequency spread has to be narrower than the FEL gain bandwidth $1/N_u \sim 10^{-3}$ (see Eq. (2.93)). This is in turn determined by electron energy spread σ_η. Hence, for a fixed K and λ_u, we require $\sigma_\eta \ll 1/N_u$. However, from Eq. (2.160) we observe that the minimum energy spread feasibly achievable in a high-energy storage ring

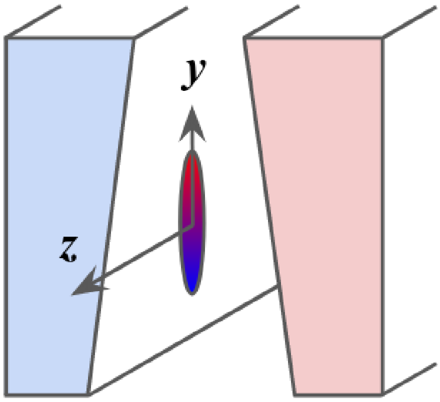

Figure 3.1: Cross-section of a transverse gradient undulator (TGU) aligned vertically. Direction of electron motion is in z. The magnetic field gradient grows stronger along the positive y-axis due to the canted undulator poles (exaggerated for visibility). If electron bunch (center oval) is dispersed appropriately so that higher energy electrons (red; top half) experience higher field strength while lower energy electrons (blue; bottom half) experience less, then FEL gain can be greatly improved even for large electron energy spreads.

is around 10^{-4}, with actual implementation coming closer to $\sigma_\eta \sim 10^{-3}$.

The energy spread requirement can be significantly relaxed if we are able to vary K in the numerator so as to cancel the spread in γ in the denominator. The TGU accomplishes this using a two-step method (Figure 3.1). First, by slightly canting the pole faces along the y-axis, the on-axis field strength becomes an approximately linear function of y:

$$K(y) \approx K_0(1 + \alpha y), \tag{3.2}$$

where α is the TGU gradient parameter. Notice that unlike the typically horizontally aligned planar undulator, we choose deliberately to align the TGU vertically due to the smaller vertical emittance in a storage ring (Eq. (2.164)). This reason will become clearer once we derive the TGU gain function.

Second, we deliberately introduce dispersion (Eq. (2.124)) in the vertical direction such that

$$y_j = D\eta_j + y_{\beta_j}, \tag{3.3}$$

where D is the dispersion parameter, η_j is the relative energy deviation, and y_{β_j} is the original betatron trajectory of the electron. For each electron j, we would like equation (3.1) to be individually satisfied:

$$\lambda_1 = \lambda_u \frac{1 + K_0^2(1 + \alpha y_j)^2/2}{2\gamma_0^2(1 + \eta_j)^2}. \tag{3.4}$$

Inserting equation (3.3) into the above yields

$$\lambda_1 \approx \lambda_u \frac{1 + K_0^2/2}{2\gamma_0^2} \left[1 + \frac{K_0^2 \alpha (D\eta_j + y_{\beta_j})}{1 + K_0^2/2} - 2\eta_j \right], \tag{3.5}$$

for $\eta_j \ll 1$ and $\alpha y_j \ll 1$. We can eliminate η_j and effectively remove the influence of energy spread by choosing

$$\alpha D = \frac{2 + K_0^2}{K_0^2}, \tag{3.6}$$

and assuming $y_{\beta_j} \ll D\eta_j$. The latter assumption implies that for the overall electron ensemble, the correlated electron beam size in y should be dominated by dispersion, i.e. $\langle y_{\beta_j}^2 \rangle \equiv \sigma_y^2 \ll D^2 \sigma_\eta^2$. We quantify this by introducing the dimensionless TGU parameter

$$\Gamma \equiv \frac{D\sigma_\eta}{\sigma_y}. \tag{3.7}$$

The previous argument is then equivalent to $\Gamma \gg 1$. For $\Gamma \sim 1$ or less, the TGU benefit is greatly diminished. We will see that Γ plays a pivotal role in TGU gain.

TGU-induced transverse focusing

The magnetic gradient in the TGU also excites additional transverse betatron oscillations [35]. The associated focusing strength can be shown to be

$$k_{\text{TGU}} = \frac{\sqrt{1+K_0^2/2}}{D\gamma}. \tag{3.8}$$

In the X-ray regime, this is typically very weak. To demonstrate, let us compare this with natural undulator focusing $k_{\text{nat}} = K_0 k_u/\sqrt{2}\gamma$ (Eq. (2.75)). The resulting ratio is

$$\frac{k_{\text{TGU}}}{k_{\text{nat}}} = \frac{\alpha}{k_u}\sqrt{\frac{K_0^2}{2+K_0^2}} \tag{3.9}$$

where we used the TGU resonance condition Eq. (3.6). For $K_0 \sim 1$, the ratio is of order $\alpha/k_u \sim 0.1$ in our parameter range. Since natural focusing is already considered negligible in the X-ray regime, we will also neglect TGU-induced focusing in the following discussion. This is especially important for a key assumption of the gain convolution formula (Eq. (2.79)).

3.2 Low gain perturbative analysis

The derivation of TGU gain formula follows closely the analysis in Section 2.2.3, with two key differences. Firstly, we make the substitution

$$y \to y - D\eta \tag{3.10}$$

in the particle position coordinate to account for the added TGU dispersion. Secondly, in accordance with Eq. (3.5), the TGU magnetic gradient modifies the FEL resonance condition:

$$\frac{k_u}{k_1} \approx \frac{1+K_0^2/2}{2\gamma_0^2}\left[1 + \frac{K_0^2\alpha y}{1+K_0^2/2} - 2\eta\right], \tag{3.11}$$

where k_u, k_1 are the wavenumbers of the undulator and the fundamental radiation harmonic respectively. This change is carried forward into the evolution equation of the FEL ponderomotive phase θ:

$$\frac{\mathrm{d}\theta}{\mathrm{d}z} = 2k_u\eta - k_u T_\alpha y - \frac{k_1}{2}\left(\vec{\boldsymbol{p}}^2 + k_\beta^2\vec{\boldsymbol{x}}^2\right), \tag{3.12}$$

where $T_\alpha \equiv K_0^2\alpha/(1+K_0^2/2)$ incorporates the TGU magnetic gradient, $(\vec{\boldsymbol{x}}, \vec{\boldsymbol{p}})$ are the particle position and momentum coordinates, and k_β represents the external focusing terms. Compared to Eq. (2.72), the first and third terms remain the same. Since we are ignoring TGU-induced transverse focusing effects, we leave the third term unchanged, as well as the evolution equations for $\vec{\boldsymbol{x}}$ and $\vec{\boldsymbol{p}}$ (Eq. (2.74)). For our purposes the TGU is only important for longitudinal FEL dynamics.

With all of that in mind, let us begin from the gain convolution result Eq. (2.97), restated here as

$$G = \frac{G_0}{8\pi N_u L_u^2\lambda_1^2}\int d\eta d\vec{\boldsymbol{x}} d\vec{\boldsymbol{y}} d\vec{\boldsymbol{\phi}} d\vec{\boldsymbol{p}}\, B_E(\vec{\boldsymbol{y}}, \vec{\boldsymbol{\phi}}) B_U(\eta, \vec{\boldsymbol{x}} - \vec{\boldsymbol{y}}, \vec{\boldsymbol{\phi}} - \vec{\boldsymbol{p}})\frac{\partial}{\partial\eta}F(\eta, \vec{\boldsymbol{x}}, \vec{\boldsymbol{p}}). \tag{3.13}$$

Here B_E is the seed radiation brightness, B_U is the brightness of the spontaneous radiation, F is phase space distribution of the initial electron beam, and L_u is the undulator length.

The prefactor G_0 is defined as

$$G_0 = (4\pi)^2\gamma_0\frac{I}{I_A}\frac{K_0^2[JJ]^2}{(1+K_0^2/2)^2}N_u^3\lambda_1^2, \tag{3.14}$$

where I is the electron peak current, $I_A = 4\pi\epsilon_0 mc^3/e \approx 17\,\mathrm{kA}$ is the Alfvén current with ϵ_0 being the vacuum permittivity, and the Bessel function factor $[JJ]$ is defined in Eq. (2.51). Let us reiterate that Eq. (3.13) is derived under the assumption that the electrons undergo no transverse focusing in the undulator, i.e. $k_\beta \to 0$. This includes natural undulator focusing, external focusing quadrupoles and TGU-induced focusing.

The spontaneous undulator brightness B_U can be obtained from the Wigner transform of the undulator radiation field $\mathcal{U}$. The latter is given by

$$\begin{aligned}\mathcal{U}(\eta, \vec{\boldsymbol{x}}(z), \vec{\boldsymbol{\phi}} - \vec{\boldsymbol{p}}; z) \;\; = & \;\; \int_{-L_u/2}^{L_u/2} dz \, \exp\Big[-ik\vec{\boldsymbol{\phi}} \cdot \vec{\boldsymbol{x}}(z) - ikz(\vec{\boldsymbol{\phi}} - \vec{\boldsymbol{p}})^2/2 \\ & + ik_u z(2\nu\eta - T_\alpha \vec{\boldsymbol{x}}(z) - \Delta\nu)\Big] . \qquad (3.15)\end{aligned}$$

Notice the similarity to Eq. (2.96). The only difference comes from the $T_\alpha \boldsymbol{x}(z)$ term. The electron trajectory is the same as that given in Eq. (2.79) and is restated here:

$$\vec{\boldsymbol{x}}(z) = \vec{\boldsymbol{x}} - \vec{\boldsymbol{p}}\,(L_u/2 - z) \tag{3.16}$$

Note that on right hand side $(\vec{\boldsymbol{x}}, \vec{\boldsymbol{p}})$ represent the transverse coordinates of the electron at the midpoint of the TGU, i.e. $z = L_u/2$. We choose to evaluate the gain integral at the midpoint because it is the location of the waists of the electron and X-ray beams.

From now on, we will restrict our discussion to the vertical TGU axis. The horizontal dimension can be easily obtained by setting $\Gamma \to 0$ or referring to Eq. (2.100). At the undulator midpoint, the brightness of the Gaussian seed X-ray pulse can be easily expressed as

$$B_E(y, \phi_y) = \frac{1}{2\pi\sigma_{ry}\sigma_{\phi y}} \exp\left(-\frac{y^2}{2\sigma_{ry}^2} - \frac{\phi_y^2}{2\sigma_{\phi y}^2} \right), \tag{3.17}$$

where $\sigma_{ry}, \sigma_{\phi y}$ are the RMS X-ray beam size and divergence measured at $z = L_u/2$. Similarly, we approximate the initial electron distribution as Gaussian:

$$F(\eta, y, p_y) = \frac{1}{(2\pi)^{3/2}\sigma_y\sigma_\eta\sigma_{py}} \exp\left[-\frac{(y - D\eta)^2}{2\sigma_y^2} - \frac{\eta^2}{2\sigma_\eta^2} - \frac{p^2}{2\sigma_{py}^2} \right]. \tag{3.18}$$

Here σ_η is the relative energy spread, and σ_y, σ_{py} are the electron beam size and divergence respectively. Notice the dispersion modification in the exponent.

Inserting Eqs. (3.17), (3.18), and the Wigner transform of Eq. (3.15) into the gain convolution formula (3.13) allows us to obtain an analytical formula for G. The calculation involves several steps of Gaussian integration, with more details in the Appendix. The final result is

$$
\begin{aligned}
G \;=\; \frac{G_0}{4\pi}\int_{-1/2}^{1/2} dz\,ds\,\frac{i(z-s)}{\sqrt{\mathfrak{D}_x\mathfrak{D}_y}}\exp\Bigg[&-2i\delta(z-s)-\frac{2\tilde{\sigma}_\eta^2(z-s)^2}{1+\Gamma^2} \\
&-\left(\frac{\Gamma}{1+\Gamma^2}\frac{\tilde{\sigma}_\eta}{\tilde{\beta}_y}\right)^2\frac{(z^2-s^2)^2}{2}\frac{\mathfrak{d}_y}{\mathfrak{D}_y}\Bigg]. \qquad (3.19)
\end{aligned}
$$

Following the convention established in Section 2.2.3, the gain formula is expressed in terms of the following dimensionless parameters

$$\delta = \pi N_u(\omega-\omega_1)/\omega_1, \qquad (3.20)$$

$$\tilde{\sigma}_\eta = 2\pi N_u\sigma_\eta, \qquad (3.21)$$

$$\tilde{\beta}_y = \beta_y/L_u. \qquad (3.22)$$

We also introduced the diffraction factors

$$\mathfrak{D}_{x,y} = \Sigma_{x,y}^2 + sz\,L_u^2\Sigma_{\phi x,y}^2 - iL_u(z-s)\left[\frac{1}{4k_1}+k_1\Sigma_{\phi x,y}^2\Sigma_{x,y}^2\right], \qquad (3.23)$$

$$\mathfrak{d}_y = \Sigma_y^2 + sz\,L_u^2\sigma_{\phi y}^2 - iL_u(z-s)\left[\frac{1}{4k_1}+k_1\sigma_{\phi y}^2\Sigma_y^2\right], \qquad (3.24)$$

with

$$\Sigma_y^2 = \sigma_y^2+\sigma_{ry}^2+D^2\sigma_\eta^2, \qquad (3.25)$$

$$\Sigma_x^2 = \sigma_x^2+\sigma_{rx}^2, \qquad (3.26)$$

$$\Sigma_{\phi x,y}^2 = \sigma_{px,y}^2+\sigma_{\phi x,y}^2. \qquad (3.27)$$

Here, $\sigma_{x,y}, \sigma_{px,py}$ are the electron beam sizes and divergences in x, y respectively, while $\sigma_{rx,ry}, \sigma_{\phi x,\phi y}$ are the analogous quantities for the seed X-ray beam.

In the limit $\Gamma \to 0$, the gain formula (3.19) reduces correctly to its counterpart for a traditional planar undulator. As in the planar undulator case, the factor $\mathfrak{D}_x\mathfrak{D}_y$ represents the dilution of gain due to 3D diffraction effects. In the exponential, the first term $-2i\delta(z-s)$ represents the effect of frequency detuning and similarly remains unchanged from its non-TGU counterpart.

The impact of the TGU is most evident in the second term $-2\tilde{\sigma}_\eta^2(z-s)^2/(1+\Gamma^2)$. Without the TGU ($\Gamma = 0$), this term results in the exponential suppression of gain due to energy spread. The TGU parameter Γ acts in the denominator to mitigate this effect. The third and final term in the exponential in Eq. (3.19) limits gain when a large electron divergence outweighs the required y-γ correlation for ideal TGU cancellation. This means that gain does not increases monotonically with Γ, but rather, reaches a maximum and then falls off.

While not appearing directly in the gain formula, the electron transverse emittances $\varepsilon_{x,y}$ play an important role due to their influence on $\sigma_{x,y}$ and $\sigma_{px,py}$ and thus the diffraction dilution factors $\mathfrak{D}_{x,y}$. In particular, having a small emittance ε_y along the TGU axis can potentially greatly increase gain. Herein lies the advantage of driving the TGU with a storage ring—due to the unique nature of radiation damping in a ring (see 2.3.2), the equilibrium natural emittance $\varepsilon_{x,0} \equiv \varepsilon_x + \varepsilon_y$ is a conserved quantity with the vertical emittance ε_y being typically orders of magnitude smaller than its horizontal counterpart. Moreover, by using coupling lattice elements such as skew quadrupoles, we can fine-tune this emittance ratio k_c (Eq. (2.164)). We will see in the TGU optimization section that by choosing $k_c \ll 1$, we can potentially increase gain by an order of magnitude. Even modest values of k_c, such as 1/6 used for PETRA-IV [22], present significant gain improvement (up to 2x).

CHAPTER 4

SIMULATION TECHNIQUES

In this study, we rely heavily on numerical simulation in order to model the performance of SRXFELO. It is therefore crucial to establish a proper background on common simulation techniques. The first three sections of this chapter discuss individually the three principle components of the the SRXFELO, namely the optical cavity, the FEL and the electron storage ring. Then, we round out the chapter by looking at a custom start-to-end simulation framework specifically developed for this study.

4.1 Optical cavity code

A complete representation of the radiation field is given by $E(\boldsymbol{x}, t; z)$, where $\boldsymbol{x} \equiv (x, y)$ are the transverse coordinates, t is the longitudinal coordinate (along the photon pulse), and z represents longitudinal position along the beamline. In code, the field is stored as a complex 3D array $\mathtt{E}(\mathtt{n_t}, \mathtt{n_y}, \mathtt{n_x})$ where each $\mathtt{n}$ is the index along the subscript coordinate. The longitudinal coordinate z is omitted for memory reasons. Instead, the field is edited in place as it propagates along the cavity.

The cavity code is developed based on the principles of Fourier optics. At various points in the cavity, it is required to perform the Fourier transform. Here, we make use of the well-established Fast Fourier Transform (FFT) algorithm, available in `python` under the package `numpy.fft`. The FFT can be performed along 1, 2 or all 3 coordinates (or axes) at one time,

$$\mathtt{E}(\mathtt{n_t}, \mathtt{n_y}, \mathtt{n_x}) \overset{\mathtt{FFT}}{\longleftrightarrow} \mathtt{E}(\mathtt{n}_\omega, \mathtt{n}_{\phi\mathtt{y}}, \mathtt{n}_{\phi\mathtt{x}}). \tag{4.1}$$

Here, angular frequency ω and transverse angles ϕ_y, ϕ_x are the Fourier companions to t, y, and x respectively. We are not free to choose the grid resolutions for ω, ϕ_y and ϕ_x (the "angular coordinates") independently of t, y and x (the "spatial coordinates"). Instead, they are constrained via the Fourier transform as follows. For the t-ω pair, the grid step sizes $\mathtt{dt}, \mathtt{d}\omega$ and maximum ranges $\mathtt{t_{max}}, \omega_{\mathtt{max}}$ are related by

$$\mathtt{dt} = \frac{2\pi}{\omega_{\mathtt{max}}}, \qquad \mathtt{d}\omega = \frac{2\pi}{\mathtt{t_{max}}}, \tag{4.2}$$

$$\mathtt{t_{max}} = \frac{2\pi}{\mathtt{d}\omega}, \qquad \omega_{\mathtt{max}} = \frac{2\pi}{\mathtt{dt}}. \tag{4.3}$$

These relationships are deliberately written in a circular fashion to emphasize the trade-offs faced by an user when choosing grid resolutions. A small step size $\mathtt{dt}$ results in a large frequency window $\omega_{\mathtt{max}}$, implying lower frequency resolution given a fixed number of grid points. If the user desires extra fine resolution in both t and ω, then the price must be paid in computational resources.

In the transverse domain, we have corresponding relationships for x-ϕ_x, namely

$$\mathtt{dx} = \frac{\lambda}{\phi_{\mathtt{x,max}}}, \qquad \mathtt{d}\phi_{\mathtt{x}} = \frac{\lambda}{\mathtt{x_{max}}}, \tag{4.4}$$

$$\mathtt{x_{max}} = \frac{\lambda}{\mathtt{d}\phi_{\mathtt{x}}}, \qquad \phi_{\mathtt{x,max}} = \frac{\lambda}{\mathtt{dx}}, \tag{4.5}$$

and similarly for y-ϕ_y. Here, physics constraints typically occur in the form of (a) minimum RMS beam size at the cavity waists, as well as (b) angular bandwidth of the Bragg reflectors.

For completeness sake, we will also define the total number of grid points (i.e. length of the array) as

$$\mathtt{N_t} \equiv \mathtt{t_{max}}/\mathtt{dt} + 1 \tag{4.6}$$

and so on for the other dimensions. (The additional 1 comes from including the end values of the simulation range.) In practice, since `N` needs to be an integer, one usually specifies `N` and along with either the simulation range or step size.

Having discussed the radiation field, we now turn our attention to the physics of the X-ray cavity. Figure 2.7 shows the layout of a generic 4-mirror X-ray cavity. As the radiation field traverses the cavity, it encounters (a) diffraction and focusing, (b) Bragg reflection, (c) possible optical imperfections, and finally (d) possible outcoupling. In the following subsections, we will discuss the modeling of each phenomena in turn.

Diffraction and Focusing

The subsequent discussion is based on the paraxial approximation established in Section 2.1.2. To recap, vacuum propagation of the radiation field is equivalent to multiplication by a complex phase factor in the angular domain (Eq. (2.18)). That is, given the angular representation of the radiation field $\mathcal{E}(\boldsymbol{\phi}, \omega; z_0)$ at some longitudinal position z_0, the field becomes

$$\mathcal{E}(\boldsymbol{\phi}, \omega; z_1) = \exp\left(-\frac{ik}{2}\boldsymbol{\phi}^2(z_1 - z_0)\right)\mathcal{E}(\boldsymbol{\phi}, \omega; z_0) \tag{4.7}$$

at the second position z_1. In code, this means that we (a) first perform FFT if the field array is not already in angular representation, then (b) multiply by the appropriate phase factor for each position $(\phi_{\mathtt{x}}, \phi_{\mathtt{y}})$ in the angular grid. The latter step is described by the pseudocode:

```
def diffraction( field, z :)
  for ny, phi_y in enumerate(phi_y_grid):
    for nx, phi_x in enumerate(phi_x_grid):
      prefactor = cexp( -I * k * z * (phi_x**2 + phi_y**2) / 2 )
      field[ny, nx] = field[ny, nx] * prefactor
```

(In a 3D beam, it is additionally necessary to repeat this for every time/frequency step.) In `python`, it is good practice to avoid `for` loops since they scale poorly in computation time. Instead, we recommend using vectorized operations (via `numpy.ndarray`).

Thin lens focusing in the paraxial regime involves a similar process as diffraction. Given the spatial representation of the radiation field $E_{\mathrm{bef}}(\boldsymbol{x}, t; z)$ immediately before the lens, the field after focusing becomes

$$E_{\text{aft}}(\boldsymbol{x},t;z) = \exp\left(-\frac{ik}{2}\left[x^2/f_x + y^2/f_y\right]\right) E_{\text{bef}}(\boldsymbol{x},t;z) \tag{4.8}$$

where f_x, f_y are the focal lengths in x and y respectively. In pseudocode:

```
def focusing( field, fx, fy ):
  for ny, y_pos in enumerate(y_grid):
    for nx, x_pos in enumerate(x_grid):
      prefactor = cexp( -I * k * (x_pos**2/fx + y_pos**2/fy) / 2 )
      field[ny, nx] = field[ny, nx] * prefactor
```

Once again, we can avoid unfavorable computation time increase in `python` by avoiding the `for` loop construction in favor of vectorized multiplication.

Let us demonstrate basic beam propagation within the 4-mirror cavity depicted in Figure 2.7. Let us designate the side lengths `L1`, `L2` as the waist-to-lens distance before and after the first lens. Both lenses are assumed to have the identical focal length `F` in both transverse directions. Beginning in the first waist, the cavity beamline looks like

```
diffraction( field, L1 )
FFT_to_spatial( field )
focusing( field, F, F )
FFT_to_angular( field )
diffraction( field, 2*L2 )
FFT_to_spatial( field )
focusing( field, F, F )
FFT_to_angular( field )
diffraction( field, L1 )
```

This assumes that the field starts in the angular representation. Notably missing from the model are the Bragg mirrors which not only reflects the beam, but also filters it in frequency and angle. We will discuss this next.

Reflection and Outcoupling

The most basic operation of a mirror is flipping the image about the reflection axis:

$$E(x, y, t; z) \longrightarrow E(-x, y, t; z) \tag{4.9}$$

$$\mathcal{E}(\phi_x, \phi_y, \omega; z) \longrightarrow \mathcal{E}(-\phi_x, \phi_y, \omega; z) \tag{4.10}$$

assuming that x is the reflection axis. In code, we reverse the order of the field array along the corresponding axis.

Bragg mirrors also have a bandwidth filtering effect in both angle and frequency domains. The Bragg reflectivity coefficient R can be calculated numerically given the reflection and crystal plane geometries, as well as material properties of the crystal. For modeling purposes, $R(\omega, \phi_x)$ can be considered a complex-valued function of frequency ω and angle ϕ_x along the reflection axis. The absolute magnitude $|R|^2$ gives the relative intensity of the reflected beam versus the incident. Figure 2.6 shows an example of R plotted versus frequency ω and angle ϕ_x. In the numerical model, R is represented as a 2D "mask" of complex values. The reflected field is obtained via

$$\mathcal{E}_{\text{refl}}(\phi_x, \phi_y, \omega; z) = R(\omega, -\phi_x)\mathcal{E}(-\phi_x, \phi_y, \omega; z). \tag{4.11}$$

The reflectivity array R must be provided with the same transverse resolution as the radiation field. We then multiply R onto $\mathcal{E}$ in the same fashion as the diffraction method, while also remembering to flip the array along the reflection axis.

The simplest method to outcouple the radiation beam from the cavity is to rely on mirror transmission. In a 4-mirror cavity, the first mirror (laying along the undulator axis) is thinner than the other three so as to allow for increased transmission. As before, we can define a transmission coefficient $T(\omega, \phi_x)$ for each of the mirrors. In order to obtain the transmitted field, we simply multiply the two:

$$\mathcal{E}_{\mathrm{trs}}(\phi_x, \phi_y, \omega; z) = T(\omega, \phi_x)\mathcal{E}(\phi_x, \phi_y, \omega; z). \tag{4.12}$$

Optical misalignment

By the translation property of the Fourier transform,

$$\mathcal{E}(\boldsymbol{\phi} + \Delta\boldsymbol{\phi}) = \mathcal{F}[\exp\left(ik\boldsymbol{x} \cdot \Delta\boldsymbol{\phi}\right) E(\boldsymbol{x})], \tag{4.13}$$

where $\mathcal{F}$ denotes the Fourier transform. We observe that a displacement of $\Delta\boldsymbol{\phi}$ in the angular domain corresponds to multiplication by a linear phase factor $\exp\left(ik\boldsymbol{x} \cdot \Delta\boldsymbol{\phi}\right)$ in the spatial domain. This is useful in modeling optical misalignments in the cavity.

Let there be a mirror misalignment of δ degrees clockwise relative to the vertical axis. By the law of reflection, the photon trajectory will be deflected by 2δ degrees from the nominal axis, i.e. $\mathcal{E}(\phi_x) \to \mathcal{E}_{\mathrm{err}}(\phi_x + 2\delta)$. By the translation property, we have

$$E_{\mathrm{err}}(x) = \exp\left(2ik\delta x\right) E(x) \tag{4.14}$$

where $E(x)$ is the field on the ideal trajectory without misalignment.

The translation property is useful not only for angular displacements, but also for the reverse — introducing a linear phase factor in angle will result in a corresponding translation in the spatial domain. We also use the same principle to simulate temporal delays (e.g. due to electron timing jitter) by including the phase factor in the frequency domain.

Note that when we displace the beam in this fashion, new information is not being "created" or "destroyed" at the window boundaries. Rather, due to the periodicity assumption of the Fourier transform, any field values being overwritten on one end of the array due to the translation simply wraps back around the other side. The operation conserves total energy, but care must be taken to avoid unphysical scenarios — especially if the field is not exponentially diminishing or periodic at the simulation boundaries. This usually does not pose a problem in our studies.

Phase front error

Phase front errors apply to the transverse profile of the beam and thus have a detrimental effect on transverse coherence. One physical source of phase error is surface roughness on the optical components. Another common source is mirror strain due to the mounting system and temperature fluctuations. These imperfections vary transversely across the face of the mirror/lens, and manifest as a phase error term $\varphi(\boldsymbol{x})$ where

$$E_{\mathrm{err}}(\boldsymbol{x}) = \exp\left(i\varphi(\boldsymbol{x})\right) E(\boldsymbol{x}). \tag{4.15}$$

Phase error is typically quoted either as a fraction of the fundamental wavelength, e.g. $\varphi_{\mathrm{rms}} = \lambda/30$, or in units of distance $\Delta h \equiv \varphi/k$, e.g. $\Delta h_{\mathrm{rms}} = 0.2\,\text{Å}$. The latter notation tends to be used in discussing surface roughness, although appropriate factors have to be included to account for the reflection geometry.

There are three main sources of phase error data in our studies. See Figure 4.1 for examples of each. The first method is rocking curve imaging (RCI). Here, the Bragg crystal is "rocked" from side-to-side relative to an incident test beam, effectively scanning its reflectivity as a function of angle along the reflection axis. The crystal is then displaced slightly in the orthogonal direction, and the scanning is repeated. Thus, phase error information derived from RCI is effectively 1D — without an appropriate way to calibrate adjacent scans in

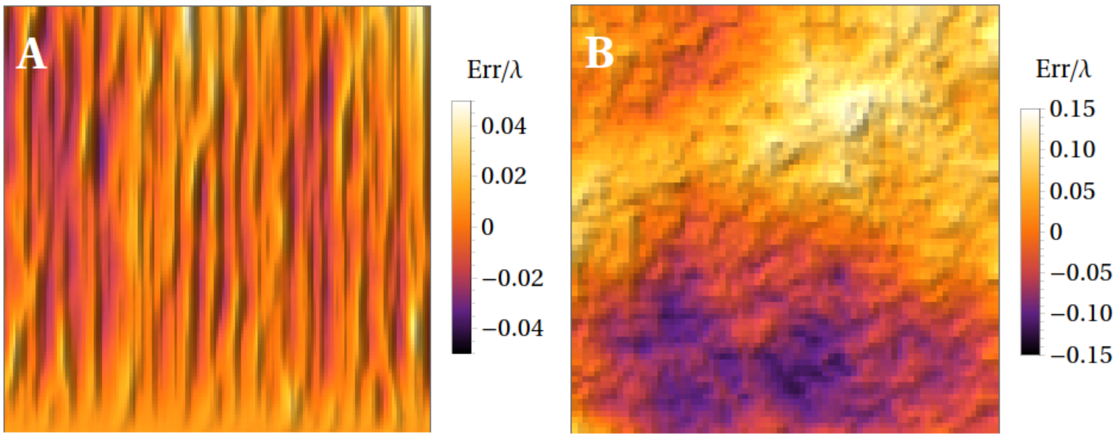

Figure 4.1: 2D amplitudes of crystal phase error from (A) rocking-curve imaging and (B) synthetic generation. Error amplitude is expressed as a fraction of the fundamental wavelength λ. Notice the vertical striation in the RCI data resulting from the single dimension scan.

phase, we can only do crude adjustments such as aligning the sample means or start/end points. Nevertheless, these RCI scans contain valuable noise spectrum information on the phase error. In a pinch, we can also use the RCI dataset to simulate beam distortion in 1D (as long as there is no x-y correlation in the optical lattice).

Using the noise spectra from RCI measurement, we can artificially generate a phase error map in 2D. This is the second source of phase error data. Advantages of this method include being able to enforce desired statistical properties (such as RMS or min-max values), and the easy availability of data.

Finally, the speckle method provides full 2D phase error measurement up to a resolution of $\sim \lambda/100$. We refer the reader to [36] for details of the speckle measurement technique. It is the most accurate of the three methods, and is the primary source of experimental phase error data.

Summary

The cavity code relies on the principles of Fourier optics. Every physical operation on the field can be thought of as the multiplication of an appropriate phase factor in the correct Fourier

Operation	Domain	Key parameter	Phase factor
Diffraction (drift)	Angular	Distance s	$\exp\big(-ik\boldsymbol{\phi}^2 s/2\big)$
Focusing (lens)	Spatial	Focal length f	$\exp\big(-ik\boldsymbol{x}^2/(2f)\big)$
Bragg reflection	Angular	Reflectivity $R(\omega, \phi_x)$	$R(\omega, -\phi_x)$
Outcoupling	Angular	Transmission $T(\omega, \phi_x)$	$T(\omega, \phi_x)$
Mirror misalignment	Spatial	Misalignment $\Delta\phi$	$\exp(2ikx\Delta\phi)$
Spatial displacement	Angular	Displacement Δx	$\exp(2ik\phi\Delta x)$
Phase front error	Spatial	Error profile $\varphi(x,y)$	$\exp(i\varphi(x,y))$

Table 4.1: Summary table of phase operations in Fourier optics. Domain indicates the appropriate Fourier representation for the field.

space. Table 4.1 summarizes all the operations discussed previously. A cavity beamline can then be thought of as a sequence of these operations set up in a loop. See Figure 4.2 for a flowchart representing the 4-mirror bowtie cavity.

4.2 FEL codes

In this study, we use `GENESIS` [37] and `ginger` [38], two popular FEL codes within the accelerator community. These codes rely on a common set of simulation principles, which we shall briefly introduce below. Additionally, we will also outline the steps taken to modify version 2 of `GENESIS` to include TGU physics[1].

Longitudinal model

In the longitudinal direction, the electron and radiation beams are divided into "slices". For the radiation beam, this is no different than discretizing the t dimension. For the electron beam however, each slice contains its own microcosm of particles which do not interact directly with any other electron slice. Each electron slice is considered adjacent to

---

[1] The newest version of `GENESIS` (version 4) as of time of writing has added TGU functionality, rendering the modification unnecessary. It works based on largely the same principles as that described in the main text.

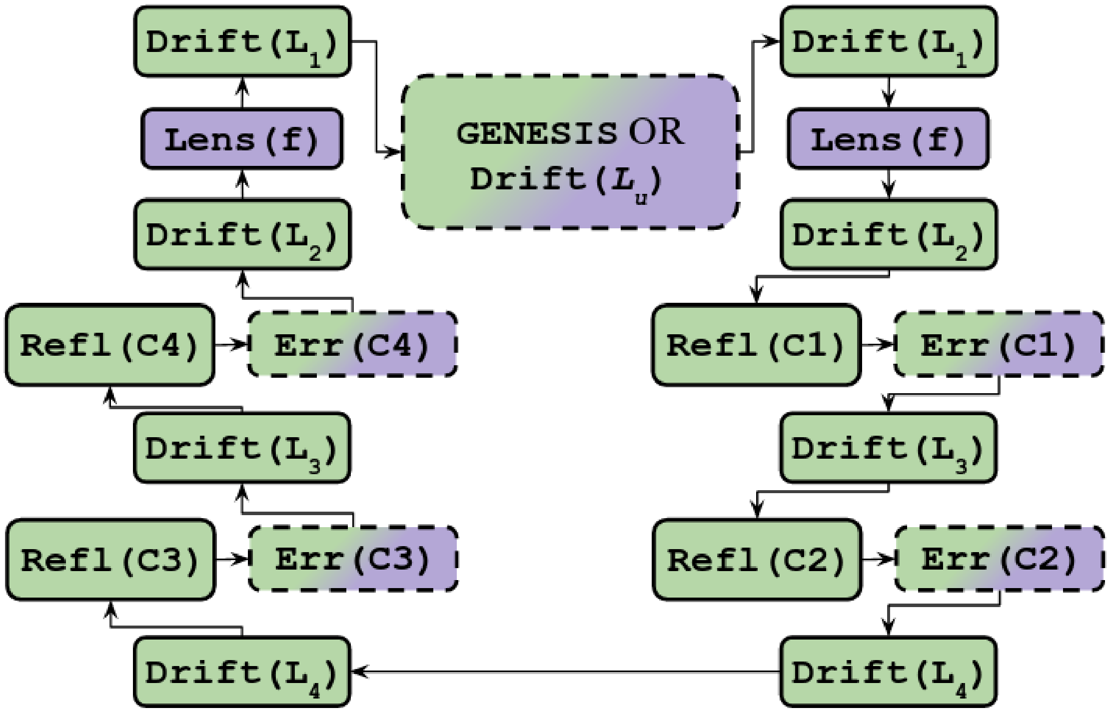

Figure 4.2: Flowchart depicting the simulation process for a four-mirror cavity. The color of each box represents approriate Fourier domain: spatial (purple) or angular (green). Dashed outline represents optional step. The `Err` operation may include misalignments and/or phase errors. Each round trip begins and ends at the undulator, with optional `GENESIS` simulaton or drift operation to bridge the gap to the next iteration.

a corresponding radiation slice, as they would be in a physical FEL.

After an amount of time, the radiation field is expected to slip ahead of the electron beam longitudinally. The total slippage distance across the entire undulator is given by

$$z_{\text{slip}} = N_u \lambda_1. \tag{4.16}$$

The slippage process accounts for the development of longitudinal coherence. Therefore, it is crucial (especially for high-gain cases) that the slice width Δt is much smaller than z_{slip}/c. This allows for the appropriate discretization of the slippage process.

Transverse model

Within each longtudinal slice, there are different approaches to modeling the transverse physics. `GENESIS`, a full 3D code, takes a particle-in-cell (PIC) approach. Each particle is represented by its 6D coordinates and exist within the 2D rectangular grid of the radiation field. The motion of the particles are tracked according to the FEL equations (Section 2.2.2), with field terms being interpolated at the location of each particle. Similarly, the radiation field evolves according to Eq. (2.77) with each electron being treated as point particle.

Numerical integration of transverse particle motion is handled by solving the transverse Hamiltonian, whereas longitudinal motion is integrated using the 4th order Runge-Kutta method. The evolution of the radiation field uses the finite difference alternating-direction implicit (ADI) method. The ADI method is particularly fast and stable given the parabolic form of the wave equation Eq. (2.77).

The code `ginger` takes a 2.5D pseudo-spectral approach. The transverse field is decomposed into axisymmetric TEM modes, truncated to a finite order. Thus the field is effectively stored as eigenmode coefficients. The evolution of these eigenmodes are calculated beforehand by solving the homogeneous form of the wave equation Eq. (2.77), followed by projecting the source term (electrons) onto these eigenmodes. In this manner, the continuous PDE problem is recast as a linear algebra problem.

The pseudo-spectral approach takes advantage of the fact that the transverse FEL mode is typically highly symmetric (usually Gaussian). Very few eigenmodes are necessary to adequately describe the field, therefore greatly reducing computational overhead. Furthermore, since the eigenmodes are continuous functions, the field itself can be represented continuously and is not subjected to the usual drawbacks of discretization (e.g. aliasing).

However, the pseudo-spectral method can struggle if the field is not particularly symmetric. For instance, the radiation field is dominated by asymmetric spontaneous emission during the FEL start up phase. One must either greatly increase number of eigenmodes in the simulation, thereby eroding the aforementioned computational gains, or risk not accurately representing the radiation field. In particular, 2.5D codes like `ginger` use only azimuthally symmetric modes and generate a well-known discrepancy versus `GENESIS` during the initial start-up phase [39]. This becomes less of a problem once the FEL amplification process takes hold and the Gaussian mode becomes dominant.

Finally, an honorable mention must be given to the 1D model. In this case, the field is reduced to a single point and the electrons are represented only by their longitudinal coordinates (γ, θ). The 1D model can be considered as a limit of the 3D finite difference model as $N_x, N_y \to 1$. Its main advantages include algorithmic simplicity and computational speed. For this reason, it is a useful tool for ballpark calculations and benchmarking purposes, prior to setting up a full 3D run.

TGU modification

By default, version 2 of `GENESIS` used in this study does not include a transverse linear term in the undulator field. As previously discussed in Eq. (3.2), the canted polefaces of the TGU introduces a transverse linear dependance in undulator strength

$$a_w(x) = a_{w,0}(1 + \alpha x) \tag{4.17}$$

where we assume x is the TGU axis. We use $a_w \equiv K/\sqrt{2}$ here to denote undulator strength in accordance with the notation used in `GENESIS`. The corresponding modification must be made to the `faw2` function in the `magfield.f` source file. More specifically,

```
faw2 = awz(i)*awz(i)*(1.d0
          + 2.d0*atgu*xt + atgu*atgu*xt*xt
          + xkx*xt*xt + xky*yt*yt )
```

The middle line of code is our addition. We introduced the variable `atgu` defined by α/k_u.

(The factor of $1/k_u$ comes from `GENESIS` coordinate normalization.) Notice that the TGU parameter multiples into the horizontal coordinate `xt`, contrary to our desired orientation. This is because of the implicit assumption in `GENESIS` that the undulator is horizontally oriented. It is therefore also necessary to rotate the electron bunch externally before and after each `GENESIS` run.

Another external operation applied to the electron bunch before/after `GENESIS` is the addition and removal of dispersion. Using Eq. (3.6), we can calculate the requisite amount of dispersion to introduce to the electron bunch beam via an external script.

4.3 Storage ring code

To model the storage ring, we used the popular particle tracking code `elegant` developed by M. Borland [40]. The code `elegant` tracks each particle in 6-dimensional phase space $(x, x', y, y', s, \delta)$, where (x, y) represent the transverse particle positions, (x', y') the transverse particle momenta, and (s, δ) the longitudinal particle distance and momentum deviation respectively. The storage ring is described via an input description file ("lattice file") that breaks down the machine into distinct, specialized elements.

The exact composition of the lattice file is determined by the breadth and depth of the simulation. Our model of the ring is composed of three main elements: (a) one-turn periodic transport (`ILMATRIX` element), (b) synchrotron radiation (`SREFFECTS`), and (c) RF acceleration (`RFCA` element). We will give a brief description of each below.

The `ILMATRIX` element stands for Individualized Linear Matrix for fast symplectic tracking. It is based on the transport matrix representation previously discussed in Section 2.3.1. To summarize, for a given phase plane such as x-x', we can write the generic one-turn transport matrix as

$$M_x = \begin{pmatrix} \cos 2\pi\nu_x + \alpha_x \sin 2\pi\nu_x & \beta_x \sin 2\pi\nu_x \\ -\gamma_x \sin 2\pi\nu_x & \cos 2\pi\nu_x - \alpha_x \sin 2\pi\nu_x \end{pmatrix} \tag{4.18}$$

where $\alpha_x, \beta_x, \gamma_x$ are the Twiss parameters and ν_x is the tune. Similar matrices M_y, M_s exist for the y-y' and s-δ planes. These set of three matrices, along with the appropriate cross-terms (dispersion, momentum compaction, transverse coupling), dictate the nominal trajectory of the particle orbit.

For any given particle, the individualized matrix is calculated from M by performing a Taylor expansion on the tune ν. In general, the tune of each particle is dependent on its momentum offset δ and betatron amplitude A. The sensitivity of this dependence is specified by the user via the magnitude of the partials $\partial\nu/\partial\delta$, $\partial\nu/\partial A$. Finally, the individualized matrix is multiplied into the particle coordinates, after accounting for the momentum-dependent closed orbit.

The `SREFFECTS` element takes a "lump sum" approach to tracking the synchrotron damping within the ring. Instead of modeling each radiative element, the bunch is damped according to the user-specified damping parameters, such as the partition numbers $\mathcal{J}_x, \mathcal{J}_y, \mathcal{J}_s$, the damping times τ_x, τ_y, τ_s, as well as equilibrium energy spread σ_η and natural emittance $\varepsilon_{x,0}$. The `SREFFECTS` element then models exponential damping based on these parameters. See Section 2.3.2 for specific discussion of the damping dynamics.

The net energy loss through synchrotron radiation is topped up each turn via the `RFCA` element, which models the RF acceleration system to the first order. Key parameters include the peak voltage, cavity frequency, and the acceleration phase.

Particle file compatibility with `GENESIS`

Although both `elegant` and `GENESIS` rely on 6D particle tracking, the discrete slice representation of the particle bunch in `GENESIS` makes it difficult for seamless compatibility with `elegant`. There are two main challenges.

First, the longitudinal particle coordinates used in `GENESIS` are (θ, γ), i.e. FEL ponderomotive phase and particle energy respectively, in comparison to (s, δ) in `elegant`. While it would be relatively straightfoward to translate between $\gamma \leftrightarrow \delta$, the longitudinal coordinate is less clear. The phase θ is measured with respect to the particular slice resided by the particle, while s is calculated relative to the nominal path taken by the reference particle. One can in theory approximate s based on θ and the relative position of the slice within the bunch, but it is unclear how to account for the periodic boundary conditions imposed by the FEL slice without significantly altering the FEL code.

The second problem is the relative size of the longitudinal simulation windows within `elegant` and `GENESIS`. In `elegant`, there is no explicit simulation window width per se—instead the rough size of the "window" is simply set by several multiples of the specified RMS bunch length σ_z. In `GENESIS`, due to the coexistence of the discretized radiation field, it is necessary to explicitly define the simulation window width t_{width}. Comparing the two values, it is often the case that the full bunch length $\sim 6\sigma_z$ in `elegant` is substantially larger than a feasible t_{width} for fast simulation. Put in a different way, the necessary longitudinal resolution Δt, set by the slippage length and frequency window, is far too small compared to the $6\sigma_z$ window—which comes at a significant cost to computation time.

We use a different approach to resolve the particle file compatibility issue. Instead of exchanging the particle file between the two programs directly, we exchange the first- and second-order moments of the bunch (i.e. mean and standard deviations). After each `GENESIS` run, we measure and record the beam moments of the electron bunch. Then, we input these parameters into the `bunched_beam` method in `elegant`. This method generates a random

Gaussian beam with the specified moments for subsequent tracking. After one iteration of `elegant`, the resulting beam moments are recorded again, and a corresponding `GENESIS` particle file is generated via Gaussian sampling for the next step.

There are two additional benefits to the moment-tracking method. First, it allows for easy concurrent tracking of multiple electron bunches. In most of our studies, there are multiple electron bunches within the ring interacting sequentially with one single X-ray pulse. In lieu of storing and manipulating multiple particle files, we simply store the beams moments in an array and update/retrieve the appropriate row during each iteration. The second benefit is the possibility to run `GENESIS` in single-slice mode. Single-slice simulation is much faster than running with full time-dependence and is often used in initial exploration studies. Clearly, with the lack of a full longitudinal dimension, single-slice mode is incompatible with `elegant`. However, by simply exchanging tranverse beam moments and establishing a realistic bunch length within `elegant`, one can side-step this limitation.

4.4 Start-to-end framework

With all the critical components of the simulation framework explored in the preceding sections, we now turn our attention to the overall simulation pipeline (Fig. 4.3). The simulation pipeline can be broken down into four parts, namely (a) overall run management, (b) TGU-FEL simulation, (c) storage ring propagation, and (d) X-ray cavity propagation. Components (b), (c) and (d) are implemented as described in their respective sections.

Run management is handled by a wrapper program. The user first provides a parameter input file, similar to that of `GENESIS` or `elegant`. Then, the user sets up a tracking routine using functions provided in the run manager library. There are several tracking options available, including (a) photon-only cavity propagation, (b) single-pass `GENESIS` run for gain calculation, and (c) full multipass SRXFELO simulation with both `GENESIS` and `elegant`.

In photon-only cavity propagation, the run manager calls upon the cavity code `pyopt`

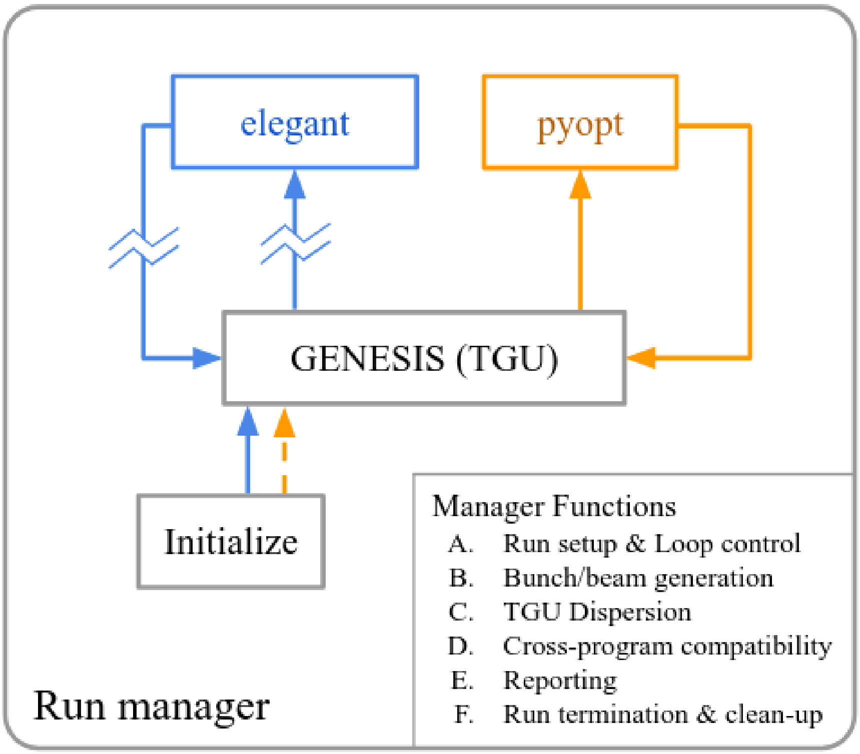

Figure 4.3: Flowchart of start-to-end simulation framework. Blue lines indicate electron simulation pathway, while orange lines indicate X-ray pathway. Dashed line indicates optional step. The run manager serves as a wrapper program that coordinates the tracking run. FEL simulation is handled by modified `GENESIS` version 2, while storage ring particle tracking is handled by `elegant`. Broken lines between `GENESIS` and `elegant` indicate that the electron file is not preserved between iterations. X-ray cavity simulation is handled by an in-house Fourier optics code `pyopt`. The X-ray file is preserved throughout.

to propagate the field file through a user-specified cavity. Both the run manager and `pyopt` come with custom reporting capabilities, including spatial and angular beam moments, 2D beam spot, and frequency spectrum. In the single-pass `GENESIS` use case, the run manager generates an initial electron particle file and optionally a photon field file (for seeded start). Then, it calls upon `GENESIS` to perform the FEL simulation, and reports on the results afterwards. In the TGU-FEL case, the run manager also performs two important calculations pre- and post-run, namely introducing the correct TGU dispersion to the particle file, and rotating the particle and field files for compatibility with `GENESIS`.

The multipass tracking mode is the most complicated and comprehensive use case. It makes use of all of the aforementioned functionality. Starting with the appropriate particle/field files, the run manager iteratively (a) calls `GENESIS` to handle the TGU-FEL simulation step, and (b) calls `elegant` and `pyopt` to handle the storage ring orbit and cavity propagation steps respectively. In between steps (a) and (b) are various pre- and post-processing calculations to ensure compatibility and enable statistics tracking. This includes particle/field manipulation (e.g. dispersion, rotation), particle file re-generation (for compatibility between `elegant` and `GENESIS`), and multi-bunch statistics tracking.

While the aforementioned simulation cases are the most commonly used, the object-oriented nature of run manager library provides plenty of flexibility for the user to define their own tracking mode. Furthermore, it is relatively easy to extend or modify the physics model to accomodate future studies. For instance, should a detailed study of a specific cavity outcoupling method be desired, one can readily modify `pyopt` to do so. The inclusion of optical phase front errors and misalignments is an example of this extension.

CHAPTER 5

DESIGN STUDY OF A STORAGE RING XFELO

The design of a storage ring XFELO (Fig. 1.2) can be understood to be made up of three separate systems: (a) the electron storage ring, (b) the TGU, and (c) the optical cavity. In the preceding chapters, we examined the core physics of each of the three components independently. Now, we will put it all together in order to study the design, performance, and implementation challenges of the storage ring XFELO.

We will begin by discussing some of the choices made in choosing the parameters for the study. Much attention has been paid in particular to the TGU parameter optimization process. Following that, we will examine the projected performance of the chosen parameter set, obtained using the simulation framework detailed in the previous chapter. Finally, we will end the chapter with some discussion on ring-FEL coupling strategies for the XFELO.

5.1 Design parameters

Storage ring and optical cavity

The storage ring parameters chosen for this study are based on the PETRA-IV electron synchrotron located in Hamburg, Germany [22]. Refer to Table 5.1. PETRA-IV is an upgrade of the existing ring PETRA-III, which brings the light source into the 4th generation. Its target to provide ultralow electron emittance makes it a prime candidate to be the storage ring driver for the XFELO. While existing PETRA-IV plans do not include an XFELO, we nevertheless feel that it would serve as an instructive starting point for the growing number of 4th generation storage rings coming online in the near future.

That being said, we do make slight adjustments to the parameters in order to favor XFELO performance. Most notably, the emittance coupling factor has been reduced to 1/6, and the peak current of the electron bunch has been increased from 10 A to 33 A with

Parameter	Symbol [unit]	Value
Electron energy	E_{beam}	5.96 GeV
Storage ring circumference	L_{ring}	2333.87 m
Relativistic gamma	γ_r	1.167×10^4
Bunch charge (lasing)	Q_b	4 nC
Bunch charge (non-lasing)		1 nC
Number of lasing bunches		16
Peak current (lasing)	I_{pk}	31.89 A
Relative energy spread	σ_η	0.1%
Natural emittance	$\varepsilon_{x,0}$	19 pm rad
Emittance ratio	k_c	0.167
Emittance damping time (y)	τ_y	22 ms
Betatron functions at TGU midpoint	β_x, β_y	8.2 m, 4.5 m

Table 5.1: Table of storage ring parameters used for the SRXFELO design study. These values are largely based on PETRA-IV [22].

a corresponding cost to bunch length. Both of these choices are theoretically achievable by PETRA-IV and will effectively increase TGU gain. In an actual implementation, we envision various operating modes for the storage ring, one of which would be the "XFELO mode" specially tuned for the FEL in question.

The X-ray cavity is based on the 4-mirror bowtie design, previously discussed in Section 2.2.4. Refer to Figure 5.1 and Table 5.2 for the design layout and parameters. Based on the target 14.4 keV photon energy and using the C337 crystal configuration, the nominal angle of incidence on each mirror is calculated to be $\theta_{\text{inc}} = 9.2477\,\text{deg}$. The cavity dimensions are then designed around θ_{inc}, a TGU undulator measuring $L_u = 30\,\text{m}$, and a feasible footprint for the storage ring facility. The final cavity has a footprint of 70 m by 11.87 m, with a round trip distance of $L_{\text{cav}} = 145.87\,\text{m}$ ($T_{\text{cav}} = 486.56\,\text{ns}$). Note that we specifically chose $L_{\text{cav}} = L_{\text{ring}}/16$ to have a whole number divisor with the storage ring circumference L_{ring}. We should also like to note that this cavity design is just one of many possible configurations, and the ideal cavity layout should be determined on a case-by-case basis for each facility.

Parameter	Symbol	Value
Photon energy	$\hbar\omega_1$	14.4125 keV
Angle of reflection	θ_{inc}	9.2477 deg
Round trip length	L_{cav}	145.867 m
Round trip time	T_{cav}	486.560 ns
Length 1	L_1	12 m
Length 2	L_2	8 m
Length 3	L_3	37.433 m
Length 4	L_4	0.5 m
Cavity length (footprint)	D	70 m
Cavity width (footprint)	W	11.87 m
Focal length	f	20.70 m
Rayleigh lengths at W1	$Z_{Rx1,Ry1}$	8.2 m
Rayleigh lengths at W2	$Z_{Rx2,Ry2}$	32.82 m

Table 5.2: Table of cavity parameters used for the SRXFELO design study. Refer to Figure 5.1 for physical layout.

In addition to cavity dimensions, we also need to determine focal lengths and Rayleigh distances of the stable Gaussian mode. The latter is primarily chosen based on TGU optimization (discussed in the next section). Near optimal TGU performance was achieved with a round beam mode of $Z_{Rx1} = Z_{Ry1} = 8.2\,\mathrm{m}$. Having equal Rayleigh lengths in both dimensions means that the focal length f is also the same in both directions. Using Eq. (2.116), we calculated that $f = 20.70\,\mathrm{m}$ and at waist 2 (outside of the undulator) we find $Z_{Rx2} = Z_{Ry2} = 32.82\,\mathrm{m}$. The choice of f falls within values achievable by off-the-shelf beryllium compound refractive lenses (CRLs).

Finally, the four mirrors are diamond Bragg crystals in the C337 configuration. The first crystal C1, located after the TGU, is thinner at 88 microns for outcoupling. The three other crystals have thicknesses of 1000 microns. The net round trip power loss without additional errors is $\sim 15\%$.

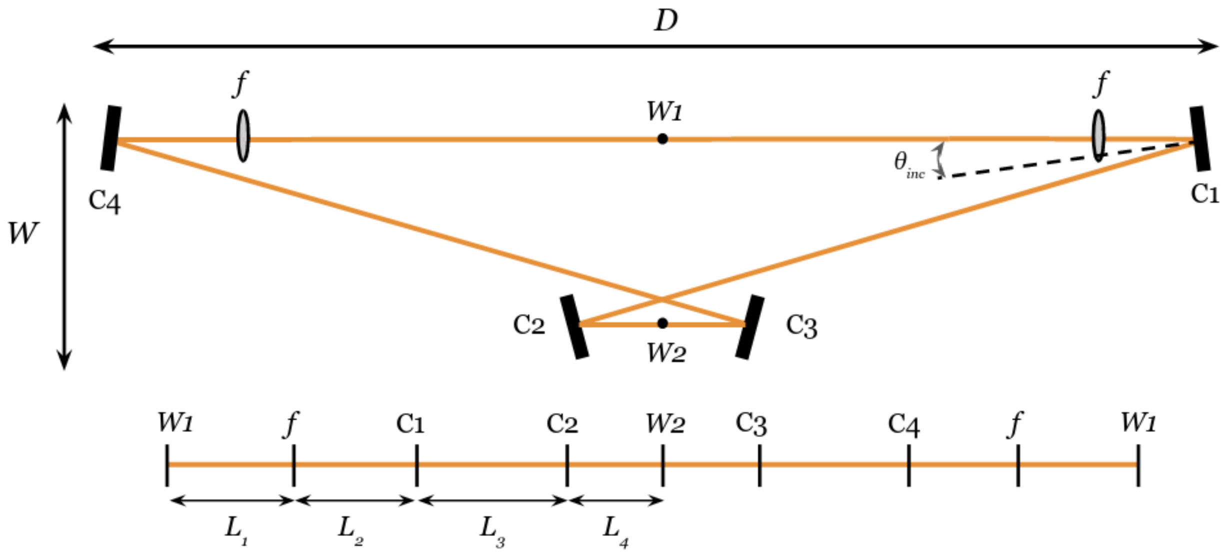

Figure 5.1: Schematic of the 4-mirror bowtie cavity used for the SRXFELO design study. Dimensions and parameters are listed in Table 5.2.

TGU parameter optimization

We wish to determine the optimal set of beam parameters (for both electron and photon) that would maximize TGU gain. In this sense, the TGU gain equation Eq. (3.19) can be regarded as an optimization problem. Let us work with the following nine degrees of freedom: electron betatron functions (2), X-ray Rayleigh lengths (2), electron transverse emittances (2), energy spread (1), FEL frequency detuning (1), and TGU parameter (1). The remaining parameters are considered fixed *a priori* and are drawn from Table 5.1.

We tested a number of different optimization algorithms on this problem, including gradient descent, simulated annealing and simple hill climber. We found that the objective function, i.e. the gain integral, had in all cases a clear global optimum and a simple convex shape. Provided reasonable starting parameters, all algorithms were able to converge relatively quickly (on the order of minutes) and reliably. In the end, we chose the simple hill climber method for its algorithmic simplicity.

The first parameter of interest is the TGU parameter Γ. Figure 5.2 shows TGU gain as a function of Γ, with the optimum value at $\Gamma_{\text{opt}} = 13.3$ and max gain $G_{\text{th}} = 0.42$ from

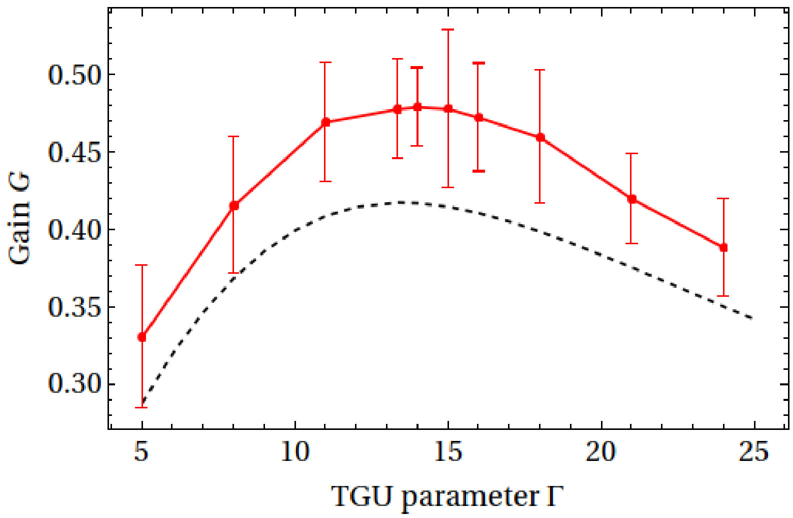

Figure 5.2: Plot of gain G versus TGU parameter Γ depicting results from numerical integration (black, dashed) and time-independent `GENESIS` simulation (red, solid). Error bars indicate 2 standard deviations of the shot-to-shot variation. Simulation results consistently overperform when compared to theory, likely due to the magnitude of gain $G \sim \mathcal{O}(1)$ surpassing the low-gain assumption of the analytical formula. Nevertheless, both models are consistent on the location of the gain optimum at $\Gamma = 13.3$.

numerical integration and $G_{\text{sim}} = 0.48$ from `GENESIS` simulation. The systematic overshoot from `GENESIS` simulation is a result of the magnitude of gain $G \sim \mathcal{O}(1)$ exceeding the low-gain assumption used to derive Eq. (3.19). In such cases, nonlinear interaction terms further boost its value in such a way that the gain increase $\propto G_{\text{th}}^2$ for $G < 1$. Nevertheless, the primary quantity of interest Γ_{opt} remains consistent between simulation and theory. The shape of the curve is also consistent with our qualitative analysis of the TGU gain formula. There is a dramatic rise in gain at low Γ as the TGU kicks in, followed by gradual drop-off at values above Γ_{opt} due to diffraction effects.

We can convert Γ_{opt} into the more practical values of dispersion D and magnetic gradient α using Eqs. (3.6) and (3.7). Figure 5.3 shows the optimization plots of these two parameters, with $D_{\text{opt}} = 6.2\,\text{cm}$ and $\alpha_{\text{opt}} = 0.045\,\text{mm}^{-1}$. The maxima are rather broad, affording flexibility to account for experimental limitations and/or imperfections. For example, if we nominally define an "acceptable" gain value as falling within 10% of the maximum, the

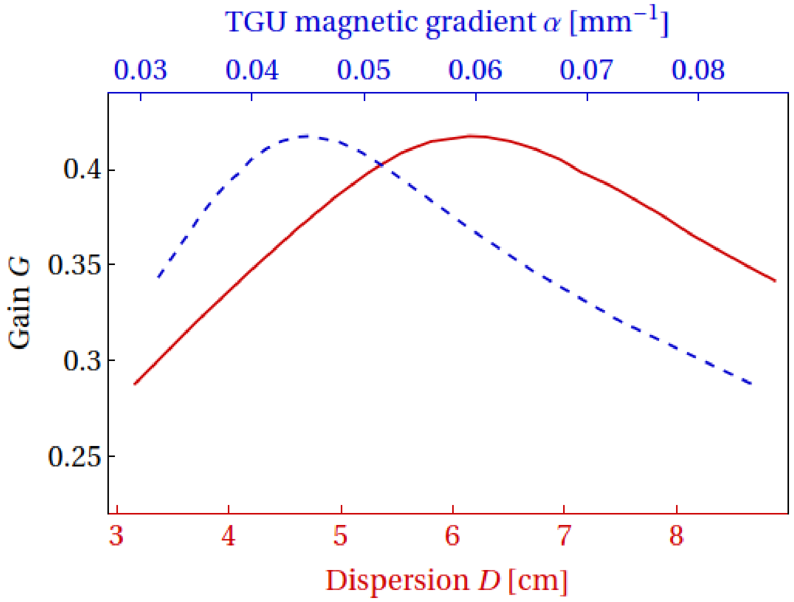

Figure 5.3: Plot of gain G versus electron beam dispersion D (red, solid) and TGU magnetic gradient α (blue, dashed) derived from numerical integration of the 3D gain formula. These parameters are derived from the TGU parameter Γ by Eqs. (3.6) and (3.7). Optimal gain is attained at $D_{\text{opt}} = 6.2\,\text{cm}$ and $\alpha_{\text{opt}} = 0.045\,\text{mm}^{-1}$ for the chosen machine parameters.

allowable ranges of D varies between 5 - 7.5 cm and α between 0.035 - 0.055 mm^{-1}.

Note that although the optimal gradient $\alpha_{\text{opt}} = 0.045\,\text{mm}^{-1}$ may be considered large from an engineering standpoint, it still lays within the realm where the linear theory is appropriate. From the discussion around Eq. (3.5), we require that $\alpha y_j \ll 1$ for each individual electron, which in the ensemble sense translates to $\alpha\sigma_y \ll 1$, where σ_y is the RMS electron beam size in y. This is amply satisfied in our case.

Next, we explore the effect of transverse emittances on TGU gain (Fig. 5.4). In a storage ring, the natural emittance $\varepsilon_{x,0}$ is determined by the magnetic lattice and radiation damping, with the individual emittances $\varepsilon_x, \varepsilon_y$ being set by tuning k_c. We observe that TGU gain always increases as $\varepsilon_{x,0}$ is reduced, with the lower bound ultimately set by storage ring constraints. This is because lower $\varepsilon_{x,0}$ is associated with smaller RMS beam sizes, which in turn reduces the magnitude of the diffraction factors $\mathfrak{D}_x, \mathfrak{D}_y$ in the denominator of Eq. (3.19).

Perhaps more notably, we observe greater benefit to TGU gain in minimizing ε_y over ε_x.

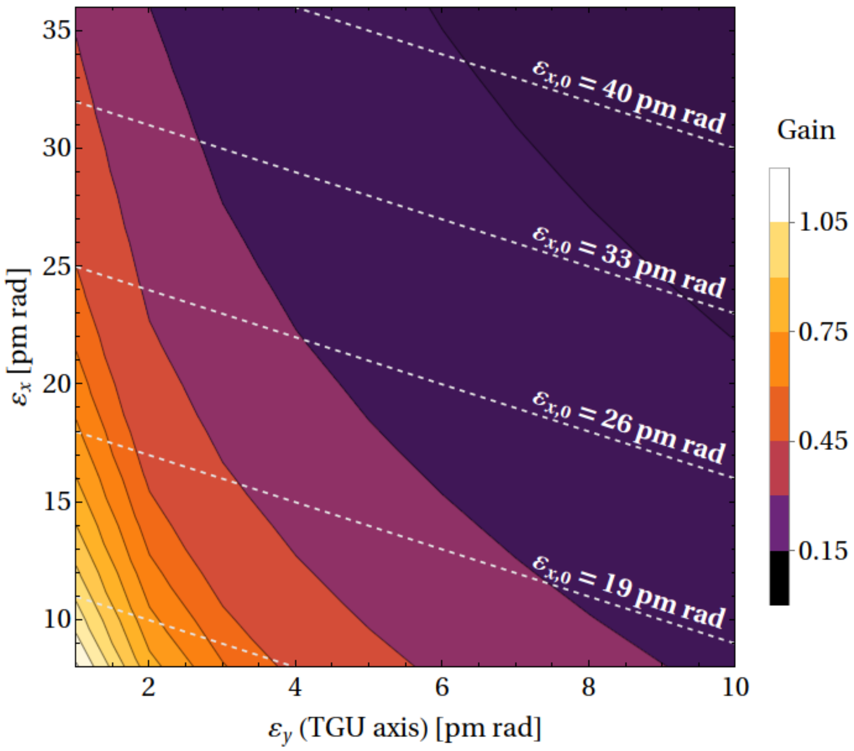

Figure 5.4: Contour plot of gain as a function of transverse emittances $\varepsilon_x, \varepsilon_y$. White dashed lines represent levels of constant natural emittance $\varepsilon_{x,0} \equiv \varepsilon_x + \varepsilon_y$. For fixed $\varepsilon_{x,0}$, reducing the emittance ratio $k_c \equiv \varepsilon_y/\varepsilon_x$ (hence reducing ε_y) results in significant gain improvement. Hence it would be advantageous for the TGU to minimize k_c for given $\varepsilon_{x,0}$.

For instance, a change of 1 pm rad in ε_y can have the same impact on TGU gain as a change of 5 to 10 pm rad in ε_x. Thus, for a fixed $\varepsilon_{x,0}$, we should aim to minimize k_c to maximally reap the benefits of the TGU.

Figure 5.5 shows the gain optimization plots with respect to β_x, β_y and Z_{Rx}, Z_{Ry}. In the horizontal axis, the optimal value lies along the $\beta_x = Z_{Rx}$ line. This agrees with planar FEL theory, which predicts that gain is maximized when the radiation mode size matches that of the electron beam [3]. On the other hand, the TGU gain contour is highly asymmetric in the vertical dimension due to TGU dispersion. (To clarify, β_y reflects the nominal betatron function before the introduction of dispersion.)

During storage ring operation, the beta functions $\beta_{x,y}$ can be constrained by lattice stability requirements. Using once again the 10% gain dropoff threshold, we observe that β_y

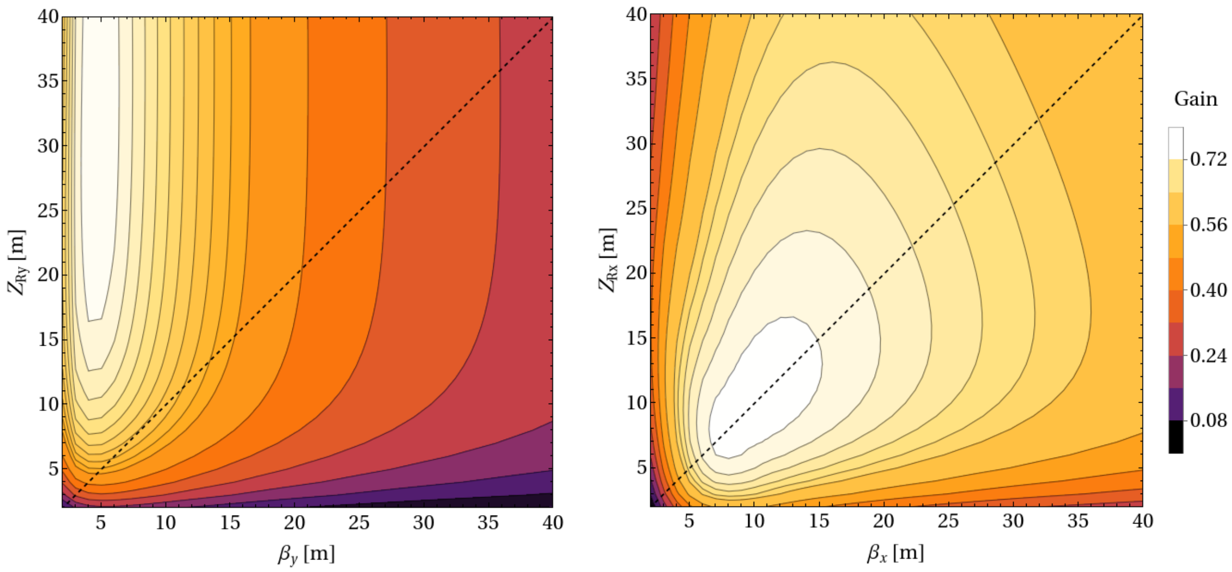

Figure 5.5: Contour plots of gain vs electron and photon beam parameters in x (right) and y (left). In the x-direction, peak gain is located along the $\beta_x = Z_{Rx}$ line (black, dashed) as predicted by traditional FEL theory. In the y-direction, the contours are much more asymmetric due to the dispersion introduced by the TGU. In both directions, there are generous margins for potential tuning while still maintaining respectable gain.

and β_x accept values up to 10 m and 23 m respectively. These ranges encompass the nominal figures for PETRA-IV insertion devices, with a generous margin for additional tuning if necessary.

The Rayleigh ranges Z_{Rx}, Z_{Ry} are similarly constrained in reality, both by practical optical cavity design as well as user requirements. Fortunately, there is also a great deal of tunablility in these parameters. In the horizontal dimension, the optimal Z_{Rx} is always equal to β_x, but a deviation of up to ±10 m still lays within the "acceptable" range. In the vertical dimension, the allowance for sub-optimality is even larger, laying anywhere between 12 m and 50 m. Lastly, one special note should be made for the round-beam case ($Z_{Rx} = Z_{Ry}$), which the chosen case in our study. With this constraint imposed, we observed approximately 10% dropoff from the optimal gain, making it feasible as an actual use case.

In summary, Table 5.3 lists some possible operation points for a TGU-enabled XFELO based on PETRA-IV parameters. Aside from the optimal case, we include a weak dispersion

Parameter	Symbol [unit]	Set A	Set B	Set C
Gain (theory)	G_{th}	0.29	0.36	0.42
Gain (sim)	G_{sim}	0.34	0.36	0.48
TGU parameter	Γ	5	12	13.3
Betatron function in x	β_x [m]	6.0	6.2	8.2
Betatron function in y	β_y [m]	8.4	14.1	4.5
Rayleigh length in x	Z_{Rx} [m]	6.0	14.1	8.2
Rayleigh length in y	Z_{Ry} [m]	14.8	14.1	47.5
Freq. detuning	δ	4.495	2.715	2.722
Dispersion	D [cm]	3.2	6.5	6.2
TGU gradient	α [1/m]	85	42	45

Table 5.3: Table of optimized TGU parameter sets. From left to right, the parameter sets represent (A) capped dispersion, (B) round beam constraint, and (C) unconstrained optimum. The final chosen set for the SRXFELO study was based on Set C.

scenario (when dispersion needs to be controlled), and an optimized round-beam case (when the X-ray beam needs to have a symmetric profile). In all cases we find more than sufficient gain to drive a low-gain oscillator.

For our numerical study, we used the optimal TGU case with the modification $Z_{Rx} = Z_{Ry} = 8.2\,\text{m}$. The reason we did not use the optimized round beam case is largely due to ease of comparison with the optimal TGU case. Despite not optimizing for the round beam, our test parameters returned gain values very close to the optimized case—thanks to the weak sensitivity of TGU gain with respect to Z_{Ry} as discussed previously. All in all, we observed a great deal of flexibility when choosing beam parameters for the TGU, which allows these parameters to be dictated by the other parts of the overall machine design.

5.2 Projected performance

Using the numerical framework in Section 4.4 and the previously discussed study parameters, we performed multi-pass, time-dependent simulation studies of the proposed SRXFELO. We report on the results in this section.

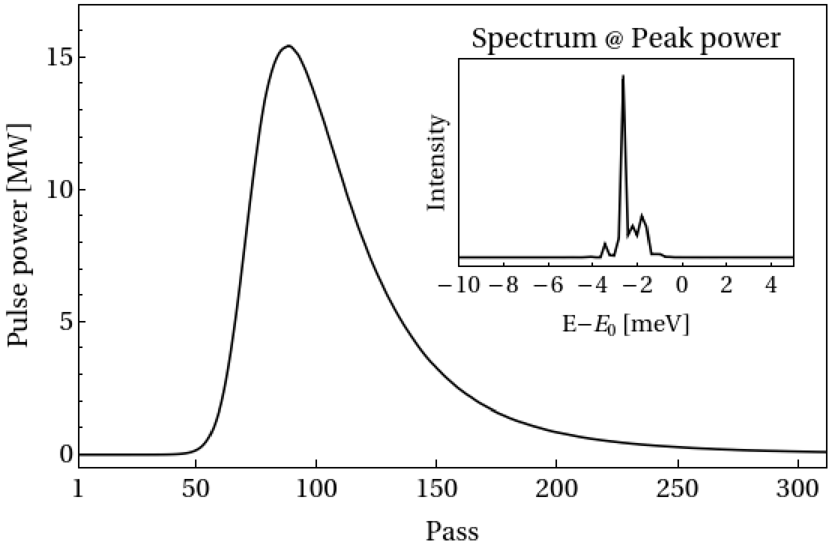

Figure 5.6: Plot of XFELO pulse power vs. turn number from numerical simulation. Maximum power of 15 MW is achieved at turn 95. The inset shows the frequency spectrum at peak power. The spectrum has a full-width half-maximum (FWHM) of 2 meV corresponding to a relative bandwidth of 1.4×10^{-7}.

The macrotemporal evolution of XFELO pulse power is shown in Figure 5.6. Peak intracavity power of 15 MW was achieved at turn 95 after initial onset. With 15% thin-mirror outcoupling, this corresponds to 2.25 MW of usable power. At peak power, the photon bandwidth has a full-width half-maximum (FWHM) of approximately 2 meV (relative bandwidth of 1.4×10^{-7}).

Contrary to previous studies [41], we observed multiple peaks within the overall photon bandwidth, rather than a single one. We attribute this difference to the length of the electron bunch (or simulation window in the case of constant bunch current). In previous studies, a relatively short bunch with $\sigma_t \lesssim 2$ ps was used. This is, however, less feasible in practice where IBS and Touschek lifetime considerations in the storage ring limit realistic values of RMS bunch length to 20 to 50 ps for the desired peak currents.

In order to conserve simulation time and memory, we chose a 20 ps simulation window with a constant current profile. On average, we observed ~ 4 peaks within the FWHM bandwidth. For longer electron bunch lengths, we predict that more peaks would arise within the same overall bandwidth, with the width of each peak set by the Fourier limit. In order to verify this, we ran a number of additional numerical experiments of low-gain oscillators, both with and without the TGU. We found empirically that the total FWHM bandwidth in saturation has a lower bound between five to ten times smaller than the crystal bandwidth σ_ω. For electron bunch lengths shorter than $\sim 5/\sigma_\omega$, the output has one single spectral peak as a result of the Fourier limit. On the other hand, longer bunches can result in multiple spectral modes within the overall bandwidth of $\sigma_\omega/5$. Currently, we do not have a rigorous theory to indicate if this limit is fundamental or to what extent it may be changed—this would be an area deserving of further study.

In the bowtie cavity, we observed maximum TGU gain of approximately $G_{\text{TGU}} = 0.3$, after accounting cavity losses and intentional outcoupling. This includes losses due to absorption and transmission at all four Bragg crystals. All optical components are otherwise assumed to be free of imperfections. In the next chapter, we will examine the impact of optical imperfections, such as misalignments and phase errors, on cavity performance. With a net round trip gain of 0.3, there is a healthy margin for these additional losses.

Figure 5.7 shows the beam profile at peak power, imaged at waist 1. We measure RMS beam sizes of $\sigma_x = 14\,\mu$m and $\sigma_y = 12\,\mu$m. While the nominal beam is intended to be round ($\sigma_x = \sigma_y$), the slight asymmmetry is attributed to the angular filtering of the Bragg crystal, which only takes place in the horizontal plane of the cavity. The narrow angular bandwidth imposed by the crystals results in a corresponding increase in the beam size in x.

In the electron beam, we observed an almost four-fold increase in vertical emittance ε_y from 2.7 pm rad to 10 pm rad at saturation (Figure 5.8). This is a natural consequence of the FEL amplification process, as discussed in Section 2.2.4. Recall from Eq. (2.108) that the X-ray beam induces energy spread gain in the eletron bunch in a regular planar FEL. This induced energy spread is translated into vertical emittance growth due to TGU dispersion.

Thus, as the X-ray beam grows exponentially in power, vertical emittance ε_y becomes

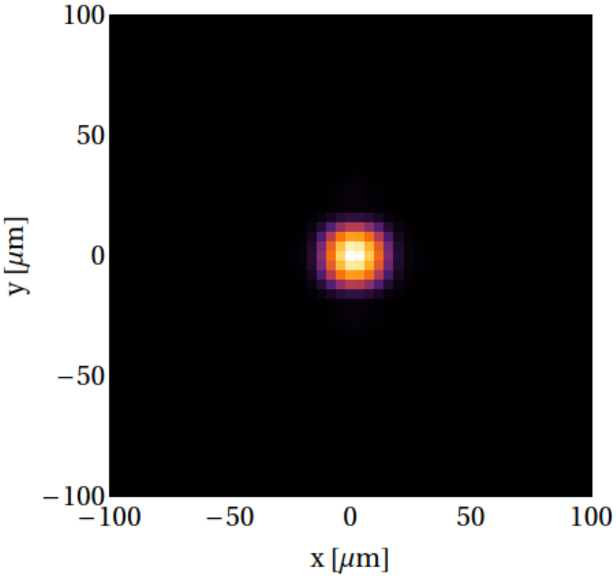

Figure 5.7: Simulated X-ray beamspot at peak power. The root-mean-square (RMS) beam sizes are $\sigma_x = 14\,\mu\text{m}$ and $\sigma_y = 12\,\mu\text{m}$. The slight asymmetry, despite the symmetric cavity, is due to the Bragg crystal filtering acting only in the horizontal plane.

increasingly degraded by the strong radiation field. This in turn reduces TGU gain. Eventually, emittance growth is so severe that net round trip gain falls below zero. At this point, saturation is reached and the X-ray power begins to decline. The emittance growth continues but at a decreasing rate corresponding to the falling X-ray power, until it eventually levels out. This marks the end of one single XFELO pulse.

Over a much longer timescale, ε_y will slowly damp down due to synchrotron emission along the ring. This is discussed in detail in Section 2.3.2. Once it is reduced to a sufficiently low value (not necessarily the equilibrium value) the entire process can begin anew for the next macropulse. In the following section, we will discuss this process in greater detail, and examine some implementation challenges associated with ring-FEL coupling.

5.3 Ring-FEL coupling and other challenges

The X-ray cavity and storage ring constitute a coupled oscillator system. The physics of the storage ring FEL has been previously studied in the UV/IR regimes [17, 19, 20]. Though the

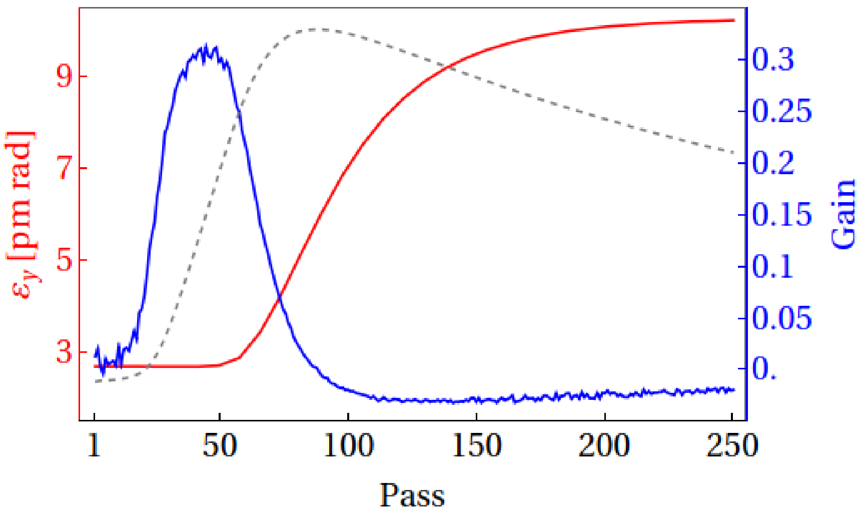

Figure 5.8: Plot depicts the degradation of electron emittance ε_y (red) due to FEL power (gray dashed) within a single oscillator pulse. Initially, the low emittance ε_y enables a large positive gain (blue), which in turn exponentially amplifies the X-ray power (dashed gray; vertical log scale not shown). The increasing X-ray power degrades ε_y due to the TGU-FEL interaction. Near saturation, emittance ε_y has increased so much that gain falls below zero, leading to the exponential decay of the X-ray pulse.

energies involved here are greater, much of the theory, especially relating to the ring-FEL interaction, remains relevant in the X-ray regime. For the sake of the following discussion, we provide here a short summary of the most salient points adapted from [19, 20].

In a storage ring FEL, there exists a tension between the electrons circulating in the ring and the photons circulating in the cavity. Namely, as photon intensity increases, the electron bunch suffers increasing degradation of its energy spread. This in turn leads to the reduction of FEL gain, and eventually, the saturation and decline of laser power. The addition of the TGU modifies this interaction in one important aspect—electron beam degradation takes place in the TGU-axis transverse space (y in our case), rather than longitudinally. This is because of the dispersive sections before and after the undulator, which effectively translates the energy spread growth generated by the FEL into excess emittance in the ring.

Hence, the macrotemporal dynamics of the TGU-enabled storage ring FEL can be described by the following linearized equations:

$$
\begin{aligned}
\frac{dU}{dt} &= U\frac{g-L}{\theta} + U_s, && (5.1)\\
\frac{d(\varepsilon_y)}{dt} &= -\frac{2}{\tau_y}(\varepsilon_y - \varepsilon_{y,0}) + \Delta_U, && (5.2)\\
g &= g_0 \exp\bigl(-k(\varepsilon_y - \varepsilon_{y,0})\bigr)\,[1+F(t)]\,. && (5.3)
\end{aligned}
$$

Here, U is the FEL intensity, g, L, θ are the gain, loss and transit time for each turn respectively, U_s is the intensity of the spontaneous emission, $\varepsilon_{y,0}$ is the equilibrium y emittance, τ_y is the characteristic emittance damping time, Δ_U is the increase in emittance due to laser intensity, g_0 is the maximum gain at equilibrium emittance, and $F(t)$ represents an optional external gain modulation imposed on the system.

Figure 5.8 depicts the evolution of these three parameters over a single FEL pulse. At first, the photon intensity is dominated by spontaneous emission, which quickly gets overtaken by FEL amplification as the equilibrium emittance $\varepsilon_{y,0}$ enables the maximum theoretical TGU gain g_0. The exponential rise in photon intensity results in increasing degradation of ε_y, which causes g to suffer. Finally, at saturation, g falls below single turn loss L (such that $g - L \leq 0$), which marks the start of the exponential decay of the photon pulse. This whole process takes place over hundreds of oscillator turns, with a characteristic rise time on the order of microseconds. On the much longer timescale, the electron bunch damps in ε_y as it circulates within the storage ring (typically over tens to hundreds of milliseconds). This process is explained in Section 2.3.2.

Thus, the ring-FEL system behaves like a coupled oscillator with two drastically different timescales. On the one hand, the laser is characterized by its rise time $\tau_0 \sim 10^{-6}\,\mathrm{s}$. On the other hand, emittance damping is set by $\tau_y \sim 10^{-2}\,\mathrm{s}$. Using Eqs. (5.1)–(5.3), we can determine the natural period of the system to be

$$T_R = 2\pi\sqrt{\frac{\tau_0\tau_y}{2}}. \tag{5.4}$$

The system is extremely sensitive to initial conditions, displaying chaotic and noisy behaviour close to this natural resonance [17, 18]. A more stable alternative can be achieved by modulating the gain periodically in the FEL so as to effectively "turn on" and then "turn off" the XFELO. Thus, the laser can operate in a pulsed fashion with greater stability. The duty cycle of the modulation is given by: (a) "off" state for several τ_y damping times (tens to hundreds of milliseconds), then (b) "on" state for several τ_0 laser rise times (tens of microseconds) until saturation. The laser switches itself off due to emittance degradation at saturation.

Gain modulation can be achieved by essentially disrupting the temporal and/or spatial overlap between the electron bunch and the photon pulse, thus suppressing the FEL interaction. For our proposed parameters, a temporal displacement of $\sim$ 20 to 50 fs between consecutive bunches is sufficient to "switch off" the XFELO. This can be done by detuning the storage ring RF system to the order of tens of Hz. This method has been experimentally tested, albeit on a smaller scale, at the Duke storage ring FEL [18]. Other potential gain modulation methods include transversely displacing the electron trajectory in the undulator (e.g. with a kicker) or manipulating the X-ray cavity length/geometry, although to perform the latter at the required millisecond time scale without compromising cavity stability remains an open area of research.

One additional note must be made about the ring-FEL coupling strategy. Since the storage ring circumference is typically many times the length of the X-ray cavity, it is necessary to have multiple electron bunches spaced around the ring with temporal separation matching the cavity round-trip time. In the numerical study, we had a ring-cavity circumference ratio of 16, meaning that we had 16 of these "XFELO bunches". This is a fraction of the hundreds,

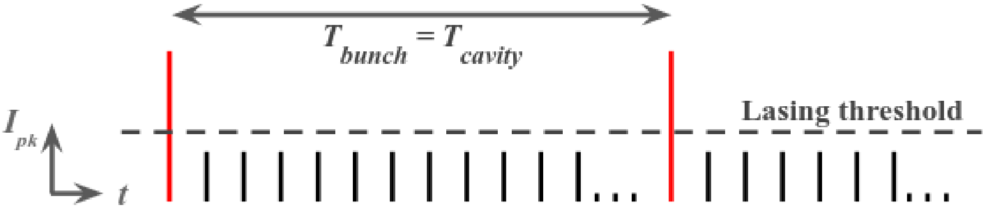

Figure 5.9: Proposed bunch train structure for ring-FEL coupling. Each vertical line represents one bunch, with its height proportional to peak current I_{pk} and thus TGU gain by Eq. (3.14). Tall red bunches are the designated "XFELO bunches" with I_{pk} exceeding the lasing threshold set by single-turn cavity loss. The temporal gap between XFELO bunches T_{bunch} is equal to the X-ray round-trip time T_{cavity}. The non-XFELO bunches (black) lay below the lasing threshold and only experience spontaneous undulator radiation. Thus they are able to avoid substantial emittance degradation from the XFELO lasing process.

if not thousands, of simultaneously circulating bunches present in a modern storage ring.

As discussed previously, the XFELO lasing process leads to significant emittance degradation due to the elevated laser intensity. We would like to isolate this detrimental effect to only the XFELO bunches while leaving the non-XFELO bunches relatively unperturbed. The problem of selecting for the XFELO bunches is non-trivial [16].

One commonly proposed technique is to situate the XFELO on a bypass with fast transverse kickers, which periodically kick the XFELO bunches into the oscillator. This is not feasible when the closely spaced electron bunches are only separated by gaps on the order of single to tens of nanoseconds. Even if the rise/fall time of the kicker fits within the bunch separation, its repetition rate is not fast enough to support the oscillator [42].

Our current proposal is to utilize bunch charge stacking (Fig. 5.9). Under this scheme, the XFELO bunches, spaced at the appropriate periodic interval, are intentionally injected with multiple times the nominal bunch charge, while adjacent RF buckets are left empty to compensate for the beam loading effect. This technique has precedence in the APS-U, where it is employed to mitigate ion instabilities [43].

Since TGU gain is linearly proportional to peak current in the low gain approximation, the XFELO bunches will experience proportionally more gain than the non-XFELO ones.

Then, it suffices to set the single turn loss within the cavity (for instance, using outcoupling methods) to be higher than the gain experienced by non-XFELO bunches, but lower than that of the XFELO bunches. Thus only the latter will experience exponential growth and the subsequent emittance degradation due to the intense laser field near saturation. The non-XFELO bunches will only undergo spontaneous undulator radiation, which will not cause substantial emittance increase.

In our numerical study, we chose the non-XFELO bunches to have a total charge of $Q_b = 1\,\mathrm{nC}$, with a corresponding peak current of $I_{\mathrm{pk}} = 10\,\mathrm{A}$, whereas the stacked XFELO bunches have $Q_b = 4\,\mathrm{nC}$ and $I_{\mathrm{pk}} = 32\,\mathrm{A}$, after accounting for bunch lengthening due to intra-beam scattering (IBS) and ring impedance. Single turn loss is set to approximately 0.15 via thin mirror outcoupling.

CHAPTER 6

CAVITY-BASED X-RAY FEL (CBXFEL) EXPERIMENT

The Cavity-based X-ray FEL (CBXFEL) project aims to provide the world's first experimental demonstration of an X-ray FEL cavity. It is a collaboration between Argonne National Laboratory (ANL), SLAC National Accelerator Laboratory, and Super Photon ring-8 GeV (SPring-8) of Japan. The experimental setup is physically located at the Linear Coherent Light Source (LCLS) facility at SLAC [21].

The experiment will enclose the first seven undulators of the LCLS within a 4-mirror rectangular cavity (Fig. 6.1). The 4-mirror optical cavity will utilize diamond Bragg reflectors in the C400 geometry with 45 degree angle of reflection, along with two beryllium CRLs for focusing. The goal of the experiment is to observe second pass gain—that is, having the photon pulse generated from spontaneous emission in the first pass make a full round trip in the cavity and be amplified by the second, trailing electron bunch.

The electron bunches are supplied by the LCLS normal conducting linac with 120 Hz RF repetition rate. Alone, the RF cavities are too slow to keep up with the $\sim 220\,\mathrm{ns}$ cavity round trip time. Instead the CBXFEL experiment will rely on two bunch generation, wherein twin lasers in the LCLS photoinjector system will fire with the desired temporal separation to generate two consecutive electron bunches. The two bunches will then be accelerated in separate RF buckets.

There will be two principal modes of operation in this experiment — the low gain XFELO mode, and the high gain X-ray regenerative amplifier (XRAFEL) mode. The primary difference between the two modes are the electron peak current and bunch length. Table 6.1 lists some key parameters of the experiment.

In the context of this thesis, the CBXFEL experiment serves as a key demonstration of the operational viability of the XFELO. Although the electron driver in this case is a linac, many of the challenges associated with the X-ray optical cavity remain the same. In the

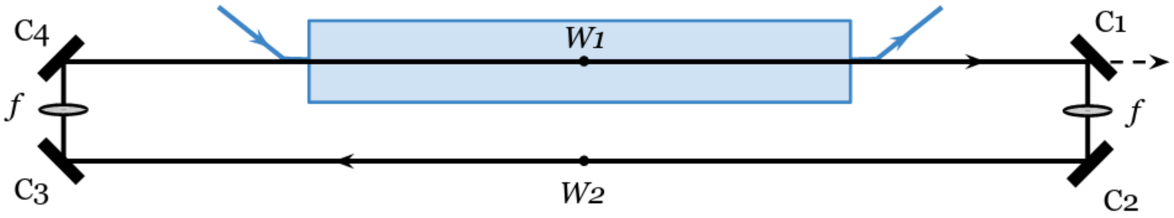

Figure 6.1: Layout of the Cavity-based X-ray FEL (CBXFEL) experiment. The four-mirror rectangular cavity encloses the first seven undulators of the LCLS (blue rectangle).

Parameter	Value
Electron energy	10.3 GeV
Peak current (XFELO, XRAFEL)	0.333, 3 kA
Bunch length (XFELO, XRAFEL)	300, 50 fs
Photon energy	9831 eV
Undulator period	2.6 cm
Number of periods	7 × 130
Undulator parameter	2.44
Cavity length	65.3 m

Table 6.1: Table of key CBXFEL experiment parameters.

following sections, we will examine two of these issues—cavity alignment and phase front errors—in the context of the CBXFEL experiment, while keeping in mind that much of the discussion is also relevant for storage ring XFELO.

6.1 Simulation model

Figure 6.2 shows a flowchart of the simulation model used in this study. The FEL portion of the code is handled by `GENESIS` while the cavity propagation is done using a precursor to `pyopt` (operating on identical physics principles). There are two main types of simulation runs. The first is a two-pass 3D run in order to determine the projected photon count within the diamond crystal bandwidth. From this data, we are able to calculate the two-pass gain, a key metric for the experiment. We are also able to study the projected impact of various

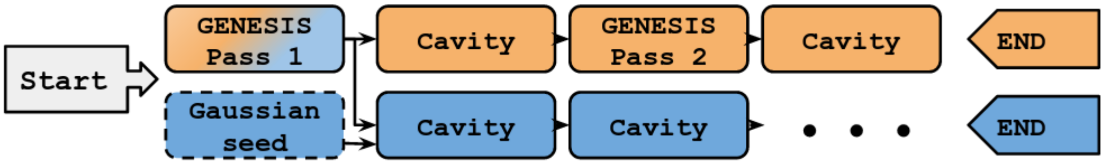

Figure 6.2: Flowchart depicting the simulation process of the CBXFEL experiment. The two primary run modes are two-pass (orange) and ring down (blue). For the ring down runs, one may optionally use a Gaussian seed (dashed outline) instead of `GENESIS` output. The cavity simulation step is similar to that depicted in Fig. 4.2.

cavity misalignments.

The second mode is the ringdown study, where the X-ray beam is allowed to circulate the cavity for a large number of passes (usually 10-25) without FEL amplification. By tracking the pulse power over each turn, we are able to determine the round trip loss and cavity quality factor. We are also able to track the transverse beam spot and RMS sizes. This allows us to investigate the impact of phase front imperfections.

6.2 Cavity alignment

Peak FEL gain occurs when there is maximal overlap between the co-propagating electron and X-ray beam within the undulator. This overlap can be disrupted due to unintentional misalignments in the longitudinal and transverse domains.

Longitudinal misalignments

In the longitudinal domain, the electron bunch may arrive too early/late, or at the wrong energy. This is primarily determined upstream by the two bunch generation laser system. Any slight mistiming in the setup can translate into significant energy differences, due to the position of the bunch relative to the RF accelerating potential.

Figure 6.3 shows the simulated second-pass photon count versus second-bunch temporal and energy displacements. In the temporal domain, the XFELO nominal bunch length is

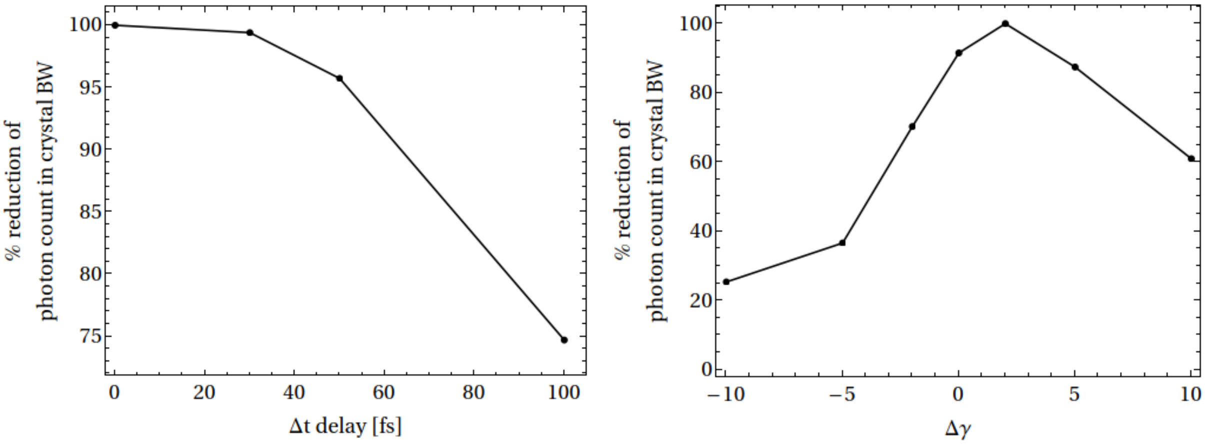

Figure 6.3: Plot of second-pass photon count reduction versus temporal (left) and energy (right) misalignments. Each data point represents a single two-pass simulation with fixed seed to eliminate the impact of shot noise.

300 fs. We observe that a delay of less than ~ 30 fs, or 10 percent of the bunch length, will lead to negligible gain dropoff. In the high gain XRAFEL mode, we foresee a much more stringent timing requirement for negligible gain dropoff, due to the shorter nominal bunch length of 50 fs. However, in XRAFEL mode the estimated peak gain is $G \sim 100$, meaning that even a 50 percent overlap would likely provide detectable second-pass amplification, which would fulfill the experimental goal. Thus, we determined that an overall timing tolerance of 25 to 30 fs would satisfy both XFELO and XRAFEL test acases.

In the energy domain, the energy difference between the two bunches should ideally be less than half the undulator bandwidth, i.e. less than $1/2N_u \sim 5 \times 10^{-4}$. This is consistent with simulation result, which indicates that a gap of $\Delta\gamma \lesssim 1$ or $\Delta\gamma/\gamma \lesssim 5 \times 10^{-5}$ would lead to negligible impact on second-pass gain. Also notice that peak photon count is achieved slight above the nominal electron energy, which is consistent with our understanding of peak gain at positive detuning (Sec. 2.2.3).

Transverse misalignments

One important source of transverse cavity misalignment comes from the cavity mirrors. Let us assume that the four mirrors are misaligned by $\theta_{m1}, \theta_{m2}, \theta_{m3}, \theta_{m4}$ radians respectively. The resulting displacement of the photon beam, relative to the nominal axis, is a linear combination of these misalignments:

$$\Delta x = c_1\theta_{m1} + c_2\theta_{m2} + c_3\theta_{m3} + c_4\theta_{m4}, \tag{6.1}$$

$$\Delta\phi = f_1\theta_{m1} + f_2\theta_{m2} + f_3\theta_{m3} + f_4\theta_{m4}, \tag{6.2}$$

where coefficients c_i, f_i are calculated from cavity drift distances and focal lengths using the ABCD ray transfer matrix. For the CBXFEL cavity, we have $c_1 = c_2 = 22\,\mathrm{m}$ and $c_3 = c_4 = 33\,\mathrm{m}$, as well as $f_1 = f_2 = -2.6$ and $f_3 = f_4 = 2$.

Let us then assume that the θ_i are independent and identically distributed[1] with zero mean and standard deviation σ_m. The RMS angular and position deviations are given by

$$\sigma_x = \sigma_m\sqrt{c_1^2 + c_2^2 + c_3^3 + c_4^2}, \tag{6.3}$$

$$\sigma_\phi = \sigma_m\sqrt{f_1^2 + f_2^2 + f_3^2 + f_4^2}. \tag{6.4}$$

The values for the CBXFEL cavity are $\sigma_x = 56\sigma_m\,\mathrm{m}$ and $\sigma_\phi = 4.6\sigma_m$. In other words, if we are able to determine tolerance values for σ_x, σ_ϕ, the above equations allow us to work out the corresponding tolerance on mirror angular stability σ_m.

Transverse displacement error reduces FEL gain. For given electron beam size σ_x and radiation mode size σ_r, the reduction in FEL power for a relative displacement of Δx can

---

[1] Note that there is no *a priori* justification for this assumption—in fact, environmental factors such as temperature and seismic movement may cause the errors to be correlated in some fashion. Nevertheless, the present assumption of independence provides a reference point for further analysis. It is important to keep correlated errors in mind when considering the "worst case" misalignment scenarios.

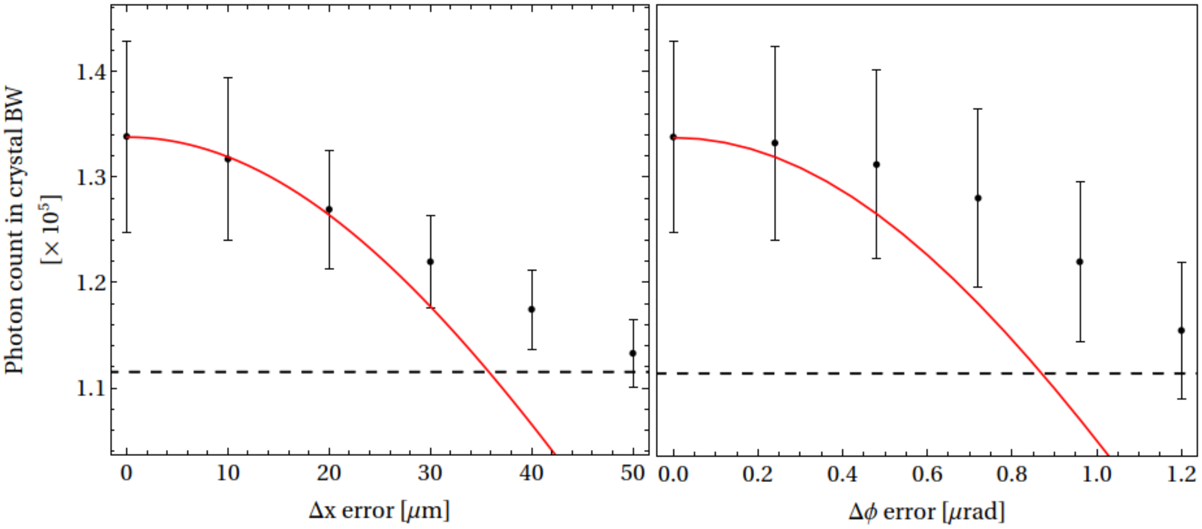

Figure 6.4: Plot of second-pass photon count versus transverse misalignment Δx (left) and $\Delta\phi$ (right). Data points show data from $n = 20$ two-pass simulations, with error bars indicating RMS variation due to shot noise. The red plots show theoretical relationship given by Eq. (6.5). At large misalignments, the data deviates from the theoretical value and trends towards the two-pass spontaneous emission background (black dashed).

be estimated by

$$P = P_0 \exp\left(-\frac{(\Delta x)^2}{2(\sigma_r^2 + \sigma_x^2)}\right) \tag{6.5}$$

where P_0 is the initial power without misalignment. An equivalent expression exists for angular overlap between $\sigma_{x'}$ and σ_ϕ.

Figure 6.4 shows the second pass photon count (directly proportional to power) as a function of transverse displacements Δx and $\Delta\phi$. The data was obtained from $n = 20$ two-pass simulation runs. For comparison, Eq. (6.5) is shown in red. Initially, the power dropoff follow the theoretical relationship. However, for large displacements, the numerical result asymptotically approaches the base level of $\sim 1.1 \times 10^5$ photons—the spontaneous emission background (black dashed line). We observe negligible impact on performance for displacements $\Delta x \lesssim 8\,\mu$m and $\Delta\phi \lesssim 0.2\,\mu$rad. Taking the more stringent result for angular overlap, this leads to the conclusion $\sigma_m \lesssim 50\,$nrad.

In order to verify that this limit is sufficient, we ran 60 independent instances of the two-

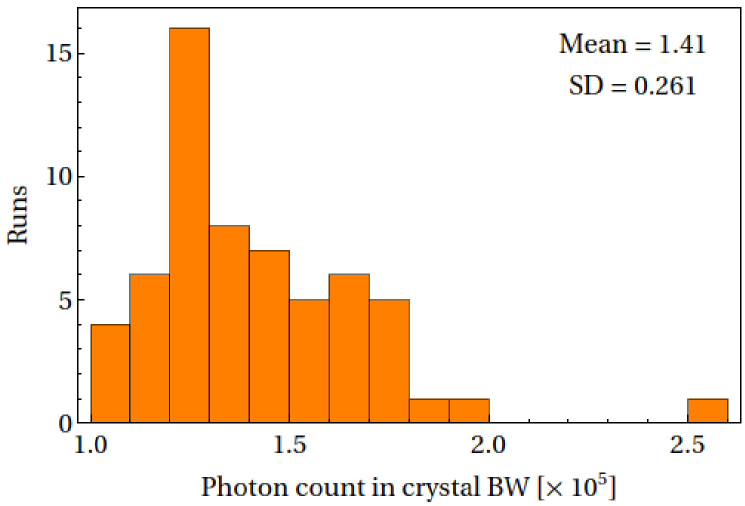

Figure 6.5: Histogram of second-pass photon count from $n = 60$ two-pass simulations using randomly sampled mirror misalignments with $\sigma_m = 50\,\text{nrad}$. There is no observable difference from ideal conditions.

pass gain simulation with mirror errors randomly distributed according to $\sigma_m \sim 50\,\text{nrad}$. Figure 6.5 shows a histogram of the second pass photon count. At this level, there is no observable difference from the ideal case.

6.3 Phase front error

Phase error in diamond crystals arises due to irregularities in the Bragg reflection planes. This can occur on the crystal surface in the form of surface roughness, or within the crystal interior due to mechanical strain. When an initially coherent beam reflects off the crystal, the crystal imperfections introduce a transversely-dependent phase factor into the beam wavefront, per Eq. (4.15), thereby spoiling the transverse coherence of the beam.

In CRLs, one additional source of phase error comes from its material composition. Beryllium is the dominant element used for CRL construction due to its low atomic number and very low absorption of X-rays. In the manufacturing process, the elemental Be is contaminated by oxide formation, resulting in beryllium oxide BeO. The level of BeO impurity, when combined with the grain size and anisotropy properties determined by the manufacturing technique, is the primary source of phase error in CRLs [44].

Error measurement and quantification

As discussed in Section 4.1, we relied on a multitude of sources for phase front error data, including rocking curve imaging, speckle tracking, and artificial generation. Each error profile is subject to data preprocessing, where it is segmented into the appropriate window size and formatted into a 2D array of effective phase shifts $\varphi(x, y)$.

Given an error profile, we wish to measure its “quality”. In fact, there are several useful metrics. The first is the RMS phase variation σ_φ after subtracting the zeroth and first order terms[2]. The remaining phase terms are the residuals from fitting the data to a best-fit plane. The RMS variation of these residuals gives an idea of the level of phase fluctuations in each data set.

The RMS phase variation σ_φ can also be converted into an effective height variation σ_h. Based on the 90 degree reflection geometry of the CBXFEL cavity, we can show that for a given height deviation Δh, the resulting phase error is

$$\Delta\phi(x, y) = \frac{2\sin\theta\Delta h(x, y)}{\lambda} \tag{6.6}$$

where $\theta = 45$ degrees. Whereas σ_φ is dimensionless and vary between 0 and 2π, σ_h has units of distance and can intuitively be compared to λ. For this reason, RMS phase error is frequently quoted in units of λ, e.g. $\sigma_h \sim \lambda/100$.

The final metric adopted in this study is the *Strehl ratio.* Given a surface with error

---

[2] The zeroth order error represents a constant phase shift to the entire wavefront, which corresponds to an effective path length difference. Similarly, the first order (linear) error introduces an overall angular misalignment. Both errors are accounted for during the cavity alignment process.

profile $\varphi(x, y)$, the Strehl ratio S is calculated from

$$S = \left| \left\langle e^{ik\varphi} \right\rangle \right|^2, \tag{6.7}$$

where $\langle \cdot \rangle$ indicates taking the average over the 2D surface. Values of S range between zero and unity, with the latter representing an error-free optical element.

Figure 6.6 demonstrates the crystal data preprocessing using example data sets taken RCI and speckle measurements. We segment the large crystal surface (millimeter-scale) into smaller grid squares corresponding to the simulation window size. Then, we calculate S for each grid square in order to estimate its quality. The regions selected for simulation are then cropped and formatted for the cavity code. Alternatively, we can also perform a window scan over the data set in order to find the best/worst regions for study. Rather than relying on a fixed grid, this method is able to objectively locate the region with the highest/lowest S at the cost of more computation time.

In the case of the simulated error profiles, we are obviously able to specify the desired quality level and data fidelity beforehand, obviating the need for much preprocessing. Nevertheless, it is important that the error spectrum of the generated profile be as close to the real measurements as possible. Figure 6.7 shows a comparison of the noise spectral profiles. We were able to verify similarity down to the feature size of the beam spot ($\sim 20\,\mu$m).

Simulation results

For each simulation run, we select a set of four mirror phase error profiles (two in the case of CRLs) from the measured or simulated data. Each profile covers a 500x500 micron transverse area. We did not always choose regions with the highest S or lowest σ_h, since we wished to explore a wide range of values. Due to the limited amount of measurement data at the time of the study, it is possible for two regions to be selected from the same test crystal, although test regions are never allowed to overlap. If the data set is smaller than 500x500 microns, as is the case for the RCI dataset, we pad it with zeros evenly along all four sides.

Figure 6.8 (left) shows the beam spots after 25 ring down passes for four different sets of crystal error profiles: (a) perfect crystal, (b) speckle, (c) RCI, and (d) synthetic. By partial coincidence, they are also ordered from best to worst by RMS phase error. The best dataset came from speckle tracking partly due to the precision of the technique—capable of detecting phase errors down to $\sim \lambda/100$—and partly due to a change in crystal providence. The RMS phase error for each crystal ranged between $\lambda/100$ to $\lambda/80$. Within this range, we observe minimal deterioration of the transverse beam profile even after 25 passes. The average round trip loss is also close to perfect. At the other extreme, the "worst" dataset was artifically generated to have RMS phase errors ranging between $\lambda/10$ to $\lambda/5$. At this level, there is noticeable negative impact on the beam profile as well as round trip loss.

Figure 6.8 (right) shows the ring down results with CRL error profiles. The error profile is taken from speckle measurement data of physical lenses. We ranked the lenses by RMS phase error within the central 110 μm region, corresponding to approximately 6σ of the X-ray beam spot. Then, we selected the best and worst error profiles for simulation. The results show that phase error in the CRLs have a much smaller, albeit non-negligible, impact on the transverse beam profile.

Interestingly, phase error poses much less problems for high gain XRAFEL operation. Figure 6.9 shows the ring down results for different levels of outcoupling up to 90%. Notice the considerable improvement in transverse coherence as the outcoupling level is increased. In the high gain regime, the transverse beam profile is primarily shaped by powerful gain guiding effects rather than the cavity [3]. Furthermore, the high level of outcoupling means that the recirculating beam makes up only a small fraction of the total beam power, thus greatly suppressing the impact of any phase irregularities.

In summary, our simulation results demonstrate that an acceptable level of phase error is

$\lesssim \lambda/50$ for low gain XFELO operation. While this threshold is partially subjective, it serves as a useful benchmark for crystal/lens selection. More importantly, this study also provides a handy simulation pipeline for benchmarking experimental results during commissioning and operation.

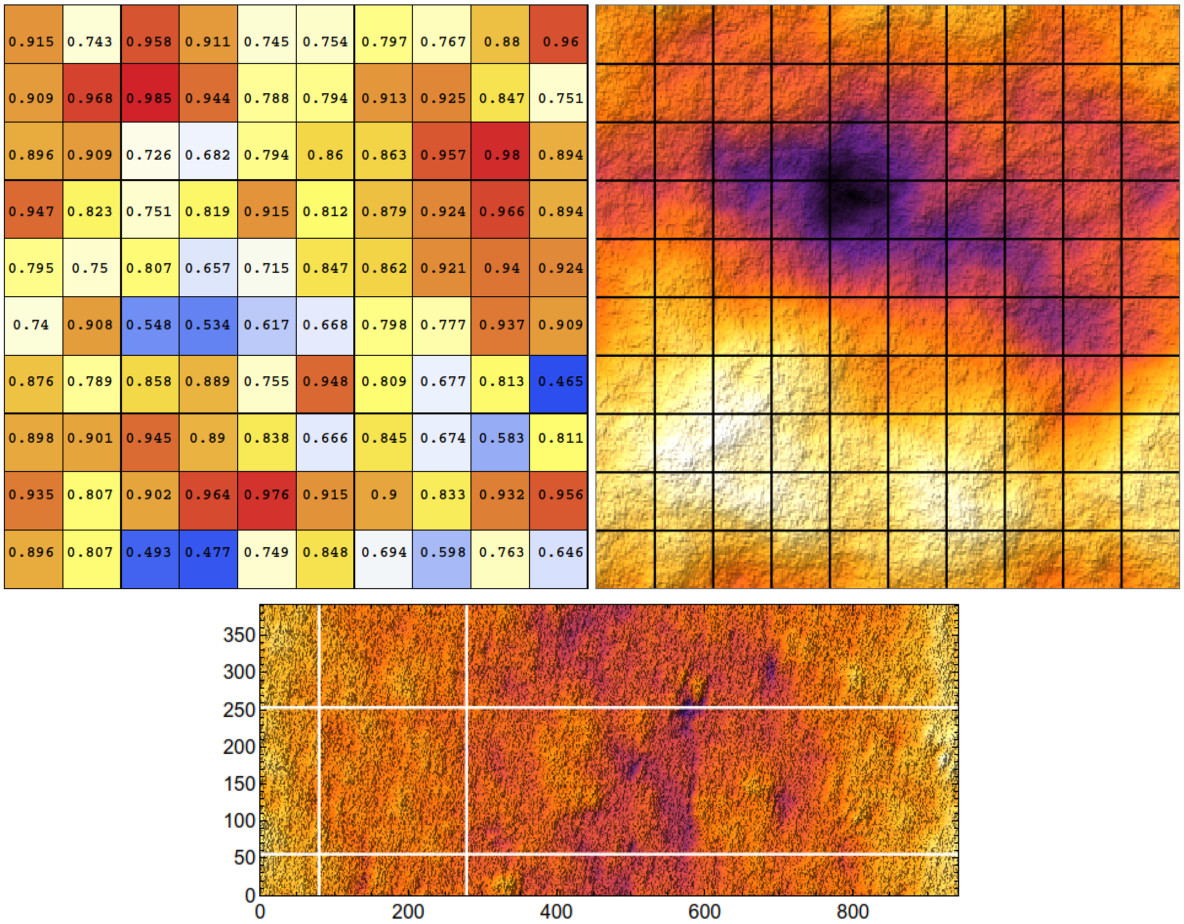

0.915	0.743	0.958	0.911	0.745	0.754	0.797	0.767	0.88	0.96
0.909	0.968	0.985	0.944	0.788	0.794	0.913	0.925	0.847	0.751
0.896	0.909	0.726	0.682	0.794	0.86	0.863	0.957	0.98	0.894
0.947	0.823	0.751	0.819	0.915	0.812	0.879	0.924	0.966	0.894
0.795	0.75	0.807	0.657	0.715	0.847	0.862	0.921	0.94	0.924
0.74	0.908	0.548	0.534	0.617	0.668	0.798	0.777	0.937	0.909
0.876	0.789	0.858	0.889	0.755	0.948	0.809	0.677	0.813	0.465
0.898	0.901	0.945	0.89	0.838	0.666	0.845	0.674	0.583	0.811
0.935	0.807	0.902	0.964	0.976	0.915	0.9	0.833	0.932	0.956
0.896	0.807	0.493	0.477	0.749	0.848	0.694	0.598	0.763	0.646

Figure 6.6: Sample of crystal phase error profiles showing window selection process. *Top:* A grid is applied to the overall crystal data set (right) according to the simulation window size. We then calculate Strehl ratio S for each region (left) in order to select the appropriate regions for further study. *Bottom:* Instead of applying a fixed grid, we can also perform a moving window scan for minimal/maximal S. This is useful for narrowing down the most error-free regions for the actual experiment.

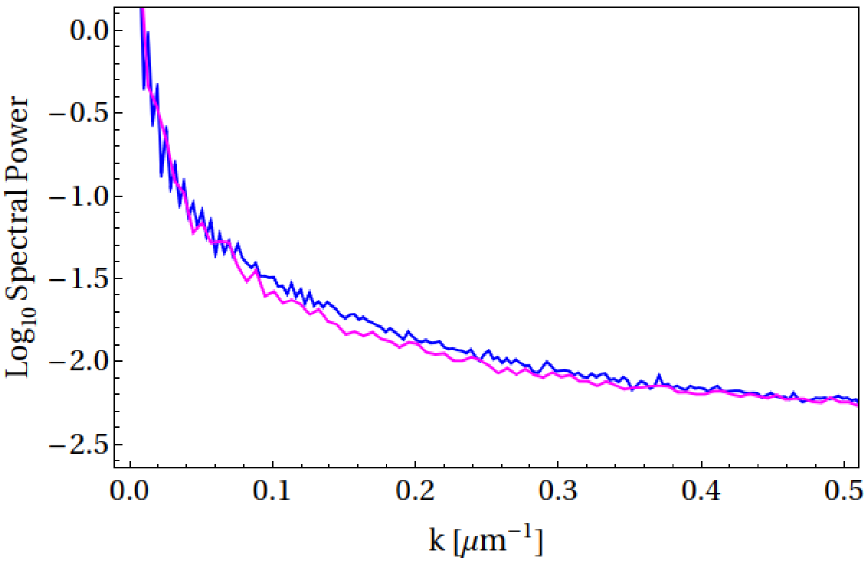

Figure 6.7: Noise spectral power for artificial (magenta) versus measured (blue) phase error data. We observe similar profiles down to at least $k \sim 0.3\,\mu\mathrm{m}^{-1}$, corresponding to the RMS spot size $\sim 20\,\mu\mathrm{m}$.

	No error	Crystal			CRL	
		Speckle	RCI	Synthetic	Best	Worst
rms err.	0	λ/100 ~ λ/80	λ/70 ~ λ/60	λ/10 ~ λ/5	λ/135	λ/25
Beam spot	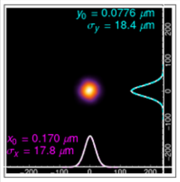	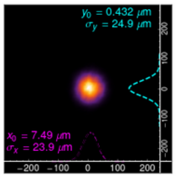	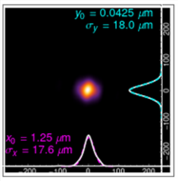	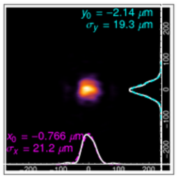	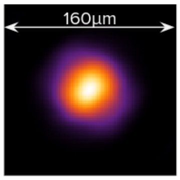	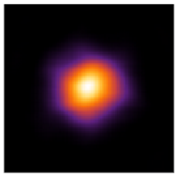
RT Loss	8.4%	8.5%	8.9%	9.2%	8.4%	8.5%

Figure 6.8: Beam spot comparison for ring down simulation with phase error data. Each beam spot was recorded after 25 passes in the cavity, along with round trip (RT) power loss figures. From these simulation results, an acceptable level of phase error was deemed to be $\lesssim \lambda/50$ (per element) for XFELO operation.

Outcoupling	None	50%	90%
Beam spot	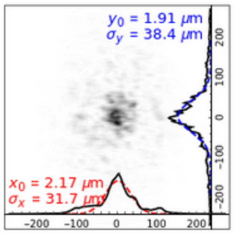	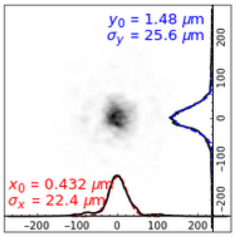	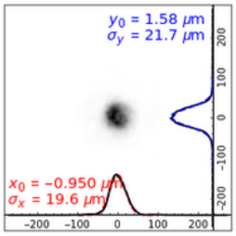

Figure 6.9: Beam spot comparison with different levels of outcoupling for XRAFEL. Beam spot measured after 25 passes in the cavity. At high levels ($\sim$ 90%) of outcoupling, the transverse mode is primarily shaped by FEL gain guiding rather than the cavity mirrors.

CHAPTER 7

CONCLUSION

In this thesis, we examined the theory, simulation, and implementation of a TGU-enabled storage ring X-ray FEL oscillator. Following an introduction to FEL and storage ring physics in Chapter 2, we discussed TGU physics in the low gain approximation and derived the 3D gain equation in Chapter 3. The gain equation Eq. (3.19) permits us to optimize beam parameters for a given TGU design.

In Chapter 4, we discussed the process of constructing an entire start-to-end simulation model for the SRXFELO concept. The model folds in the theory from the previous chapters and allows us to obtain projected performance for a arbitrary set of beam and machine parameters. We examine one such case in Chapter 5 and report on performance figures. Most notably, we go into detail about potential challenges facing the ring-FEL coupling implementation.

Finally, in Chapter 6, we reported on optical cavity simulations for the CBXFEL collaboration. The experiment serves as a testbed for future XFELO cavity designs, and much of the results remain relevant for future machines. We focused on issues relating to beam alignment and optical phase front purity, and derived practical engineering tolerances using simulation.

The results of this study demonstrate that the TGU-enabled SRXFELO can be a feasible inclusion for modern storage rings, and thus is deserving of further study. There remains undoubtedly many other challenges which we do not have time to discuss in this thesis. However, we hope that the mathematical and numerical framework derived for this study will serve as a useful starting point for modeling future SRXFELO designs in a wide range of practical circumstances.

Future work

In the short term, there are a number of problems that could be interesting to study. First, as mentioned in the performance results in Chapter 5, the SRXFELO exhibits multiple frequency modes within the overall crystal bandwidth. We hypothesized that this could be due to the longer electron bunch length corresponding to narrower Fourier-limited modes. It would be useful to derive a more mathematically rigorous explanation in this regard.

In previous studies of SRFELOs [17, 18, 20], it was observed that continuous-wave (CW) operation of the oscillator is also possible under the correct circumstances. In our hypothetical test case, we were unable to find a feasible CW mode of operation. However, it may be worth exploring whether such CW designs may exist under a different set of machine parameters.

As of the time of writing, the CBXFEL experiment will be up and running in 1-2 years. The actual measurements from this experiment will serve as a useful benchmark of our analytical and numerical models. There is also the possibility to extend the cavity module of the framework—for instance, on-the-fly generation of the crystal bandwidth based on input parameters (currently performed with an external program), as well as introducing new optical componentry such as diffraction gratings and X-ray beam position monitors.

Finally, as a longer term project, it is worthwhile to consider consolidating the FEL and cavity portions of the numerical model. This could lead to large improvements in computational efficiency, since the radiation file (the primary bottleneck) will no longer be written and read from disk every turn. It would be a significant undertaking that would streamline the simulation process for future XFELO projects.

APPENDIX A

DERIVATION OF 3D TGU GAIN

We start from Eq. (3.13). For future convenience, we perform a change of variables $\vec{\boldsymbol{\phi}}-\vec{\boldsymbol{p}} \to \vec{\boldsymbol{\phi}}$ and $\vec{\boldsymbol{x}} - \vec{\boldsymbol{y}} \to \vec{\boldsymbol{x}}$. We also use integration by parts to switch the derivative, thus obtaining

$$\begin{aligned} G &= -\frac{G_0}{8\pi N_u L_u^2 \lambda_1^2} \int d\eta d\vec{\boldsymbol{x}} d\vec{\boldsymbol{y}} d\vec{\phi} d\vec{\boldsymbol{p}}\, B_E(\vec{\boldsymbol{y}}, \vec{\boldsymbol{\phi}} + \vec{\boldsymbol{p}}) \\ &\qquad \times \frac{\partial}{\partial \eta} B_U(\eta, \vec{\boldsymbol{x}}, \vec{\boldsymbol{\phi}}, \vec{\boldsymbol{p}}, \vec{\boldsymbol{y}}) F(\eta, \vec{\boldsymbol{x}} + \vec{\boldsymbol{y}}, \vec{\boldsymbol{p}}). \end{aligned} \tag{A.1}$$

Since the two transverse dimensions are decoupled, we drop the vector notation and focus on the TGU dimension y. (The x case can be easily obtained later by setting $\Gamma \to 0$). At this point, note that x, y will refer to spatial integration variables instead of the usual transverse dimensions. The Gaussian X-ray seed is given by

$$B_E(y, \phi + p) = \frac{1}{2\pi\sigma_r\sigma_\phi} \exp\left[-\frac{y^2}{2\sigma_r^2} - \frac{(\phi+p)^2}{2\sigma_\phi^2}\right]. \tag{A.2}$$

Here, σ_r, σ_ϕ refers to the RMS X-ray beam size and divergence in y respectively. The electron distribution is given by

$$F(\eta, x+y, p) = \frac{1}{(2\pi)^{3/2}\sigma_y\sigma_\eta\sigma_p} \exp\left[-\frac{(x+y-D\eta)^2}{2\sigma_y^2} - \frac{\eta^2}{2\sigma_\eta^2} - \frac{p^2}{2\sigma_p^2}\right]. \tag{A.3}$$

Here, σ_y, σ_p refers to the RMS electron beam size and divergence in y respectively, and σ_η refers to the normalized energy spread where $\eta \equiv (\gamma - \gamma_0)/\gamma_0$. As discussed in the main text, the spontaneous undulator brightness can be obtained from the Wigner transform of

Eq. (3.15):

$$\begin{aligned} B_U(\eta,x,\phi,p,y) &= \int_{-L/2}^{L/2} dzds\, \exp\Big[ik_u\Delta\nu(z-s) - 2ik_u\eta(z-s) \\ &\qquad + ik_uT_\alpha\Big\{(x+y)(z-s) + \frac{p}{2}(z^2-s^2)\Big\}\Big] \\ &\quad \times \int d\xi\, \exp\Big[-ikx\xi + \frac{ik}{2}\Big((\phi+\xi/2)^2z - (\phi-\xi/2)^2s\Big)\Big], \end{aligned} \tag{A.4}$$

where $\Delta\nu \equiv (\omega-\omega_1)/\omega_1$ is the frequency detuning from the fundamental harmonic. We evaluate the Wigner integral to get

$$\begin{aligned} B_U(\eta,x,\phi,p,y) &= \int_{-L/2}^{L/2} dzds \sqrt{\frac{8\pi i}{k(z-s)}} \exp\Big[ik_u\Delta\nu(z-s) - 2ik_u\eta(z-s) \\ &\quad + ik_uT_\alpha\Big\{(x+y)(z-s) + \frac{p}{2}(z^2-s^2)\Big\} \\ &\quad - \frac{2ik}{z-s}x^2 - \frac{2iksz}{z-s}\phi^2 + \frac{2ik(z+s)}{z-s}x\phi\Big]. \end{aligned} \tag{A.5}$$

Note that

$$\frac{\partial B_U}{\partial \eta} = -2ik_u(z-s)B_U. \tag{A.6}$$

We then substitute Eqs. (A.2) through (A.6) into the gain convolution formula, and perform Gaussian integration in each variable. Generically, the Gaussian integral takes the form

$$\int dx \exp\Big(-Ax^2 + Bx\Big) = \sqrt{\frac{\pi}{A}} \exp\left(\frac{B^2}{4A}\right). \tag{A.7}$$

In each case, we will use coefficients A, B with the appropriate subscripts (e.g. A_x, B_x for the dx integral) to denote the result. For brevity, we will define the following parameters:

$$\begin{aligned}
\Sigma_y^2 &= \sigma_y^2 + \sigma_r^2 + D^2\sigma_\eta^2, && \text{(A.8)}\\
\Sigma_{yr}^2 &= \sigma_y^2 + \sigma_r^2, && \text{(A.9)}\\
\Sigma_{y\eta}^2 &= \sigma_y^2 + D^2\sigma_\eta^2, && \text{(A.10)}\\
\Sigma_\phi^2 &= \sigma_p^2 + \sigma_\phi^2. && \text{(A.11)}
\end{aligned}$$

We will also use short-hand notation for the following recurring terms:

$$\begin{aligned}
\left[\ldots\sigma_\phi^2\right] &= (z-s) + 4ikssz\sigma_\phi^2, && \text{(A.12)}\\
\left[\ldots\Sigma_\phi^2\right] &= (z-s) + 4iksz\Sigma_\phi^2, && \text{(A.13)}\\
[BD] &= (z-s)[1 + 4k^2\Sigma_{yr}^2\Sigma_\phi^2] + 4ik[\Sigma_{yr}^2 + sz\Sigma_\phi^2], && \text{(A.14)}\\
[BD]_y &= (z-s)[1 + 4k^2\Sigma_y^2\Sigma_\phi^2] + 4ik[\Sigma_y^2 + sz\Sigma_\phi^2], && \text{(A.15)}\\
[BD]_{\sigma_r} &= (z-s)[1 + 4k^2\sigma_r^2\Sigma_\phi^2] + 4ik[\sigma_r^2 + sz\Sigma_\phi^2], && \text{(A.16)}\\
[BD]_{\sigma_\phi} &= (z-s)[1 + 4k^2\Sigma_y^2\sigma_\phi^2] + 4ik[\Sigma_y^2 + sz\sigma_\phi^2]. && \text{(A.17)}
\end{aligned}$$

We will perform a total of five Gaussian integrals, followed by consolidating and simplifying the prefactor and the terms in the exponential. The steps are listed in order below.

The $d\phi$ integral

The integral takes the form

$$\int d\phi \exp\left[-\phi^2\left(\frac{1}{2\sigma_\phi^2} + \frac{2iksz}{z-s}\right) + \phi\left(-\frac{p}{\sigma_\phi^2} + \frac{2ik(z+s)x}{z-s}\right)\right], \qquad \text{(A.18)}$$

whence we can consolidate the terms

$$\begin{aligned}
A_\phi &= \frac{1}{2\sigma_\phi^2} + \frac{2iksz}{z-s} = \frac{[\dots\sigma_\phi^2]}{2(z-s)\sigma_\phi^2}, && \text{(A.19)}\\
B_\phi &= \frac{2ik(z+s)x\sigma_\phi^2 - p(z-s)}{\sigma_\phi^2(z-s)}, && \text{(A.20)}\\
\frac{B_\phi^2}{4A_\phi} &= p^2\,\frac{z-s}{2\sigma_\phi^2[\dots\sigma_\phi^2]} - px\,\frac{2ik(z+s)}{[\dots\sigma_\phi^2]} - x^2\,\frac{2k^2(z+s)^2\sigma_\phi^2}{(z-s)[\dots\sigma_\phi^2]}. && \text{(A.21)}
\end{aligned}$$

From the form of Eq. (A.7), we note that A_ϕ will feature in the prefactor of the final result, whereas the $B_\phi^2/4A_\phi$ term will carry into subsequent integrations. This is repeated for the subsequent integration steps.

The dy integral

We have

$$\int dy \exp\left[-y^2\left(\frac{1}{2\sigma_r^2}+\frac{1}{2\sigma_y^2}\right) + y\left(-\frac{x-D\eta}{\sigma_y^2} + ik_uT_\alpha(z-s)\right)\right], \tag{A.22}$$

whence

$$\begin{aligned}
A_y &= \frac{\sigma_y^2+\sigma_r^2}{2\sigma_y^2\sigma_r^2} = \frac{\Sigma_{yr}^2}{2\sigma_y^2\sigma_r^2}, && \text{(A.23)}\\
B_y &= \frac{ik_uT_\alpha(z-s)\sigma_y^2 - x + D\eta}{\sigma_y^2}, && \text{(A.24)}\\
\frac{B_y^2}{4A_y} &= x^2\,\frac{\sigma_r^2}{2\sigma_y^2\Sigma_{yr}^2} - x\eta\,\frac{D\sigma_r^2}{\sigma_y^2\Sigma_{yr}^2} + \eta^2\,\frac{D^2\sigma_r^2}{2\sigma_y^2\Sigma_{yr}^2} - x\,\frac{ik_uT_\alpha(z-s)\sigma_r^2}{\Sigma_{yr}^2}\\
&\quad +\eta\,\frac{iDk_uT_\alpha(z-s)\sigma_r^2}{\Sigma_{yr}^2} - \frac{\left[k_uT_\alpha(z-s)\sigma_r\sigma_y\right]^2}{2\Sigma_{yr}^2}. && \text{(A.25)}
\end{aligned}$$

The dp integral

Including terms from the $d\phi$ integral, we get

$$\int dp \exp\left[-p^2\left(\frac{1}{2\sigma_\phi^2}+\frac{1}{2\sigma_p^2}-\frac{z-s}{2\sigma_\phi^2[\ldots\sigma_\phi^2]}\right)+p\left(\frac{ik_uT_\alpha(z^2-s^2)}{2}-\frac{2ik(z+s)x}{[\ldots\sigma_\phi^2]}\right)\right], \tag{A.26}$$

whence

$$\begin{aligned}
A_p &= \frac{(z-s)+4iksz\Sigma_\phi^2}{2\sigma_p^2[\ldots\sigma_\phi^2]}=\frac{[\ldots\Sigma_\phi^2]}{2\sigma_p^2[\ldots\sigma_\phi^2]}, && \text{(A.27)}\\
B_p &= \frac{ik_uT_\alpha(z^2-s^2)[\ldots\sigma_\phi^2]-4ik(z+s)x}{2[\ldots\sigma_\phi^2]}, && \text{(A.28)}\\
\frac{B_p^2}{4A_p} &= -x^2\,\frac{2k^2(z+s)\sigma_p^2}{[\ldots\Sigma_\phi^2][\ldots\sigma_\phi^2]}+x\,\frac{kk_uT_\alpha(z+s)(z^2-s^2)\sigma_p^2}{[\ldots\Sigma_\phi^2]}\\
&\quad -\frac{[k_uT_\alpha\sigma_p(z^2-s^2)]^2[\ldots\sigma_\phi^2]}{8[\ldots\Sigma_\phi^2]}. && \text{(A.29)}
\end{aligned}$$

The dx integral

The previous three integrations all contribute terms to this integral:

$$\begin{aligned}
\int dx \exp\Bigg[&-x^2\left(\frac{1}{2\sigma_y^2}+\frac{2ik}{z-s}+\frac{2k^2(z+s)^2\sigma_\phi^2}{(z-s)[\ldots\sigma_\phi^2]}-\frac{\sigma_r^2}{2\sigma_y^2\Sigma_{yr}^2}+\frac{2k^2(z+s)^2\sigma_p^2}{[\ldots\Sigma_\phi^2][\ldots\sigma_\phi^2]}\right)\\
&+x\left(\frac{D\eta}{\sigma_y^2}+ik_uT_\alpha(z-s)-\frac{D\eta\sigma_r^2}{\sigma_y^2\Sigma_{yr}^2}-\frac{ik_uT_\alpha(z-s)\sigma_r^2}{\Sigma_{yr}^2}\right.\\
&\left.+\frac{kk_uT_\alpha(z+s)(z^2-s^2)\sigma_p^2}{[\ldots\Sigma_\phi^2]}\right)\Bigg], \qquad \text{(A.30)}
\end{aligned}$$

whence

$$\begin{aligned}
A_x &= \frac{(z-s)[1+4k^2\Sigma_{yr}^2\Sigma_\phi^2]+4ik[\Sigma_{yr}^2+sz\Sigma_\phi^2]}{2\Sigma_{yr}^2[\ldots\Sigma_\phi^2]} = \frac{[BD]}{2\Sigma_{yr}^2[\ldots\Sigma_\phi^2]}, && \text{(A.31)}\\
B_x &= \frac{(ik_uT_\alpha(z-s)\sigma_y^2+D\eta)[\ldots\Sigma_\phi^2]+kk_uT_\alpha(z+s)(z^2-s^2)\sigma_p^2\Sigma_{yr}^2}{\Sigma_{yr}^2[\ldots\Sigma_\phi^2]}, && \text{(A.32)}\\
\frac{B_x^2}{4A_x} &= \eta^2\,\frac{D^2[\ldots\Sigma_\phi^2]}{2\Sigma_{yr}^2[BD]} + \eta\,\frac{iDk_uT_\alpha(z-s)\sigma_y^2[\ldots\Sigma_\phi^2]+Dkk_uT_\alpha(z-s)(z+s)^2\sigma_p^2\Sigma_{yr}^2}{\Sigma_{yr}^2[BD]}\\
&\quad +k_u^2T_\alpha^2(z-s)^2\,\frac{k^2(z+s)^4\sigma_p^4\Sigma_{yr}^4+2ik[\ldots\Sigma_\phi^2](z+s)^2\sigma_p^2\sigma_y^2\Sigma_{yr}^2-[\ldots\Sigma_\phi^2]\sigma_y^4}{2\Sigma_{yr}^2[BD][\ldots\Sigma_\phi^2]}. && \text{(A.33)}
\end{aligned}$$

The $d\eta$ integral

We have

$$\begin{aligned}
&\int d\eta\exp\Bigg[-\eta^2\left(\frac{D^2}{2\sigma_y^2}+\frac{1}{2\sigma_\eta^2}-\frac{D^2\sigma_r^2}{2\sigma_y^2\Sigma_{yr}^2}-\frac{D^2[\ldots\Sigma_\phi^2]}{2\Sigma_{yr}^2[BD]}\right)+\eta\Bigg(-2ik_u(z-s)\\
&\qquad +\frac{iDk_uT_\alpha(z-s)\sigma_r^2}{\Sigma_{yr}^2}+iDk_uT_\alpha(z-s)\,\frac{\sigma_y^2[\ldots\Sigma_\phi^2]-ik(z+s)^2\sigma_p^2\Sigma_{yr}^2}{\Sigma_{yr}^2[BD]}\Bigg)\Bigg], && \text{(A.34)}
\end{aligned}$$

whence

$$\begin{aligned}
A_\eta &= \frac{[BD]_y}{2\sigma_\eta^2[BD]}, && \text{(A.35)}\\
B_\eta &= -\frac{2ik_u(z-s)[BD]-iDk_uT_\alpha(z-s)\big\{[BD]_{\sigma_r}-ik(z+s)^2\sigma_p^2\big\}}{[BD]}, && \text{(A.36)}\\
\frac{B_\eta^2}{4A_\eta} &= -\frac{2[BD]k_u^2(z-s)^2\sigma_\eta^2}{[BD]_y}+\frac{2Dk_u^2T_\alpha(z-s)^2\sigma_\eta^2\big\{[BD]_{\sigma_r}-ik(z+s)^2\sigma_p^2\big\}}{[BD]_y}\\
&\qquad -\frac{(k_uT_\alpha(z-s)D\sigma_\eta)^2\big\{[BD]_{\sigma_r}-ik(z+s)^2\sigma_p^2\big\}}{2[BD]_y[BD]}. && \text{(A.37)}
\end{aligned}$$

Consolidating the prefactor

The prefactor coming out of all the Gaussian integrals is

$$\frac{\pi^{5/2}}{\sqrt{A_pA_\phi A_yA_xA_\eta}} = \frac{(2\pi)^{5/2}\sigma_\phi\sigma_p\sigma_y\sigma_r\sigma_\eta(z-s)}{[BD]_y}. \tag{A.38}$$

Combining this with the gain convolution integral prefactor gives the final prefactor, after also accounting for the non-TGU x dimension.

Simplifying the exponential

Consolidating all the surviving terms in the exponential results in the following exponent:

$$\begin{aligned}
&\underbrace{ik_u\Delta\nu(z-s)}_{a} - k_u^2T_\alpha^2(z-s)^2\left\{\underbrace{\frac{\sigma_{r_1}^2\sigma_{x_1}^2}{2\Sigma_{yr}^2}}_{b} + \underbrace{\frac{\sigma_{p_1}^2(z+s)^2[\dots\sigma_{\phi_1}^2]}{8[\dots\Sigma_{\phi_1}]}}_{c}\right.\\
&\quad\left. - \underbrace{\frac{\left[k(z+s)^2\sigma_{p_1}^2\Sigma_{yr}^2 + i\sigma_{x_1}^2[\dots\Sigma_{\phi_1}^2]\right]^2}{2\Sigma_{yr}^2[BD][\dots\Sigma_{\phi_1}^2]}}_{d} + \underbrace{\frac{D^2\sigma_\eta^2\left[[BD]_{\sigma_{r_1}} - ik(z+s)^2\sigma_{p_1}^2\right]^2}{2[BD]_y[BD]}}_{e}\right\}\\
&\quad - \underbrace{\frac{2[BD]k_u^2(z-s)^2\sigma_\eta^2}{[BD]_y}}_{f} + \underbrace{\frac{2Dk_u^2T_\alpha(z-s)^2\sigma_\eta^2\left[[BD]_{\sigma_{r_1}} - ik(z+s)^2\sigma_{p_1}^2\right]}{[BD]_y}}_{g},
\end{aligned} \tag{A.39}$$

where we labelled each term with lowercase letters for easy reference. Expand term d to get

$$d = -\underbrace{\frac{k^2(z+s)^4\sigma_p^4\Sigma_{yr}^2}{2[BD][\dots\Sigma_\phi^2]}}_{h} - \underbrace{\frac{ik(z+s)^2\sigma_p^2\sigma_y^2}{[BD]}}_{i} + \underbrace{\frac{[\dots\Sigma_\phi^2]\sigma_y^4}{2\Sigma_{yr}^2[BD]}}_{j}. \tag{A.40}$$

Expand term e to get

$$e = \underbrace{\frac{D^2\sigma_\eta^2[BD]_{\sigma_r}^2}{2[BD]_y[BD]}}_{k} - \underbrace{\frac{ikD^2\sigma_\eta^2(z+s)^2\sigma_p^2[BD]_{\sigma_r}}{[BD]_y[BD]}}_{l} - \underbrace{\frac{k^2D^2\sigma_\eta^2(z+s)^4\sigma_p^4}{2[BD]_y[BD]}}_{m}. \tag{A.41}$$

Combine the terms c, h and m to get

$$c + h + m = \frac{\sigma_p^2(z+s)^2[BD]_{\sigma_\phi}}{8[BD]_y}. \tag{A.42}$$

Next, combine the following terms:

$$i + l = -\frac{ik(z+s)^2\sigma_p^2\Sigma_{y\eta}^2}{[BD]_y}, \qquad b + j + k = \frac{[BD]_{\sigma_r}\Sigma_{y\eta}^2}{2[BD]_y}. \tag{A.43}$$

Consolidate all the terms so far to obtain

$$\begin{aligned}&-ik_u\Delta\nu(z-s) - k_u^2T_\alpha^2(z-s)^2\left\{\underbrace{\frac{\Sigma_{y\eta}^2[BD]_{\sigma_r}}{2[BD]_y}}_{p} + \underbrace{\frac{\sigma_p^2(z+s)^2[BD]_{\sigma_\phi}}{8[BD]_y}}_{q} - \underbrace{\frac{ik(z+s)^2\sigma_p^2\Sigma_{y\eta}^2}{[BD]_y}}_{r}\right\}\\ &-\underbrace{\frac{2[BD]k_u^2(z-s)^2\sigma_\eta^2}{[BD]_y}}_{s} + \underbrace{\frac{2Dk_u^2T_\alpha(z-s)^2[BD]_{\sigma_r}\sigma_\eta^2}{[BD]_y}}_{t} - \underbrace{\frac{2iDkk_u^2T_\alpha(z^2-s^2)^2\sigma_\eta^2\sigma_p^2}{[BD]_y}}_{u}.\end{aligned} \tag{A.44}$$

Combine terms q, r, and u together, and terms p, s, and t together. This results in

$$\begin{aligned}&-ik_u\Delta\nu(z-s) - \frac{k_u^2(z-s)^2}{2}\left\{\frac{4\sigma_\eta^2[BD] - [BD]_{\sigma_r}(T_\alpha^2\Sigma_{y\eta}^2 - 4T_\alpha D\sigma_\eta^2)}{[BD]_y}\right\}\\ &-\frac{k_u^2\sigma_p^2(z^2-s^2)^2T_\alpha}{8}\left\{\frac{T_\alpha[BD]_{\sigma_\phi} + 8ik(T_\alpha\Sigma_{y\eta}^2 - 2D\sigma_\eta^2)}{[BD]_y}\right\}\end{aligned} \tag{A.45}$$

Now impose the dispersion-gradient relationship:

$$\alpha D = \frac{2+K_0^2}{K_0^2}\frac{D^2\sigma_\eta^2}{\Sigma_{y\eta}^2}, \quad \Rightarrow \quad T_\alpha = \frac{2D\sigma_\eta^2}{\Sigma_{y\eta}^2}. \tag{A.46}$$

Plugging that in, we obtain

$$-ik_u\Delta\nu(z-s) - \frac{2k_u^2(z-s)^2\sigma_y^2\sigma_\eta^2}{\Sigma_{y\eta}^2} - \frac{k_u^2\sigma_p^2(z^2-s^2)^2D^2\sigma_\eta^4}{2\Sigma_{y\eta}^4}\frac{[BD]_{\sigma_\phi}}{[BD]_y}. \tag{A.47}$$

At this point, we substitute in the definitions Eq. (3.20) through Eq. (3.27) to arrive at the the 3D gain formula Eq. (3.19).

REFERENCES

[1] J. M. J. Madey, "Stimulated emission of bremsstrahlung in a periodic magnetic field," *Journal of Applied Physics*, vol. 42, p. 1906, 1971.

[2] D. A. G. Deacon, L. R. Elias, J. M. J. Madey, G. J. Ramian, H. A. Schwettman, and T. I. Smith, "First operation of a free-electron laser," *Physical Review Letters*, vol. 38, p. 892, 1977.

[3] K.-J. Kim, Z. Huang, and R. Lindberg, *Synchrotron radiation and free-electron lasers: Principles of coherent X-ray generation.* Cambridge, United Kingdom: Cambridge University Press, 2017.

[4] G. R. Neil, "FEL oscillators," *Proceedings of the 2003 Particle Accelerator Conference*, p. 181, 2003.

[5] J. Feldhaus, "FLASH—the first soft x-ray free electron laser (FEL) user facility," *Journal of Physics B*, vol. 43, p. 194002, 2010.

[6] C. Bostedt, S. Boutet, D. M. Fritz, Z. Huang, H. J. Lee, H. T. Lemke, A. Robert, W. F. Schlotter, J. J. Turner, and G. J. Williams, "Linac Coherent Light Source: The first five years," *Reviews of Modern Physics*, vol. 88, p. 015007, Mar. 2016.

[7] H. Weise and W. Decking, "Commissioning and First Lasing of the European XFEL," *Proceedings of FEL2017*, p. 9, 2017.

[8] N. S. Huang, H. X. Deng, B. Liu, and D. Wang, "Physical design and FEL performance study for FEL-III beamline of SHINE," *Proceedings of FEL2019*, p. 199, 2019.

[9] C. J. Milne, T. Schietinger, M. Aiba *et al.*, "SwissFEL: The Swiss X-ray free electron laser," *Applied Sciences*, vol. 7, p. 720, 2017.

[10] Y. Shvyd'ko, S. Stoupin, V. Blank, and S. Terentyev, "Near-100% Bragg reflectivity of X-rays," *Nature Photonics*, vol. 5, p. 539, 2011.

[11] K.-J. Kim and Y. V. Shvyd'ko, "Tunable optical cavity for an X-ray free-electron-laser oscillator," *Physical Review Special Topics Accelerators and Beams*, vol. 12, p. 030703, Mar. 2009.

[12] K.-J. Kim, Y. Shvyd'ko, and S. Reiche, "A Proposal for an X-Ray Free-Electron Laser Oscillator with an Energy-Recovery Linac," *Physical Review Letters*, vol. 100, p. 244802, Jun. 2008.

[13] A. Snigirev, V. Kohn, I. Snigireva, and B. Lengeler, "A compound refractive lens for focusing high-energy X-rays," *Nature*, vol. 384, pp. 49–51, Nov. 1996.

[14] B. Adams and K. J. Kim, "X-ray comb generation from nuclear-resonance-stabilized X-ray free-electron laser oscillator for fundamental physics and precision metrology," *Physical Review Special Topics Accelerators and Beams*, vol. 18, p. 030711, 2015.

[15] T. I. Smith, J. M. J. Madey, L. R. Elias, and D. A. G. Deacon, “Reducing the sensitivity of a free-electron laser to electron energy,” *Journal of Applied Physics*, vol. 50, pp. 4580–4583, 1979.

[16] R. R. Lindberg, K.-J. Kim, Y. Cai, Y. Ding, and Z. Huang, “Transverse Gradient Undulators for a Storage Ring X-ray FEL Oscillator,” *Proceedings of FEL2013*, pp. 740–748, 2013.

[17] M. Billardon, “Storage ring free-electron laser and chaos,” *Physical Review Letters*, vol. 65, pp. 713–716, Aug. 1990.

[18] V. Litvinenko, S. Park, I. Pinayev, and Y. Wu, “Time structure of the OK-4/Duke storage ring FEL,” *Nuclear Instruments and Methods in Physics Research Section A: Accelerators, Spectrometers, Detectors and Associated Equipment*, vol. 475, pp. 240–246, Dec. 2001.

[19] P. Elleaume, “Storage ring FEL theory,” *Nuclear Instruments and Methods in Physics Research Section A: Accelerators, Spectrometers, Detectors and Associated Equipment*, vol. 237, pp. 28–37, Jun. 1985.

[20] ——, “Macro-temporal structure of storage ring free electron lasers,” *Journal de Physique*, vol. 45, pp. 997–1001, 1984.

[21] G. Marcus and F.-J. Decker, “Cavity-based free-electron laser research and development: A joint Argonne National Laboratory and SLAC National Laboratory collaboration,” *Proceedings of FEL2019*, p. 282, 2019.

[22] C. Schroer, I. Agapov, R. Roehlsberger, R. Wanzenberg, R. Brinkmann, E. Weckert, and W. Leemans, *PETRA IV Conceptual Design Report.* Deutsches Elektronen-Synchrotron, DESY, Hamburg, 2019.

[23] K.-J. Kim, “Brightness, coherence and propagation characteristics of synchrotron radiation,” *Nuclear Instruments and Methods in Physics Research Section A: Accelerators, Spectrometers, Detectors and Associated Equipment*, vol. 246, pp. 71–76, May 1986.

[24] P. Schmüser, M. Dohlus, J. Rossbach, and C. Behrens, *Free-Electron Lasers in the Ultraviolet and X-Ray Regime: Physical Principles, Experimental Results, Technical Realization.* Springer International Publishing, 2014, vol. 258.

[25] Z. Huang and K.-J. Kim, “Review of X-ray free-electron laser theory,” *Physical Review Special Topics Accelerators and Beams*, vol. 10, p. 034801, Mar 2007.

[26] K.-J. Kim, “FEL gain taking into account diffraction and electron beam emittance; generalized Madey’s theorem,” *Nuclear Instruments and Methods in Physics Research Section A: Accelerators, Spectrometers, Detectors and Associated Equipment*, vol. 318, pp. 489–494, Jul. 1992.

[27] M. Billardon, P. Elleaume, J. Ortega, C. Bazin, M. Bergher, Y. Petroff, and M. Velghe, “Results of the Orsay storage ring free electron laser oscillation,” *Nuclear Instruments and Methods in Physics Research Section A: Accelerators, Spectrometers, Detectors and Associated Equipment*, vol. 237, pp. 244–253, Jun. 1985.

[28] D. A. Edwards and M. J. Syphers, *An Introduction to the Physics of High Energy Accelerators*, 1st ed. Wiley-VCH, 2008.

[29] S. Y. Lee, *Accelerator Physics*, 2nd ed. World Scientific, Dec. 2004.

[30] M. Sands, “The physics of electron storage rings: An introduction,” Stanford Linear Accelerator Center, Tech. Rep. 121, Nov. 1970.

[31] N. Martensson and M. Eriksson, “The saga of MAX IV, the first multi-bend achromat synchrotron light source,” *Nuclear Instruments and Methods in Physics Research Section A: Accelerators, Spectrometers, Detectors and Associated Equipment*, vol. 907, p. 97, 2018.

[32] K. W. Robinson, “Radiation effects in circular electron accelerators,” *Physical Review*, vol. 111, p. 373, 1958.

[33] P. Baxevanis, Y. Ding, Z. Huang, and R. Ruth, “3D theory of a high-gain free-electron laser based on a transverse gradient undulator,” *Physical Review Special Topics Accelerators and Beams*, vol. 17, p. 020701, Feb. 2014.

[34] Z. Huang, Y. Ding, and C. B. Schroeder, “Compact X-ray Free-Electron Laser from a Laser-Plasma Accelerator Using a Transverse-Gradient Undulator,” *Physical Review Letters*, vol. 109, p. 204801, Nov. 2012.

[35] N. Kroll, P. Morton, M. Rosenbluth, J. Eckstein, and J. Madey, “Theory of the transverse gradient wiggler,” *IEEE Journal of Quantum Electronics*, vol. 17, pp. 1496–1507, Aug. 1981.

[36] D. Cocco, G. Cutler, M. Sanchez del Rio, L. Rebuffi, X. Shi, and K. Yamauchi, “Wavefront preserving X-ray optics for synchrotron and free electron laser photon beam transport systems,” *Physics Reports*, vol. 974, p. 1, 2022.

[37] S. Reiche, *GENESIS 1.3 Manual*, 2004.

[38] W. M. Fawley, *A User Manual for GINGER-H and its Post-Processor XPLOTGINH*, 2012.

[39] Y. S. Li, R. R. Lindberg, and K.-J. Kim, “Axial symmetry in spontaneous undulator radiation for XFELO two-bunch experiment,” *Proceedings of FEL2019*, p. 134, 2019.

[40] M. Borland, *User’s Manual for elegant*, 2021.

[41] R. R. Lindberg, K.-J. Kim, Y. Shvyd'ko, and W. M. Fawley, "Performance of the X-ray free-electron laser oscillator with crystal cavity," *Physical Review Special Topics Accelerators and Beams*, vol. 14, p. 010701, Jan. 2011.

[42] T. Naito, S. Araki, H. Hayano, K. Kubo, S. Kuroda, N. Terunuma, T. Okugi, and J. Urakawa, "Multibunch beam extraction using the strip-line kicker at the KEK Accelerator Test Facility," *Physical Review Special Topics Accelerators and Beams*, vol. 14, p. 051002, May 2011.

[43] J. Calvey and M. Borland, "Modeling ion effects for the Argonne Advanced Photon Source upgrade," *Physical Review Accelerators and Beams*, vol. 22, p. 114403, Nov. 2019.

[44] I. Lyatun, P. Ershov, I. Snigireva, and A. Snigirev, "Impact of beryllium microstructure on the imaging and optical properties of X-ray refractive lenses," *Journal of Synchrotron Radiation*, vol. 27, p. 44, 2020.